

# Dynamic Wind and Wake Effects in Wind Farms: Simulations and Modeling

*Yang Liu*

# DYNAMIC WIND AND WAKE EFFECTS IN WIND FARMS: SIMULATIONS AND MODELING

## DISSERTATION

to obtain  
the degree of doctor at the University of Twente,  
on the authority of the rector magnificus,  
prof. dr. A. Veldkamp,  
on account of the decision of the Doctorate Board,  
to be publicly defended  
on Wednesday 10th of December 2025 at 16:45

by

Yang Liu  
born on the 22nd August, 1995  
in Shandong, China

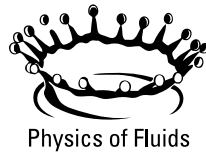
This dissertation has been approved by the promotor:

adj. prof. dr. Richard J.A.M. Stevens

and

prof. dr. Detlef Lohse

**UNIVERSITY  
OF TWENTE.**



The work in this Thesis was carried out at the Physics of Fluids group of the Faculty of Science and Technology of the University of Twente.

Publisher: Yang Liu

ISBN (print): 000

ISBN (digital): 000

© 2025 Yang Liu, The Netherlands. All rights reserved. No parts of this thesis may be reproduced, stored in a retrieval system or transmitted in any form or by any means without permission of the author. Alle rechten voorbehouden. Niets uit deze uitgave mag worden vermenigvuldigd, in enige vorm of op enige wijze, zonder voorafgaande schriftelijke toestemming van de auteur.

**Graduation Committee:**

Chair / secretary: prof. dr. Jeroen J.L.M. Cornelissen  
University of Twente

Promotors: adj. prof. dr. Richard J.A.M. Stevens  
University of Twente

prof. dr. Detlef Lohse  
University of Twente

Committee Members:: prof. dr. Devaraj van der Meer  
University of Twente

prof. dr. Cornelis H. Venner  
University of Twente

prof. dr. Fulvio Scarano  
Delft University of Technology

assoc. prof. dr. Joshua R. Brinkerhoff  
The University of British Columbia

# Contents

<b>Introduction</b>	<b>1</b>
<b>1 Modeling low-frequency wind speed variations in large-eddy simulations of wind farms</b>	<b>9</b>
1.1 Introduction . . . . .	11
1.2 LES framework . . . . .	12
1.3 Modeling dynamically changing wind speed in LES . . . . .	13
1.4 Idealized test cases . . . . .	15
1.5 Low-frequency dynamic wind speed variations . . . . .	16
1.6 Effect of dynamic wind speed variations on wind farm performance	19
1.7 Conclusions . . . . .	23
<b>2 Atmospheric boundary layer response to the dynamic geostrophic wind forcing</b>	<b>25</b>
2.1 Introduction . . . . .	27
2.2 Modeling geostrophic wind speed variations . . . . .	29
2.3 Turbulence parameterization . . . . .	31
2.4 Modeling dynamic wind speed changes . . . . .	33
2.5 Conclusions . . . . .	41
<b>Appendices</b>	<b>41</b>
2.A LES framework . . . . .	41
<b>3 Turbulence coherence in wind farms: The role of turbines</b>	<b>43</b>
3.1 Introduction . . . . .	45
3.2 Theoretical framework . . . . .	46
3.3 Large eddy simulations . . . . .	49
3.4 Turbine coherence within an extended wind farm . . . . .	49
3.5 Conclusions . . . . .	58
<b>4 Wake-corrected random sweeping model for wind farm power coherence</b>	<b>61</b>
4.1 Introduction . . . . .	63
4.2 Large eddy simulations of wind farms . . . . .	65
4.3 Wake-induced coherence loss between turbines . . . . .	67

4.4 Accounting for turbine wakes in random sweeping theory . . . . .	69
4.5 Effect of entrance-region flow dynamics on coherence . . . . .	73
4.6 Conclusions . . . . .	76
<b>5 Modeling multi-scale atmospheric interactions in wind farm power spectra</b>	<b>79</b>
5.1 Introduction . . . . .	81
5.2 Theory . . . . .	82
5.3 Coherence between turbine pairs . . . . .	87
5.4 Wind farm spectra . . . . .	88
5.5 Conclusions . . . . .	91
<b>Appendices</b>	<b>92</b>
5.A Large-eddy simulations of wind farms . . . . .	92
5.B Modeling atmospheric spectra . . . . .	93
5.C Modeling wind farm data in Figure 5.1.1 . . . . .	95
<b>Conclusions and Outlook</b>	<b>97</b>
<b>References</b>	<b>99</b>
<b>Summary</b>	<b>107</b>
<b>Samenvatting</b>	<b>109</b>
<b>Acknowledgements</b>	<b>113</b>
<b>About the author</b>	<b>117</b>

# Introduction

Wind farms harvest energy from the wind, a resource with inherent variability. As a result, wind power displays turbulent fluctuations across a wide range of timescales, from seconds to minutes at high frequencies to hours and days at low frequencies [1–4]. Modern wind farms, often consisting of hundreds of turbines spread over tens of kilometers, are strongly affected by turbine wakes, interactions with the atmospheric boundary layer, and even neighboring farms. As with other renewable resources, characterizing and predicting power variability remains a central challenge for the wind energy community [5].

The wide range of scales in wind power generation shapes all aspects of wind energy research. High-frequency vibrations cause dynamic aerodynamical loads on wind turbine blades, which are the main cause of turbine structural and electrical fatigues [6]. Wind variabilities over larger time scales, from seconds to minutes, affect not only the power fluctuations of individual turbines but also the interactions among turbines within a wind farm [7–9]. Understanding the combined power fluctuations of wind farms is essential for integrating them into the power grid. Over longer periods, from hours to days, wind resource availability impacts daily human activities. Periods of calm wind leads to a shortfall in production, called *Dunkelflaute* events [10], pose significant challenges to energy security and reliability.

## Sources of wind energy variability

Wind turbines are located in the lower part of the atmospheric boundary layer, typically from 100 m to 200 m, where the wind conditions are affected by multiple sources of turbulence, see Figure 1.1.

Close to the ground, the atmospheric flow interacts with the surface roughnesses of terrain, which forms a boundary layer with typical thickness around several hundred meters. The turbulence structures in atmospheric boundary layer dominate the wind turbine power production at high frequencies ( $\sim 10^{-2}$  Hz and higher), which is referred to as *microscale* processes. At small scales, the turbulence is fully three-dimensional, and the wavenumber spectrum is observed to follow the Kolmogorov scaling  $k^{-5/3}$  [11–13]. Towards larger scales, the development of turbulence structures is suppressed by ge-

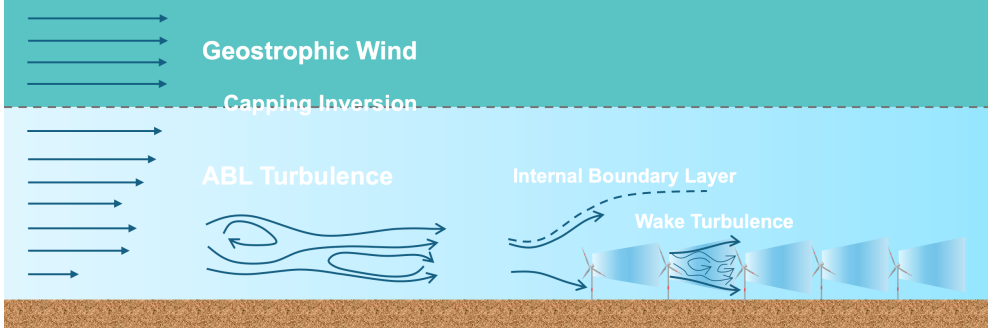


Figure 1: Schematics of turbulence sources that impact wind farm operation: the large-scale variations in geostrophic wind, the atmospheric boundary layer (ABL) turbulence and the wind-farm-induced wake turbulence.

ometry constraints, where the wavenumber spectrum with  $k^{-1}$  scaling is suggested by several studies [13, 14]. The Kolmogorov turbulence can exist till the length scale of height where wind speed is measured, whereas the  $k^{-1}$  region of wall turbulence is controlled by the boundary layer height.

With wind turbines continuously capturing energy from wind, they lower the wind speed and introduce turbulence to the flow, followed by a wake region behind the turbine. Inside wind farms, a cluster of wind turbines creates persistent wake flows, and an internal boundary layer is formed. The downstream turbines operate in the wakes generated by upstream turbines, whose power generation reduces up to 50% and the power fluctuation rises. The flow characteristics in the internal boundary layer depend on wind farm layout, turbine operational state as well as atmospheric conditions, and the cluster wakes can last several kilometers behind the wind farm. The interactions between wind farms and boundary layer turbulence under steady wind conditions have been widely investigated in theoretical, experimental and numerical studies [4, 15, 16].

The atmospheric boundary layer is typically capped by a stably stratified layer, called capping inversion, which limits its interaction with free atmosphere [17, 18]. Above the capping inversion layer, the variability of geostrophic wind is mainly driven by thermal inequilibrium and heterogeneity of Earth's surface, for example the diurnal cycle and land-sea breeze, which are referred to as *mesoscale* processes [19]. These large-scale atmospheric motions span typically more than hundreds of kilometers, shaping the wind power variations

from fifteen minutes to several hours. Most wind farm power data are based on 10-minutes-averaged measurements, evidencing the importance of understanding wind farm power response under *mesoscale* wind condition variations.

## From wind to power: the energy conversion

The energy extraction of a wind turbine strongly depends on the incoming wind speed. The actuator disk theory [20] expresses the power output of a wind turbine as

$$P(t) = 1/2\rho A C_P u_\infty^3(t) \quad (1)$$

where  $\rho$  is the air density,  $A$  is the area of wind rotor disk, and  $C_P$  is the power coefficient specified for each turbine. The turbine power exhibits cubic relation to the inflow wind speed  $u_\infty$ . With wind turbines operate below rated power, the power coefficient remains stable. Considering the simplified case that  $C_P$  is constant, the power fluctuations of wind power is mainly driven by the variation of inflow wind speed. As turbines can be regarded as a temporal probe of turbulence at a fixed position, the space-time correlation of turbulence structures needs to be established to understand the power variations. A common approach is to apply the Taylor's frozen turbulence hypothesis [21], where the turbulence structures are assumed not to evolve when they are advected through wind turbines. The temporal wind speed variation recorded by turbines is therefore related to both spatial structures of turbulence and the speed of the advection. Adopting Taylor's hypothesis, the frequency spectra of wind speed exhibit  $f^{-5/3}$  scaling, respecting the  $k^{-5/3}$  scaling of Kolmogorov turbulence. The spectra of turbine power output, as third power of wind speed variations, also follow the same  $f^{-5/3}$  relation, as suggested by several studies [1–3].

## Power correlations between wind turbines

Modern wind farms consist of hundreds of wind turbines, and the aggregate power fluctuations depend on not only the output of individual turbines, but also power correlations among them. The strength of correlation can also be

quantified by coherence in the spectral domain, which is expressed as a function of frequency. From low-frequency variations to high-frequency fluctuations, wind power shows a decayed trend in coherence. The *mesoscale* processes correlate power variations in a wind farm, and the drop of correlation is observed between geographically distributed wind farms [3]. The decorrelation is related to the integral scale of atmospheric turbulence, which spans typically hundreds of kilometers.

On the other hand, the *microscale* turbulence mainly correlate power of successive turbines, and the correlation strength drops rapidly for a larger distance. Several experimental and numerical studies examined the random sweeping models on predicting wind turbine coherence [7–9], which consider Taylor’s hypothesis for turbulence convection with an unsteady sweeping velocity. The exponential decoherence trend in power fluctuations towards high frequencies is well captured by the model, where both the atmospheric fluctuations and turbine operation impact the turbulence coherence. At the interface of *mesoscale* and *microscale* processes, smoothing effect in wind farm power spectra is evident due to the transition from highly correlated to uncorrelated power fluctuations among wind turbines [22, 23].

## Large-eddy simulations of wind farms

The atmospheric boundary layer is characterized by a very high Reynolds number ( $\sim \mathcal{O}(10^7)$ ) due to its large characteristic length scale and low air viscosity. Therefore, the direct numerical simulations (DNS) of atmospheric flows are extremely challenging for their huge computational demand, as they reproduce the full-scale boundary layer dynamics through resolving eddies from integral to dissipation length scales. The large-eddy simulations (LES) technique proposes a solution that can balance the fidelity and computational cost in numerical simulations. LES use a coarser grid than that in DNS, which only ensures the large eddies to be resolved. Meanwhile, unresolvable turbulent events that are smaller than grid size are parameterized as an additional viscous effect by sub-grid scale models. As sub-grid scale dissipation affects energy transfer between resolved and unresolved scales, the accuracy of LES heavily depends on the modeling of under-resolved turbulence.

LES of atmospheric boundary layer typically solve Navier-Stokes equations of turbulent boundary layer with thermal effects, which are expressed by mass, momentum and heat conservations [24]. As the sub-grid scale dissipation of

kinetic energy is much higher than that of air, the viscosity of air is often neglected. Consequently, the effect of viscous sublayer near the wall needs to be approximated by wall models to provide correct shear stress for fully turbulent region. For this purpose, the Monin-Obukhov similarity theory (MOST) [25, 26] is widely used for various momentum and thermal boundary conditions. Assuming the incompressibility of air in the control equations, the buoyancy effects on momentum transport are modeled by Boussinesq approximation.

The turbines are often represented by an extra force term in wind farm LES. The LES grid size is larger than several meters, which is not capable for resolving geometry of turbine blades. Common approaches for turbine representation in wind farm LES include actuator disk and actuator line models. The actuator disk theory considers the slow down of wind speed over the sweeping area of rotor blades, which is featured by the simple implementation and low additional computational cost. The actuator line models resolve rotor blades as rotating lines with forcings projected to the grid points. While it better represents the turbine effects at near-wake regions, the demand of higher resolutions in simulations makes it not feasible in large domain sizes. For wind farm LES performed in this work, actuator disk model is employed throughout.

## Research challenges and positioning of this thesis

Understanding the wind farm performance across multiple scales is particularly challenging, as either laboratorial or observational approaches can only address one side of the complete picture. Observational approaches, with long-term recorded field data of wind conditions and wind farm power variations, can represent the full-scale dynamics of wind farm flows. However, the numerous effects that impact the atmospheric conditions, for example, wind speed/direction changes and thermal conditions, are continuously varying, making it difficult to expose and study the effect of individual mechanism on wind farm performance. On the other hand, well-controlled conditions can be achieved in emulated environments, like wind tunnel experiments and numerical simulations. Nevertheless, with the limited domain size that only allows *microscale* structures to develop, weather phenomena are not spontaneously captured by LES. Therefore, modeling techniques to represent large-scale effects in LES domain are often needed.

In this thesis, we study the physics of wind farm flow under dynamic con-

ditions using LES. The high-fidelity numerical method resolves the ABL turbulence explicitly, which provides rich information of wind farm flow field. Meanwhile, vortices smaller than the grid-scale are parameterized as subgrid viscous effect, which effectively reduces the computational cost. Therefore, the method enables a detailed investigation of wind farm flows. Whereas most wind farm LES consider scenarios with fixed wind conditions and steady turbine operation states, we focus on dynamic effects in wind farms, where the wind speed changes due to the low-frequency variations in wind conditions. To this end, modeling techniques to represent low-frequency variations in LES are developed, and the response of wind farm flows to dynamic wind conditions is investigated. Results from numerical simulations motivate the physical modeling of wind farms, which improves the understanding of wind farm performance under dynamic wind conditions.

In **Chapter 1**, we provide a modeling technique to represent low-frequency wind speed variations in LES. Using a moving reference frame approach, this method introduces additional forcing term to drive low-frequency wind speed variations, which do not occur in standalone LES. Compared to stationary conditions which most works previously assume, the wind farm exhibits distinct behaviors under dynamic conditions. The varying wind speed conditions lead to dynamic wake effects in wind farms, which significantly affects the power production for downstream turbines. The downstream turbines experience weaker (stronger) velocity deficit under accelerating (decelerating) flow, and produce more (less) power at the same inflow wind speed compared to the steady state.

In **Chapter 2**, we investigate the dynamic response of ABL flow to changes in geostrophic wind speed. Variations in the geostrophic forcing affect both wind speed and direction within the boundary layer through the combined effects of large-scale pressure gradients, the Coriolis force, and turbulence. In addition to LES investigations, we propose a reduced-order model to capture these trends. When boundary layer turbulence is represented appropriately, the model provides satisfactory predictions of the wind speed and direction changes.

In **Chapter 3**, we study turbine power coherence within a wind farm using LES and examine the validity of random sweeping models. Our results show that turbine operation reduces power coherence between turbines, an effect not accounted for in these models. In particular, turbines with active thrust control generate dynamic wakes in response to inflow fluctuations, leading to coherence patterns that random sweeping models fail to capture.

In **Chapter 4**, we conduct a parametric LES study with varying turbine induction factors and inter-turbine spacings. Based on these results, we propose a wake-corrected random sweeping model that incorporates the influence of turbine operation by linking wake-induced decoherence to the turbine induction factor. The analytical, tuning-free model prediction agrees with LES results in different wind farm setups. The model predicts power coherence excellently for most turbines in wind farms, except at the entrance region. In this region, the undisturbed inflow transits into the wind farm internal flow. The formation process of internal boundary layer deflects the wind constantly upwards, which leads to additional turbulence decoherence for wind turbines in the entrance region of wind farms.

In **Chapter 5**, we provide theoretical coherence modeling for wind power variability under multi-scale atmospheric interactions. Random sweeping models only consider microscale scenarios, where wind speed fluctuations are small compared to the mean. The new dynamic sweeping framework includes low-frequency wind speed variations and models the full-scale wind farm power spectrum. Validated by the LES method developed in **Chapter 1**, the model provides a physical explanation of wind farm power smoothing effects. The LES and the model are consistent with trends observed in very high-resolution measurements of wind farm power output fluctuations, revealing different dynamical regimes that can now be captured in both simulations and analytical modeling.

The thesis concludes by summarizing the progress made in modeling multi-scale atmospheric and wake effects on wind farm performance. Finally, the potential applications and future research directions are outlined.



# 1

## Modeling low-frequency wind speed variations in large-eddy simulations of wind farms<sup>◦</sup>

Large-eddy simulations (LES) of wind farms often assume steady inflow, overlooking low-frequency wind speed variations from changing atmospheric conditions. As a result, they capture only higher-frequency boundary-layer turbulence and miss wind speed variations on timescales longer than several minutes. We address this by using a non-inertial moving reference frame within the concurrent precursor framework, allowing the simulation domain to follow the mean wind and produce mass-conserving, time-varying inflow with minimal changes to standard setups. Simulations show that such variability can strongly influence wake flows and wind farm power output, with wake losses decreasing during flow acceleration and increasing during deceleration. These effects stem from wind speed changes on timescales longer than the wake advection time between successive downstream turbines, which traditional LES do not resolve. Including this variability improves the physical fidelity of wind farm performance predictions and supports development of wind farm control strategies under varying inflow conditions.

---

<sup>◦</sup>To be submitted as: Y. Liu, A. Stieren and R.J.A.M. Stevens, *Modeling low-frequency wind speed variations in large eddy simulations of wind farms*.



## 1.1 Introduction

Large-eddy simulations (LES) are frequently employed to investigate the interactions between atmospheric turbulence and wind farms. By capturing three-dimensional flow structures and turbine wakes, LES provide detailed insights into energy generation, wake recovery, and structural loads on wind turbines. However, most wind farm LES assume idealized, statistically steady atmospheric boundary layer (ABL) conditions [4, 5, 27, 28]. As a result, they focus on resolving small-scale atmospheric turbulence with timescales shorter than several minutes, while slower, low-frequency variations are not captured. Consequently, their impact on wind farm performance remains poorly understood. However, the growing scale of wind turbines and farms makes it increasingly important to account for the influence of large-scale, low-frequency atmospheric dynamics on wind farm performance.

In reality, atmospheric conditions constantly change due to shifting weather conditions [19, 29, 30]. This results in relatively slow fluctuations in wind direction and speed, which significantly influence turbine inflow, wake meandering, and structural load [31]. Prior studies have shown that variations in wind direction can influence wind farm performance beyond what is predicted by averaging across different wind directions [32–34]. The role of hysteresis in wind farm performance and control, driven by low-frequency atmospheric variations, remains poorly understood due to the lack of methods to study these effects under controlled conditions [35]. Therefore, it is essential to develop simulation approaches that allow controlled variation of low-frequency atmospheric conditions to advance our understanding of wind farm dynamics and evaluate control strategies.

An approach for incorporating changing atmospheric conditions into LES involves coupling it with weather models, such as the Weather Research and Forecasting (WRF) model [36–38]. Two main strategies have been developed: (i) domain nesting, where LES is embedded within a coarser-scale weather simulation, and (ii) direct forcing of LES using output from the weather model [32, 33, 39, 40]. While nesting captures large-scale variability, the lack of resolved turbulence in weather models requires long fetch regions for the LES to develop realistic turbulent flow within the LES domain [41–43]. Forcing-based approaches are simpler but depend on pressure gradient changes that only slowly affect wind speed, making it challenging to represent the full range of atmospheric turbulence [44].

This study introduces a method to directly incorporate low-frequency wind speed variations, on timescales of several minutes or longer, into wind farm LES. Our approach integrates a non-inertial moving reference frame with the concurrent precursor method [33, 40] to conserve mass and consistently introduce low-frequency wind speed variability into wind farm simulations. The method is validated against steady-state reference cases to confirm accuracy and consistency. We then use a measured wind speed time series  $U(t)$  to assess how dynamic wind speed variations impact wind farm performance. The ability to prescribe user-defined wind speed variations makes this method particularly suited for studying wind farm performance under controlled conditions. The method also supports LES frameworks driven by large-scale weather models or measurement data and can be combined with existing approaches to account for dynamic wind direction changes [33].

The paper begins with a description of the LES setup in Section 3.3. Section 1.3 introduces the new method for incorporating dynamic wind speed variations, which is validated by idealized test cases in Section 1.4. In Section 3.4, we show how measured low-frequency wind speed variations can be used to drive LES. Section 1.6 illustrates how dynamic inflow affects wind farm performance. The paper concludes with discussion and conclusions in Section 5.5.

## 1.2 LES framework

To demonstrate the proposed method, we examine a simplified case of a neutrally stratified pressure-driven ABL. The governing equations for the LES are provided by:

$$\partial_i \tilde{u}_i = 0 \quad , \quad \partial_t \tilde{u}_i + \partial_j (\tilde{u}_i \tilde{u}_j) = -\partial_i \tilde{p}^* - \partial_j \tau_{ij} - \frac{\partial_i p_\infty}{\rho} + f_i. \quad (1.1)$$

The tilde indicates the spatial filtering at the LES grid scale  $\Delta$ , and  $\tilde{u}_i$  represents the filtered variables. The driving pressure gradient is given by  $\partial_i p_\infty / \rho = -u_*^2 / H$ , where  $u_*$  is the friction velocity. The traceless part of the sub-grid scale tensor,  $\tau_{ij} = \widetilde{u_i u_j} - \tilde{u}_i \tilde{u}_j$ , is modeled using the anisotropic minimum dissipation model. The filtered modified pressure is defined as  $\tilde{p}^* = \tilde{p} - p_\infty / \rho - \tau_{kk} / 3$ . The term  $f_i$  represents the turbine forces in the wind farm domain, which are modeled using an actuator disk approach [45].

Due to the high Reynolds numbers associated with atmospheric flows, viscous stresses are considered negligible.

At the top of the domain, a no-penetration condition and zero shear stress are applied, and periodicity is enforced in the horizontal (streamwise and spanwise) directions. At the surface, wall shear stress is modeled using Monin–Obukhov similarity theory, with a surface roughness length of  $z_0 = 0.1$  m, representing flat grassland conditions. All simulation variables are non-dimensionalized using the domain height  $H$  and the reference friction velocity  $u_*|_{t_0}$ , resulting in a characteristic time scale  $t_{\text{ndim}} = H/u_*$ . Horizontal spatial derivatives are computed with a pseudo-spectral method, while second-order central finite differences are used vertically. Time integration is performed using a third-order Adams–Bashforth scheme. Additional numerical details are available in Gadde et al. [46].

### 1.3 Modeling dynamically changing wind speed in LES

Figure 1.1 illustrates the conceptual idea of our approach, which is inspired by the work of Stieren et al. [33] on dynamic wind direction changes. We decompose the wind speed signal as  $U(t) = U_s + U_d(t)$ , where the stationary part  $U_s = U(t_0)$  is the initial value of the signal at time  $t_0$ . The dynamic component  $U_d(t)$  captures the temporal evolution of  $U(t)$  relative to  $U_s$ . Starting from an equilibrium ABL with wind speed  $U_s$ , the dynamic part  $U_d(t)$  is introduced by moving the non-inertial reference frame of the simulation domain in the opposite direction, such that the reference frame velocity is given by  $U_{\text{Frame}}(t) = -U_d(t)$ . In the moving frame of reference, this results in an apparent force that drives the dynamic changes in wind speed.

The resulting momentum equation in Cartesian coordinates reads:

$$\partial_t \tilde{u}_i + \partial_j (\tilde{u}_i \tilde{u}_j) = -\partial_i \tilde{p}^* - \partial_j \tau_{ij} - \frac{\partial_i p_\infty}{\rho} + f_i + \dot{U}(t) \delta_{i1}, \quad (1.2)$$

where the time derivative  $\dot{U}$  represents the inertial force arising from the translation of the reference frame. Since wind speed varies with height, the signal  $U(t)$  is defined as a domain-averaged quantity. For simplicity, we consider only wind speed variations in the streamwise direction, as indicated by the Kronecker delta  $\delta_{i1}$ . This approach builds upon, and can be combined with, the method for modeling dynamic wind direction changes by Stieren et al. [33].

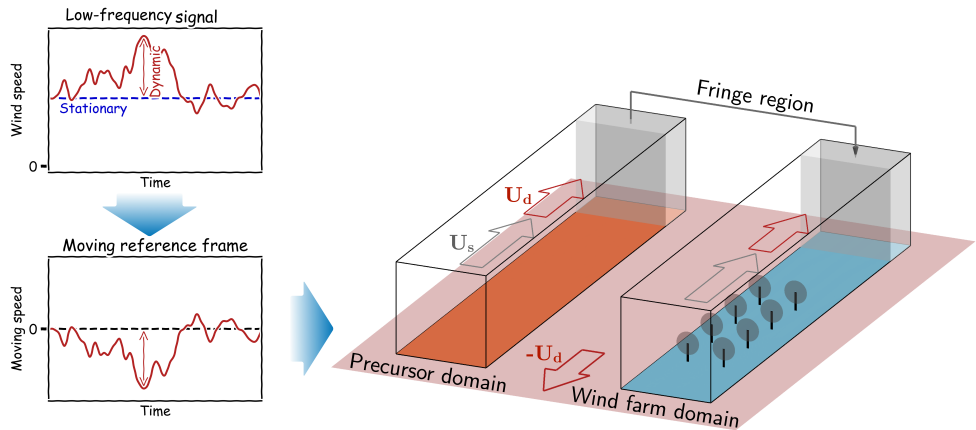


Figure 1.1: Illustrations for modeling low-frequency wind speed variations in wind farm LES. The simulation begins with a stationary wind speed  $U_s$ , and the dynamic signal  $U_d$  is introduced by translating the simulation domain's reference frame in the opposite direction at the same speed.

We assume that the ABL remains in a quasi-equilibrium state during the dynamic process. Consequently, we update the friction velocity and adjust the mean pressure gradient  $\partial_i p_\infty / \rho$  at each time step to match the evolving wind speed.

A key challenge in adjusting the incoming wind speed is maintaining mass conservation, as changes in part of the domain can disrupt the momentum flux across different cross-sections in the domain [44]. We address this by integrating our method within the concurrent precursor framework for simulating wind farms in ABLs [33, 40]. In this setup, two simulations run simultaneously: a precursor simulation alongside the actual wind farm simulation. At each time step, data sampled from the precursor are copied into the fringe region of the wind farm domain, where they serve as the inflow condition. The wind speed signal is applied throughout the entire domain, in both the precursor and wind farm simulations, which ensures that mass conservation is maintained. This enables low-frequency wind speed variations to be smoothly incorporated into the resolved ABL turbulence resolved by LES.

## 1.4 Idealized test cases

We begin by examining simplified monotonic wind speed variations to verify the proposed method. To this end, we perform neutral ABL simulations in a domain of size  $12.56 \text{ km} \times 6.28 \text{ km} \times 1 \text{ km}$  in the streamwise, spanwise, and vertical directions, respectively, using a grid of  $256 \times 128 \times 64$  points. Since the physical viscosity of air is ignored in Eq. 1.2, the simulation is fully non-dimensionalized using the length scale  $H$  and the friction velocity scale  $u_*$ . For illustrative purposes, we choose the non-dimensionalization parameters as  $H_{\text{ndim}} = 1 \text{ km}$  and  $u_{*,\text{ndim}} = 1 \text{ m/s}$ , making each non-dimensional time unit equal to  $t_{\text{ndim}} = H_{\text{ndim}}/u_{*,\text{ndim}} = 1000 \text{ s}$ . A baseline simulation of a stationary ABL with  $u_{*,\text{ref}} = u_{*,\text{ndim}}$  serves as a reference, with its domain-averaged streamwise velocity represented by  $U_{\text{Ref}}$ . For the acceleration scenario, a linear velocity increase from  $U_{\text{Ref}}$  to  $2U_{\text{Ref}}$  is imposed over  $\Delta t_{\text{ndim}} = 0.5, 2$ , and  $8$  time units, corresponding to doubling the wind speed in approximately  $8$  minutes (fast),  $30$  minutes (medium), and  $2$  hours (slow), respectively. Similarly, for the deceleration scenario, the wind speed decreases from  $2U_{\text{Ref}}$  to  $U_{\text{Ref}}$ . The dynamic changes are initiated at  $t_{\text{ndim}} = 50$  when the system is in the statistically stationary state.

Figure 1.2a shows the time evolution of the domain-averaged streamwise velocity. In all cases, the wind speed closely follows the imposed signal, confirming that the dynamic forcing is applied as intended. Figure 1.2b presents the vertical profile of streamwise velocity, averaged over both the acceleration and deceleration phases. The results confirm that the flow remains in quasi-equilibrium throughout the dynamic forcing. The normalized velocity profile, scaled by the reference profile  $u_{\text{ref}}$ , stays by a departure within  $6\%$  of the imposed value. Deviations are most noticeable near the surface, where the flow tends to overshoot, and at higher altitudes, where the velocity is slightly lower than the reference. This pattern is consistent with experimental observations of accelerating boundary layers [47]. The primary effect of flow acceleration is an imbalance between the driving pressure gradient and vertical momentum transport by turbulence. This imbalance arises from the delayed response of turbulent structures to changes in the mean wind speed [48, 49]. As a result, wind speed variations influence turbulent fluctuations with a time lag, and the effect on turbulence intensity is more pronounced during rapid accelerations and decelerations. Figure 1.2c illustrates this behavior, showing that turbulence intensity decreases during acceleration and increases during

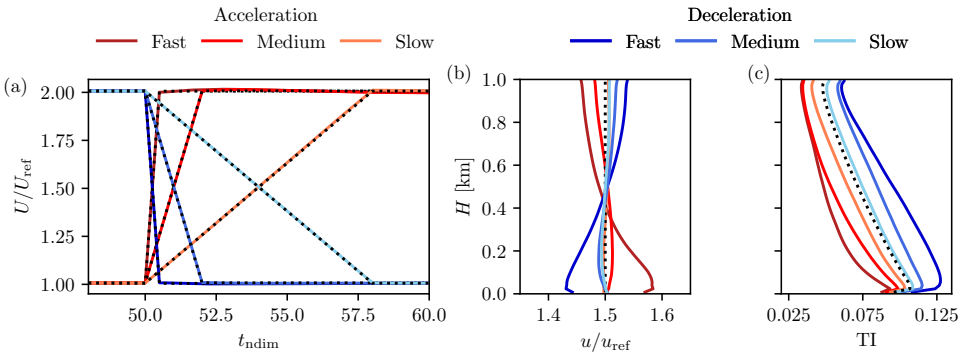


Figure 1.2: (a) Time variation of normalized velocity; (b) vertical profile of streamwise velocity normalized by  $u_{\text{ref}}$ ; (c) vertical profile of turbulent intensity for idealized test cases. The dashed line in panel (a) indicates the imposed wind speed; in panels (b) and (c), it represents the equilibrium ABL profile. Note that  $U/U_{\text{ref}}$  in (a) denotes domain-averaged velocities. In contrast,  $u/u_{\text{ref}}$  and the turbulent intensity in (b) and (c) are height-dependent and averaged over time and the horizontal plane during the acceleration period.

deceleration.

## 1.5 Low-frequency dynamic wind speed variations

To demonstrate our method's ability to replicate realistic wind speed variations, we use a model signal derived from a field-measured wind speed time series in our LES. The data were recorded on January 28, 2018, between 4:30 a.m. and 10:30 a.m. at a height of  $z = 87$  m on the M5 meteorological mast at the NREL National Wind Technology Center [50]. This dataset was chosen based on two criteria: (i) the ABL remained approximately neutral throughout the period, with  $|z/L| \leq 0.05$ , and (ii) there were no significant changes in wind direction. To isolate the low-frequency components, we apply a low-pass filter with a cutoff frequency of  $f_c = 1.8 \times 10^{-3}$  Hz to the original signal. To smoothly integrate it into the LES, we used a second-order Butterworth filter with a transition band extending up to  $2f_c$ , corresponding to timescales of approximately 5 minutes. The resulting signal, called “Model imposed” is shown in Figure 1.3. To prevent transient effects, we treat the first two hours

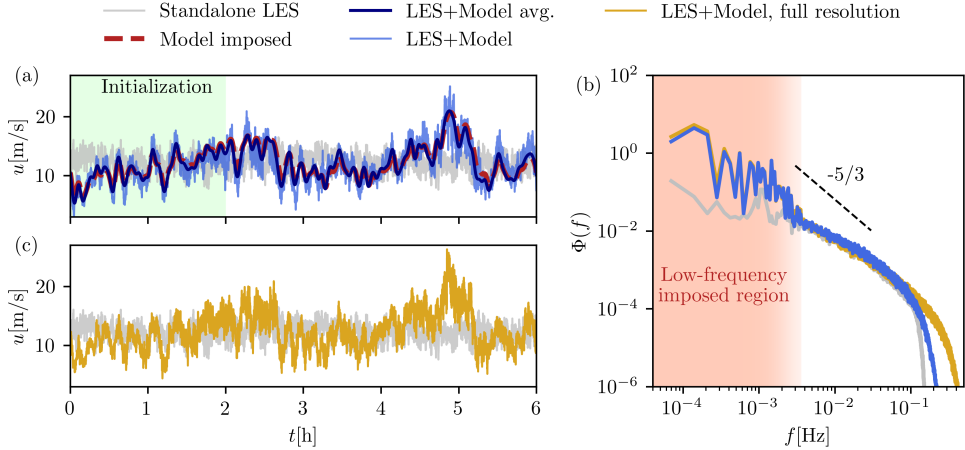


Figure 1.3: Comparison between measured wind speed, standalone LES, and LES including modeled low-frequency variations. (a): time series, (b): power spectrum. The “Model imposed” lines in (a,b) indicate the low-frequency signal in our model. Lines “LES+Model avg.” and “LES+Model” represent the horizontally averaged and locally sampled wind speed signals, respectively. Panel (c) compares the “full resolution” simulation on a  $512 \times 256 \times 128$  grid with standalone LES.

as an initialization phase and use only the last four hours of the 6-hour data for quantitative analysis.

We use the same LES domain and grid setup as described in Section 1.4. Figure 1.3 shows that standalone LES without dynamic forcing lacks the low-frequency variations seen in atmospheric flows. The figure demonstrates that the horizontally averaged velocity from the LES with our model (LES+Model avg.) closely follows the imposed low-frequency wind speed variations (Model imposed). A closer look reveals a slight deviation from the target signal. As discussed in Section 1.4, this overshoot occurs at specific heights due to the response to rapid accelerations, even though the domain-averaged wind speed remains consistent with the imposed forcing. However, we note that these overshoots are small compared to the high-frequency fluctuations visible in the locally sampled signals, see Figures 1.3a and Figures 1.3b.

Figure 1.3c confirms a smooth spectral transition between the low-frequency signal imposed by our modeling approach and the high-frequency turbulence naturally captured by LES. The smooth transition is achieved through the

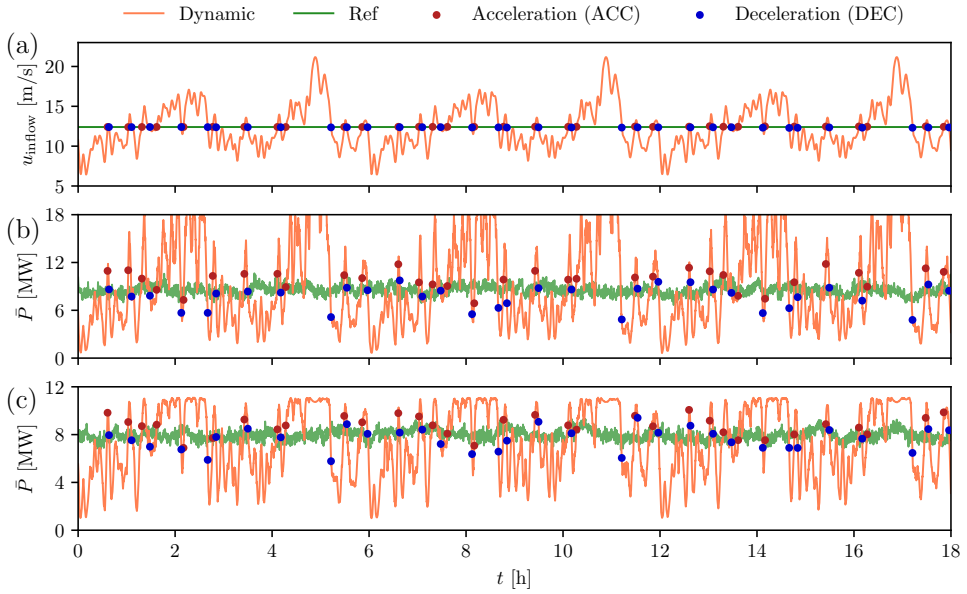


Figure 1.4: (a) Imposed wind speed at hub height, (b) corresponding averaged turbine power production in the wind farm for  $C_T = 0.8$  and (c) power production for dynamic  $C_T$ . The red (accelerating) and blue (decelerating) points indicate when the imposed dynamic wind speed matches the average wind speed (reference case).

Butterworth filter, which gradually adds low-frequency content (timescales longer than several minutes) to the standalone LES, which otherwise only captures turbulent fluctuations up to several minutes. We performed a higher resolution simulation ( $512 \times 256 \times 128$  nodes, labeled “LES+Model, full resolution”) to verify that the low-frequency content stays consistent in higher resolution simulation. Meanwhile, the high-resolution simulation captures more high-frequency content, which is expected because the grid better represents smaller length scales and higher-frequency turbulence events.

## 1.6. EFFECT OF DYNAMIC WIND SPEED VARIATIONS ON WIND FARM PERFORMANCE

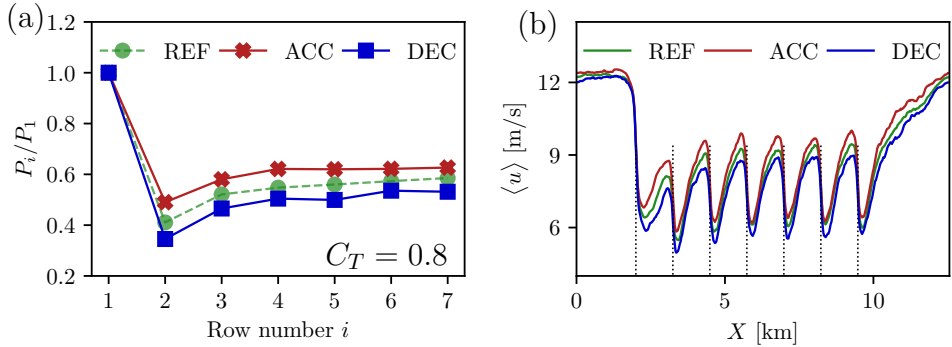


Figure 1.5: Results for idealized scenario with turbines operating at constant  $C_T = 0.8$ . (a) Relative power output per row, (b) streamwise velocity as functions of downstream position for the acceleration, deceleration, and reference scenarios. Vertical dashed lines in panels (b) indicate turbine locations.

## 1.6 Effect of dynamic wind speed variations on wind farm performance

To examine how low-frequency wind speed fluctuations with typical time scales of more than several minutes influence wind farm performance, we simulate a wind farm with 28 DTU 10MW wind turbines [51]. The turbines are arranged in seven rows and four columns, with streamwise spacing of  $7D$  and spanwise spacing of  $5D$ . Simulation runs are conducted on a grid of  $512 \times 256 \times 128$  points within a domain measuring  $12.56 \times 6.28 \times 1 \text{ km}^3$ . Each turbine, modeled with the actuator disk method, is resolved with seven grid points across its diameter, which is enough to capture the main interactions with the ABL [45].

We compare a dynamic case, using the low-pass filtered wind speed signal shown in Figure 1.3c as inflow for 18 hours by repeating a 6-hour segment three times (Figure 1.4a), with a reference case using a constant wind speed equal to the time-averaged value of the dynamic case. In Section 1.6.1, we first consider an idealized academic case with a fixed turbine thrust coefficient of  $C_T = 0.8$ . Section 1.6.2 then presents a more realistic scenario where  $C_T$  varies dynamically according to the EllipSys power curve from Bak et al. [51], which specifies a maximum power of  $P_{\max} \approx 11 \text{ MW}$ .

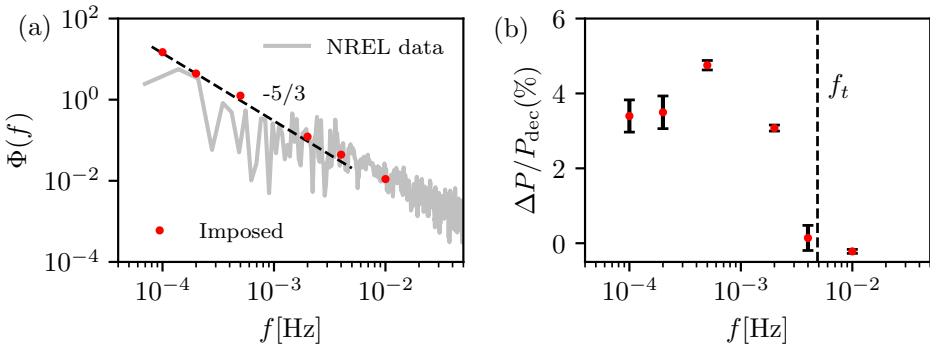


Figure 1.6: Frequency-dependent power asymmetry for idealized scenario with turbines operating at constant  $C_T = 0.8$ . (a) Imposed mono-frequency wind speed variations with amplitudes following a  $f^{-5/3}$  spectral scaling, representative of atmospheric turbulence. (b) Average power difference between acceleration and deceleration periods, showing a consistent gain in power production during acceleration at low frequencies.

### 1.6.1 Wind farm operating at constant $C_T$

We begin with the idealized scenario where all turbines operate at a constant thrust coefficient of  $C_T = 0.8$ , and the resulting wind farm power output over time is shown in Figure 1.4b. The figure highlights moments when the wind speed in the dynamic scenario matches the average wind speed from the reference case. These moments are categorized based on whether the flow is speeding up or slowing down. When the flow accelerates, the wind farm produces more power than in the reference case. Conversely, during deceleration, the power output is below the reference case at the same inflow wind speed.

Figure 1.5 shows the power output normalized by the production of the first row. The results indicate that flow acceleration and deceleration significantly impact the performance of downstream rows. During acceleration, turbines from the second row onward generate more power than in the reference case. This relative increase comes from higher wind speeds starting at the second row, as shown in Figure 1.5b. This illustrates that wake effects under dynamic atmospheric conditions differ from those under stationary conditions.

In the acceleration scenario, wind speeds near downstream turbines are higher as there is a weaker velocity deficit caused by upstream turbines. This is because the wake deficit scales with  $u_\infty - u_{\text{disc}} \propto u_\infty$ , so lower past wind speeds  $u_\infty$  lead to weaker wakes that are carried downstream. Consequently, downstream turbines benefit from more favorable inflow conditions and produce more power than in the reference case. Conversely, in the deceleration scenario, higher past wind speeds generate stronger upstream wakes, which are carried downstream and decrease the power output of downstream turbines.

The dynamic wake effects at time  $t$ , which influence downstream turbine performance, are mainly driven by prior wind speed changes, expressed as  $\Delta U = U(t) - U(t - \Delta t)$ , where  $\Delta t = \Delta x / \bar{U}$  is the wake travel time between turbines. This highlights the role of low-frequency wind speed fluctuations, since the effects of higher-frequency changes tend to cancel within  $\Delta t$  due to alternating acceleration and deceleration. We define the transition frequency for this effect as  $f_t = (2\Delta t)^{-1}$ ; for  $f > f_t$ , no sustained acceleration or deceleration occurs within  $\Delta t$ . To test whether wake travel time correlates with observed performance changes, we performed simulations with wind speed variations at specific frequencies. The chosen frequencies follow the  $f^{-5/3}$  spectral slope characteristic of atmospheric turbulence, as observed in the NREL field measurements noted above (Figure 1.6a), and span  $10^{-4}$  to  $10^{-2}$  Hz, corresponding to timescales from about 2.8 hours to 1.7 minutes.

Figure 1.6b shows that below the transition frequency  $f_t$ , the power output during acceleration events is typically about 3%–5% higher than during deceleration. This difference is smaller than in Figure 1.5a, likely because that the model spectrum accounts for the combined influence of all low-frequency components. The transition frequency  $f_t$  corresponds to twice of the average wake travel time between consecutive downstream turbines, which in our case is about  $5 \times 10^{-3}$  Hz (approximately 3min). While lower frequencies represent slower wind speed changes, their fluctuation amplitude increases with the spectral scaling  $\Phi(f) \sim f^{-5/3}$ . These opposing effects yield a persistent  $\Delta U$  at low frequencies, producing a nearly constant power difference between acceleration and deceleration events in this range. For  $f > f_t$ , this difference vanishes as high-frequency fluctuations cancel over the wake travel time  $\Delta t$  due to alternating acceleration and deceleration.

### 1.6.2 Wind farm operating at dynamic $C_T$

Figure 1.4c shows the wind farm’s power output, where the turbine thrust coefficient dynamically adjusts to the incoming wind speed following the EllipSys power curve [51]. Peak power production occurs at an inflow velocity of approximately  $u_{\text{inflow}} = 15 \text{ m/s}$ , as this allows turbines operating in wake conditions to consistently reach rated power. This produces an asymmetry in the turbine power response to the incoming wind flow. Figure 1.7 shows the power output normalized by the first row’s production. While the overall trends resemble those in the constant  $C_T$  case, some differences are apparent, particularly for the second row. This can be explained by the first-row turbines often operating in the above-rated regime (Figure 1.7b), where  $C_T$  decreases as wind speed increases. In the acceleration scenario, lower upstream wind speeds cause the first-row turbines to operate at higher  $C_T$ , partly offsetting the weaker wakes expected from lower wind speeds. In the deceleration scenario, higher upstream wind speeds yield lower  $C_T$  values, which reduces wake strength and diminishes the influence of stronger inflow.

It is important to note that the power differences shown in Figure 1.7 depend on the specific characteristics of the wind speed signal and on the wind speed level selected for comparison. The magnitude of the acceleration and deceleration effects can vary with the chosen analysis intervals. For example, Figure 1.7a shows an asymmetric response relative to the reference case, with the normalized power output during deceleration more closely matching the reference than during acceleration. Examination of Figure 1.7b indicates that this is because the downstream wind speed during deceleration is closer to the reference than during acceleration. As seen in Figure 1.4a, most deceleration events occur immediately after acceleration phases, causing the effects to partially overlap.

Considering the aggregate power output over the entire time period in Figure 1.4c, the wind farm produces less power under dynamic wind inflow (orange line) than in the corresponding reference scenario (green line). Under stationary inflow at the mean wind speed, production is near maximum capacity (Figure 1.4c). In high-wind periods, turbines reach maximum output quickly, so gains are small, while in low-wind periods production drops sharply, reducing overall output. In contrast, for the idealized constant thrust coefficient scenario with  $C_T = 0.8$ , dynamic inflow yields a power gain. This results from the cubic dependence of power on inflow velocity ( $P \sim U_\infty^3$ ), where gains dur-

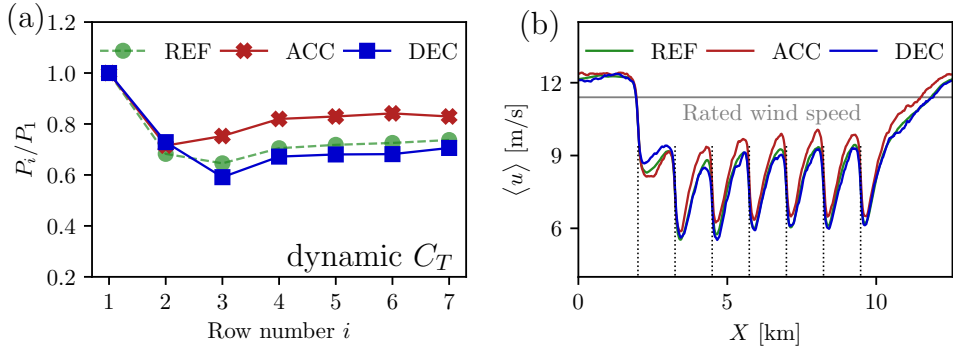


Figure 1.7: Results for turbines operating according to DTU 10MW power curve. (a) Relative power output per row, (b) streamwise velocity as functions of downstream position for the acceleration, deceleration, and reference scenarios. Vertical dashed lines in panels (b) indicate turbine locations.

ing high-wind periods outweigh losses during low-wind periods. Overall, these effects are scenario-specific and depend on turbine design and control. While a full exploration of all cases is beyond the scope of this work, the proposed method enables such investigations under controlled conditions.

## 1.7 Conclusions

We present a method for incorporating low-frequency wind speed variations into large-eddy simulations (LES) of wind farms. Traditional standalone LES often miss these dynamics because they arise from large-scale atmospheric processes, whereas most studies assume steady inflow. Our approach introduces low-frequency fluctuations by dynamically adjusting the velocity of a non-inertial reference frame. Combined with the concurrent precursor method, it preserves mass conservation, which is often challenging when modifying inflow in turbulence simulations. The implementation is straightforward and validated through multiple test cases, reproducing both idealized and field-measured low-frequency wind speed variations within LES and ensuring smooth transitions to the high-frequency turbulence naturally resolved by LES. This capability enables controlled, systematic investigations of how

low-frequency fluctuations affect wind farm dynamics.

The results show that low-frequency wind speed variations can significantly impact wind farm performance. When the wind accelerates, downstream turbines experience reduced wake losses, whereas during slowdowns, wake effects are stronger. These effects are controlled by the advection time for wakes to travel between successive downstream turbines and disappear when wind speed fluctuations occur on shorter timescales. Because standalone LES do not resolve low-frequency dynamics, they must be modeled explicitly, as done in this study. Results also differ between turbines operating at a fixed thrust coefficient and those following a realistic power curve, highlighting the role of turbine-response dynamics. This scenario dependence arises from the asymmetric and nonlinear response of turbines to changing inflow, since both thrust coefficient and wake evolution depend on wind speed and turbulence intensity. We therefore expect these effects to vary with atmospheric stability and wind farm layout.

The current study applies the approach to model wind speed variations in neutral atmospheric conditions. The method can be readily adapted for stable and unstable boundary layers and combined with previous approaches for modeling wind direction changes [33]. A key advantage is the controlled introduction of low-frequency wind speed variations at hub height, which is particularly valuable for understanding their impact on wind farm performance and control. The approach also supports the development of simulation frameworks in which LES are driven by outputs from large-scale weather models or measurement data [19, 29]. Future work could explore prescribing variations in geostrophic wind speed rather than near-surface velocity to better represent large-scale atmospheric dynamics. The scenario-dependent nature of the results highlights the need for further investigation into the influence of large-scale atmospheric fluctuations on wind farm performance.

# 2

## Atmospheric boundary layer response to the dynamic geostrophic wind forcing<sup>◦</sup>

The combined influence of geostrophic forcing, Coriolis effects, and turbulence governs the dynamics of the atmospheric boundary layer (ABL). While most studies focus on steady-state conditions, real wind fields evolve continuously in time. Here, we investigate the transient ABL response to time-varying geostrophic forcing. Large-eddy simulations (LES), driven by a dynamic pressure-gradient force, accurately reproduce geostrophic wind variations derived from mesoscale simulations or field measurements. Building on the damped-oscillator framework, we develop a reduced-order model that accounts for geostrophic forcing, Coriolis effects, and turbulence. This model captures the interaction between the ABL and the geostrophic layer, and validation against LES of conventionally neutral boundary layers confirms its ability to reproduce the essential dynamics. The proposed framework advances understanding of unsteady ABL behavior. It provides a computationally efficient tool for generating realistic inflow conditions in wind-energy applications, with potential extensions to other boundary-layer regimes and diurnal cycles.

---

<sup>◦</sup>In preparation as: Y. Liu and R.J.A.M. Stevens, *Atmospheric boundary layer response to the dynamic geostrophic wind forcing*.



## 2.1 Introduction

Wind farms operate in the lower part of the atmospheric boundary layer (ABL), which is driven by the large-scale geostrophic wind above [4, 27, 52]. The ABL is typically capped by a thermally stratified layer known as the capping inversion, which suppresses turbulence and limits mixing with the free atmosphere. Above this inversion, the geostrophic wind results from a balance between the large-scale pressure gradient force and the Coriolis force. Within the ABL, turbulence is generated by surface friction, creating drag and a wind veer that varies with height.

The typical structure of ABL is displayed in Figure 2.1a, where a neutral condition is considered inside the boundary layer. Such a simplified case is often referred to as a conventional neutral boundary layer. The drag force induced by ABL turbulence partially offsets the large-scale pressure gradient, resulting in a height-dependent shift in wind directions within the ABL. The relative surface drag  $u_*/G$  and wind veer at the surface (cross-isobaric angle  $\alpha_0$ ) can be estimated by the geostrophic drag law [53], which considers the effect of geostrophic wind speed, Coriolis effects, and turbulence. The geostrophic drag law links the large-scale, pressure-driven flow in the free atmosphere, arising from geostrophic balance, to the slower near-surface wind shaped by turbulence and friction. It provides a simplified framework to estimate the drag on the atmospheric boundary layer and the resulting deflection of the wind across isobars. Nevertheless, the classical geostrophic drag law only considers the truly neutral boundary layers. In ABLs the turbulence development is suppressed by the capping inversion layer. To account for these buoyancy effects, Liu et al. [17, 18] proposed stability corrections to capture the flow structure under different capping strengths above the ABL.

Large-eddy simulations (LES) provide a powerful tool for studying atmosphere-wind farm interactions under controlled conditions; however, they are typically restricted to domains of only a few kilometers and can only resolve small-scale boundary-layer structures. As a result, most wind farm LES assume stationary geostrophic forcing with fixed inflow speed and direction. In reality, however, the geostrophic wind evolves throughout the day, influencing both ABL dynamics and wind farm performance [33, 52, 54]. These low-frequency variations, driven by mesoscale weather systems that span hundreds of kilometers, are absent in most LES. Mesoscale models, such as the Weather Research and Forecasting (WRF) model, can capture such variations;

however, their coarse resolution prevents them from resolving the detailed interaction between wind farms and the atmosphere [29, 43, 55]. Advancing the understanding of atmosphere–wind farm interactions requires new modeling approaches that capture the ABL response to time-varying geostrophic forcing in high-resolution LES.

Momen and Bou-Zeid [56–58] proposed that ABL dynamics can be represented as a damped oscillator. In this framework, perturbations in wind speed or wind direction trigger oscillations in the boundary layer, with the dominant frequency set by the Coriolis frequency  $f_C$ . Turbulent dissipation acts as the damping mechanism, reducing these oscillations and restoring equilibrium. Thus, the Coriolis frequency and turbulence intensity define the intrinsic timescales of ABL dynamics. The boundary-layer response to external forcing is governed by the interplay between Coriolis oscillations and turbulent damping, with variations in geostrophic forcing serving as the external excitation. Here, we will extend this modeling approach and investigate the coupled dynamics of geostrophic wind and ABL flow.

Variability in the geostrophic wind is primarily driven by mesoscale processes, with typical timescales ranging from 15 minutes to several hours. For comparison, the Coriolis timescale can be estimated as  $\tau_C = 2\pi/f_C \approx 17.4$  h for  $f_C = 10^{-4}$  Hz, representative of midlatitudes at 45°N. The largest eddy turnover time in the ABL can be approximated as  $\tau_t \approx h/u_*$ , where  $h$  is the boundary-layer height and  $u_*$  the surface friction velocity [59]. For  $h = 1000$  m and  $u_* = 0.4$  ms<sup>-1</sup>, this yields a turbulence recovery time of less than one hour. Since the Coriolis period is far longer than both the turbulence timescale and the adjustment time of geostrophic forcing, the ABL is subject to continuous dynamic changes, indicating the importance of modeling these phenomena.

Here, we introduce a time-varying geostrophic forcing scheme to investigate how dynamic changes in geostrophic wind speed influence ABL dynamics. The geostrophic forcing driving wind-speed variations is decomposed into components parallel and perpendicular to the mean wind direction. Validation with LES demonstrates that this approach accurately reproduces imposed dynamic geostrophic wind signals. Within the ABL, imbalances in the forcing induce changes in both wind speed and direction. To capture and interpret these dynamics, we develop a reduced-order model that combines the damped oscillator framework with the geostrophic drag law for ABLs, thereby predicting the dynamic evolution of flow characteristics in conventionally neutral boundary layers.

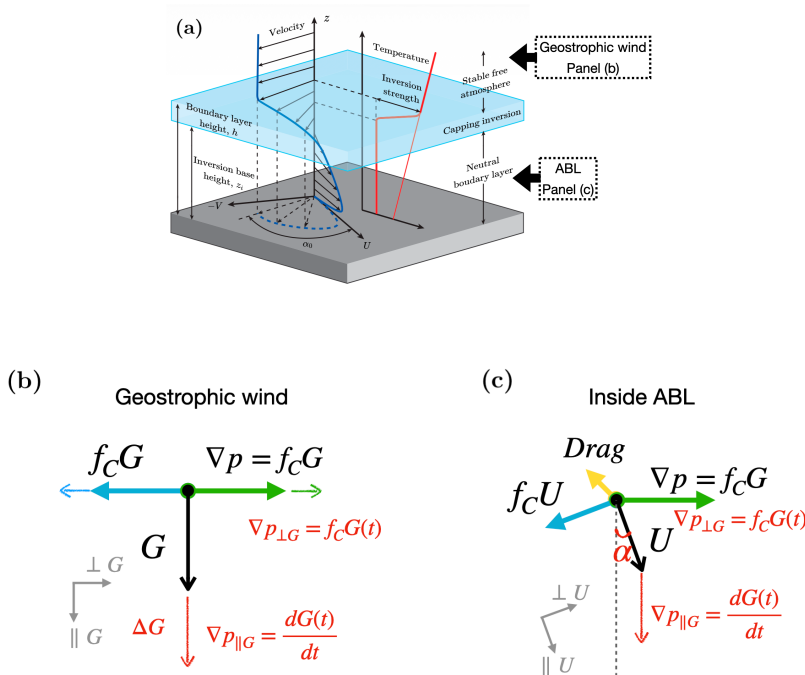


Figure 2.1: Flow structure and forcing balance in the conventionally neutral boundary layers driving the geostrophic wind, illustrated in the Northern Hemisphere. (a) Sketch of wind and temperature profiles in height; (b) The top view of the forcing balance in the geostrophic layer (above the capping inversion) and (c) inside the ABL (below the capping inversion). The dynamic pressure-gradient forcing responsible for generating the time-varying geostrophic wind is highlighted in red.

Figure 2.1 illustrates the geostrophic forcing balance in a steady atmosphere. Above the capping inversion, ABL turbulence is suppressed, and the geostrophic wind speed  $G$  arises from the balance between the pressure-gradient force and the Coriolis force, i.e.,  $G = -\nabla p/f_C$ , where  $f_C$  is the Coriolis frequency. We represent the dynamic geostrophic wind as a time

series describing variations in both wind speed and direction.

$$\vec{G}(t) = \begin{bmatrix} G(t) \\ \theta(t) \end{bmatrix}. \quad (2.1)$$

Here  $G(t)$  and  $\theta(t)$  denote the time series of geostrophic wind speed and direction, respectively. For consistency, the forcings are expressed in the geostrophic coordinate system relative to the wind direction of  $\vec{G}$ , denoted by the subscripts  $\parallel_G$  and  $\perp_G$ , see Figure 2.1b. We first consider variations in wind speed  $G(t)$  under a fixed geostrophic wind direction, i.e.,  $\dot{\theta}(t) = 0$ . According to Newton's second law, the force driving the momentum increase is given by the time derivative  $\dot{G}(t)$ . In the perpendicular direction, the pressure-gradient force that balances the Coriolis force evolves dynamically with  $G(t)$ . Hence, the pressure-gradient forcing can be expressed as:

$$\nabla P_G(t) = \begin{bmatrix} F_{\parallel G} \\ F_{\perp G} \end{bmatrix} = \begin{bmatrix} \dot{G}(t) \\ f_C G(t) \end{bmatrix} \quad (2.2)$$

Here, the subscript  $\square_G$  indicates that the forcing vector is expressed in geostrophic coordinates. We assume ideal barotropic conditions, so the large-scale dynamic pressure gradient is constant with height. Within the ABL, this pressure gradient is balanced by the Coriolis force  $f_C U$  and turbulent drag (see Figure 2.1b). Consequently, a wind veer develops in the boundary, characterized by a relative angle  $\alpha(z)$  between the local wind and the geostrophic wind (see Figure 2.1). To account for this, we rotate the geostrophic coordinate system by  $\alpha(z)$  and define a local coordinate system (denoted by  $\square_A$ ) aligned with the wind direction  $\vec{U}(z)$ . In this local coordinate system, the initial-state velocity is  $\vec{U}_A(z) = [U(z), 0]^T$ , and the governing dynamic equations at height  $z$  can be written in this rotated frame.

$$\dot{\vec{U}}_A(z) = \begin{bmatrix} \dot{U} \\ \dot{V} \end{bmatrix} = \mathbf{R}_{G \rightarrow A}(z) \nabla P_G - \begin{bmatrix} 0 \\ f_c \end{bmatrix} U(z) + \mathbf{R}_{G \rightarrow A}(z) \vec{D}_G(z) \quad (2.3)$$

Here  $\mathbf{R}_{G \rightarrow A}(z) = \begin{bmatrix} \cos \alpha & -\sin \alpha \\ \sin \alpha & \cos \alpha \end{bmatrix}$  denotes the rotation matrix that projects the pressure-gradient forcing from the geostrophic coordinate system ( $\square_G$ ) to the ABL coordinate system ( $\square_A$ ) at height  $z$ . In Eq. 2.3, the first term on the right-hand side represents the pressure-gradient force, while the second and third terms correspond to the Coriolis force and the turbulent drag force, respectively. As illustrated in Figure 2.1, Eq. 2.3 shows that dynamic variations in geostrophic wind speed induce changes in both the streamwise ( $U$ )

and spanwise ( $V$ ) velocity profiles in the lower ABL. The coupling of wind speed and direction between the geostrophic flow and the boundary layer distinguishes this system from steady-state turbulent boundary layers.

Similarly, for variations in geostrophic wind direction  $\theta(t)$ , we represent the dynamic pressure-gradient forcing applied to the lateral component as:

$$\nabla P_G = \begin{bmatrix} 0 \\ \dot{\theta}(t)G(t). \end{bmatrix} \quad (2.4)$$

Note that the rotation of the geostrophic coordinate system follows the change in wind direction, such that  $\nabla P_G$  always acts in the perpendicular direction. This forcing scheme, therefore, decouples directional changes in the geostrophic flow from variations in wind speed, allowing for the examination of their individual effects. Nevertheless, directional deflection  $\alpha$  within the ABL still induces dynamic changes in both wind speed and direction. Here, we focus on wind-speed variations, where capturing the non-equilibrium turbulence state poses a particular challenge for modeling  $\vec{D}(z)$ .

## 2.3 Turbulence parameterization

Eq. 2.3 provides insight into the dynamic ABL response to changing geostrophic wind conditions. While the first two terms on the right-hand side can be determined analytically, representing the turbulence contribution remains challenging. In reality, the boundary layer structure is continuously influenced by dynamically changing weather conditions. For simplicity, we neglect structural changes due to varying thermal conditions. This assumption limits the dynamics to a timescale of several hours, which is shorter than the diurnal cycle. We demonstrate the effectiveness of the turbulence parameterization in conventionally neutral boundary layers, characterized by neutral stratification within the boundary layer and stable stratification aloft. The proposed methodology, however, is general and applicable to other types of ABLs.

### 2.3.1 Geostrophic drag law for stationary velocity profiles

The well-known logarithmic law of the wall is widely used to describe the velocity profile in boundary layers. In an ABL, the Coriolis effect plays a

crucial role in flow dynamics; therefore, it cannot be overlooked. The classic geostrophic drag law accounts for the forcing balance due to the Coriolis effect, and connects the geostrophic wind to the wind at the surface [60, 61]. Liu et al. [17, 18] proposed a universal formulation for stationary conventionally neutral boundary layers, where the vertical structure of the boundary layer flow is determined by two dimensionless parameters: the Rossby number ( $Ro$ ) and the Zilitinkevich number ( $Zi$ ). The Rossby number is defined as  $Ro = u_*/(f_C z_0)$ , where  $u_*$  is the friction velocity,  $f_C$  is the Coriolis parameter, and  $z_0$  is the surface roughness length. A large  $Ro$  indicates that flow inertia dominates over the Coriolis effect. The Zilitinkevich number,  $Zi = N/f_C$ , characterizes the relative influence of thermal stability compared to the Coriolis effect, with  $N$  denoting the Brunt-Väisälä frequency.

The turbulent shear stress is expressed as a function of the dimensionless altitude  $\xi = z/h \in [0, 1]$ , which specifies the relative position within the ABL. Using this coordinate system, the turbulence parameterization can be written as:

$$\frac{d\tau_x}{d\xi} = -f_C h(V - V_G) \quad , \quad \frac{d\tau_y}{d\xi} = f_C h(U - U_G), \quad (2.5)$$

Where the velocity profile relative to the geostrophic background flow is given by:

$$\kappa \frac{U - U_G}{u_*} = \ln \xi + a(1 - \xi) + a_\psi \psi \quad , \quad \kappa \frac{V - V_G}{u_*} = B(1 - \xi) + b_\psi \psi, \quad (2.6)$$

The constants in the velocity profiles of Eq. 2.6 are obtained from the geostrophic drag law for conventionally neutral ABL, which has been validated against both LES data and atmospheric measurement campaigns [17, 18]. Above the ABL ( $\xi > 1$ ), the turbulent shear force decreases as the wind speed approaches the geostrophic background velocity. All equations are expressed in the ABL coordinate system referenced to the ground. The turbulent force is projected into the geostrophic coordinate system using the cross-isobaric angle  $\alpha_0$ , which depends on  $Ro$  and  $Zi$  as defined based on geostrophic drag law theory:

$$\vec{D}_G(\xi) = \begin{bmatrix} \frac{d\tau}{d\xi} \|_G \\ \frac{d\tau}{d\xi} \perp G \end{bmatrix} = \begin{bmatrix} \frac{d\tau_x}{d\xi} \cos(\alpha_0) - \frac{d\tau_y}{d\xi} \sin(\alpha_0) \\ \frac{d\tau_x}{d\xi} \sin(\alpha_0) + \frac{d\tau_y}{d\xi} \cos(\alpha_0) \end{bmatrix} \quad (2.7)$$

Analytical profiles of the turbulent shear stress  $\tau_x$ ,  $\tau_y$  can be directly obtained from Eq. 2.5 and 2.6 as functions of  $Ro$  and  $Zi$  [17, 18]. This connects the response of ABL dynamics to the geostrophic drag law, which is considered

for stationary and equilibrium ABLs. Nevertheless, we will demonstrate that in dynamic cases, the geostrophic drag law remains effective as a damping force in ABL dynamics, which can be incorporated into the damped-oscillator model proposed by Momen and Bou-Zeid [62].

### 2.3.2 Dynamic response of ABL to perturbations

When the geostrophic wind speed varies dynamically, the force balance in the ABL is disrupted, causing both wind speed  $U(z)$  and wind direction  $\alpha(z)$  to deviate from their equilibrium profiles. Turbulent shear stress acts to stabilize the dynamics and restore the flow toward the stationary state determined by the prevailing geostrophic wind. We evaluate this damping effect by numerically solving Eq. 2.3, using the turbulence parameterization in Eq. 2.7 to model  $\vec{D}_G(z)$ . In these simulations, the geostrophic wind speed is fixed at  $G = 10$  m/s (corresponding to  $Ro = 4.2 \times 10^4$ ) and the boundary-layer height at  $h = 1000$  m. We introduce an initial perturbation at  $z = 150$ m, and check the temporal evolution at the same height.

Figure 2.2 shows the response of the ABL to the wind-speed or wind-direction perturbation applied at  $t = 0$  h. A deviation in either variable induces oscillations in both wind speed and wind veer, corresponding to the Coriolis frequency  $f_C = 10^{-4}$  s<sup>-1</sup>, demonstrating that the Coriolis force dynamically couples wind speed and direction in the ABL. With the geostrophic wind held constant, turbulence damps the initial perturbation. It drives the flow back toward its stationary state, which is uniquely determined by the current geostrophic wind speed  $G(t)$ . The recovery time is longer than a day, indicating that the ABL cannot, in practice, reach an stationary state.

## 2.4 Modeling dynamic wind speed changes

Under dynamic wind speed changes, the ABL structure undergoes sustained modification, resulting in a dynamic interplay between Coriolis and turbulence effects. The reduced-order model (Eq. 2.3) provides a semi-analytical framework to capture the space-averaged unsteady ABL dynamics at different elevations. We demonstrate the predictive ability of the model by comparing it with LES results, where time-varying geostrophic wind speed signals are imposed in both the LES and the model.

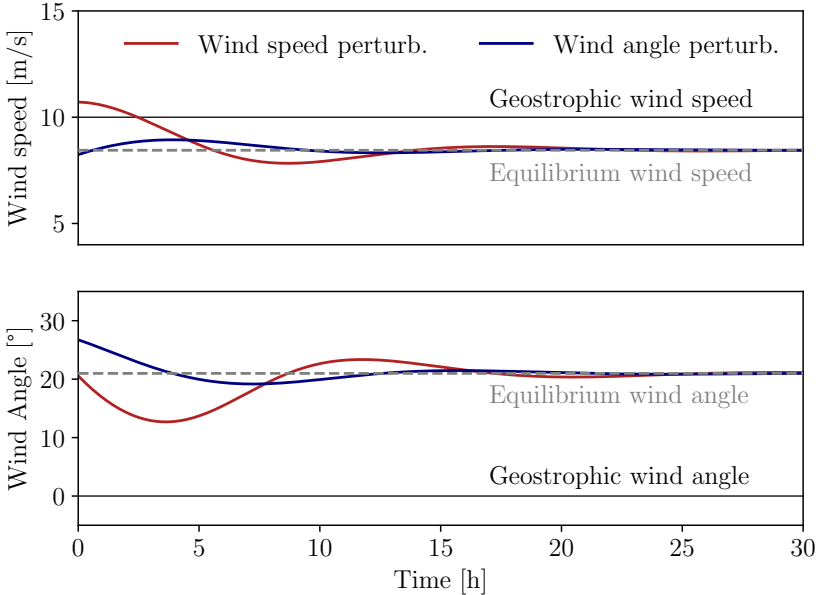


Figure 2.2: Time series of wind speed and angle at  $z = 150\text{m}$  under an imposed wind speed (red lines) and wind angle (blue lines) perturbation. Dashed lines indicate the positions in equilibrium ABLs.

We utilize the simulation code developed by Albertson [24] and validated by Gadde et al. [46], which includes the details of the numerical code provided in Appendix 2.A. Using this code, LES of conventionally neutral boundary layers are performed with a simulation domain spanning  $6.28\text{km} \times 6.28\text{km} \times 2\text{km}$  in the longitudinal, lateral, and vertical directions, discretized with  $128^3$  grid points. The temperature profile is initialized with  $\theta_0 = 286\text{ K}$  inside the ABL up to a height of 1 km. A capping inversion layer is imposed between 1 and 1.2 km with a temperature jump of 3 K, and above this, the atmosphere is stably stratified with a lapse rate of 5 K/km. The initial velocity is set to the geostrophic wind, after which the boundary-layer flow is allowed to develop naturally. The dynamic forcing is applied after the ABL reaches equilibrium at  $t = 36\text{ h}$ . A surface roughness length of  $z_0 = 0.1\text{ m}$  and a Coriolis frequency of  $f_C = 10^{-4}\text{ Hz}$  are used, representative of flat grassland terrain at a latitude of  $45^\circ\text{N}$ .

In solving Eq. 2.3, we use the geostrophic wind speed  $G(t)$  and the ABL height  $h$  as the control parameters to model  $\vec{D}_G(z)$  instead of  $Ro$  and  $Zi$ . Note that  $Ro$  and  $Zi$  are considered to describe steady conventionally neutral

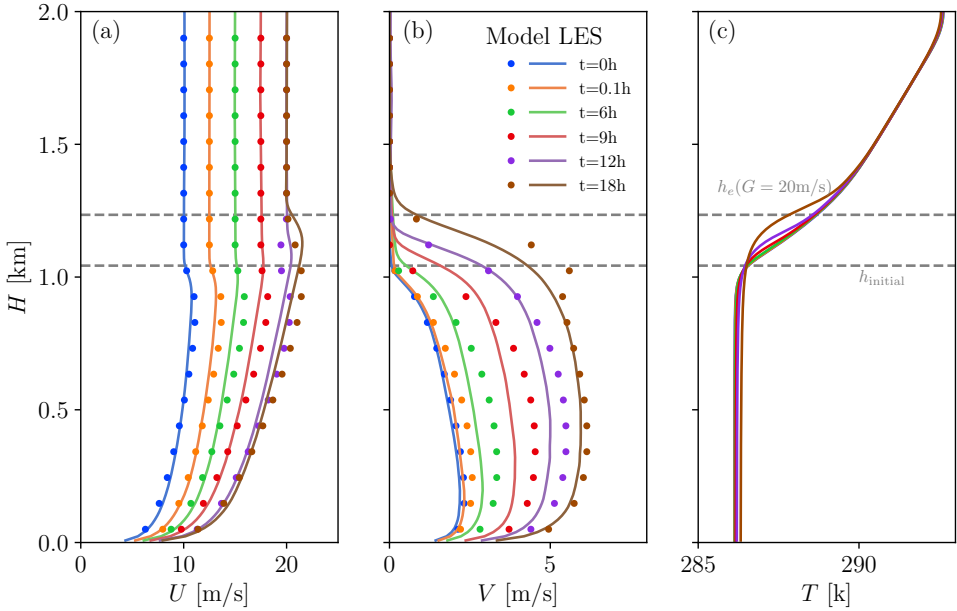


Figure 2.3: Temporal evolution of (a) streamwise velocity ( $U$ ), (b) spanwise velocity ( $V$ ), and (c) temperature profiles during a 12-hour acceleration of the geostrophic wind from  $10$  to  $20\text{ ms}^{-1}$ , starting at  $t = 0$ . LES results are shown as solid lines, and dots represent model predictions at discrete elevations. The legend applies to all panels.

boundary layers that achieve full turbulence and thermal equilibrium. In dynamic scenarios, the capping inversion height  $h_{\text{cap}}$  often mismatches the equilibrium height  $h_e$  that is determined by free-atmospheric lapse rate. Therefore,  $G(t)$  and  $h$  better describe the state of turbulence in these situations.

#### 2.4.1 Dynamic response to slowly varying geostrophic wind speed

We first consider a linear increase in geostrophic wind speed from  $G = 10$  to  $20\text{ ms}^{-1}$  over a 12-hour period, a timescale sufficiently larger than the eddy turnover timescale  $\tau_t \approx 1$  hour. The flow is assumed to remain in a quasi-equilibrium state during the acceleration, allowing the equilibrium turbulence model to be applied directly to the prescribed  $G(t)$ . For the case considered here with  $Zi = 130$ , the equilibrium ABL height  $h_e$  remains below the imposed inversion height  $H = 1000$  m until  $G = 15\text{ m s}^{-1}$ . Accordingly, in modeling

$\vec{D}_G(z)$ , the effective boundary-layer height is taken as  $h(t) = \min(h_e(t), H)$ .

Figure 2.3 shows velocity profiles at different times, with the velocity components  $U$  and  $V$  expressed in geostrophic coordinates. The dynamic forcing in LES begins at  $t = 0$  h, when the ABL flow is in equilibrium for  $G = 10 \text{ m s}^{-1}$ , corresponding to a boundary-layer height of  $h = 1043 \text{ m}$ . The results demonstrate that the geostrophic drag law accurately reproduces the steady-state velocity profiles at  $t = 0$  h, confirming the validity of the proposed turbulence parameterization even when  $h_e < H$ .

When the geostrophic wind speed increases, the wind speed  $U(t)$  in the boundary layer follows the change in the geostrophic layer  $G(t)$ , and the model captures this trend well. The differences between LES and model results are mainly due to errors in predicting the boundary-layer height. As shown in Figure 2.3b, the model underestimates the boundary layer height at  $t \approx 6$  h and overestimates it at later times. This discrepancy arises from the influence of stratification strength in the capping layer, rather than that of the free atmosphere, which is accounted for in  $h_e$ . Figure 2.3c shows the evolution of the temperature profile at different times. For  $t < 6$  h, the capping layer remains unaffected, allowing  $h$  to increase slightly as the available momentum grows. Once  $h_e > H$  after  $t = 6$  h ( $G > 15 \text{ m s}^{-1}$ ), turbulence generates a downward heat flux, sharpening the capping inversion and limiting further growth of the boundary layer. From  $t = 12$  h to  $t = 18$  h, the model assumes a fixed equilibrium boundary layer height under steady geostrophic wind speed at  $20 \text{ m s}^{-1}$ . The temperature profile from LES shows further development, as the interface between ABL and free atmosphere is not adiabatic. Consequently, the development of boundary layer height is not fully captured by the model. At  $t = 18$  h, where the ABL flow reaches steady state, the model agrees with LES results in the velocity profiles (Figure 2.3a, b) at the lower part of ABL. Nevertheless, deviations are evident at the top part of ABL, as the flow dynamics near the capping inversion are influenced not only by the instantaneous boundary-layer height but also by its prior evolution.

#### 2.4.2 Response of the ABL to rapid geostrophic wind changes

We next consider a rapid change in wind speed, in which the geostrophic flow accelerates from  $G = 10$  to  $20 \text{ m s}^{-1}$  within 5 minutes. In contrast to the slow-acceleration case, this timescale is too short for turbulence to adjust (recovery time  $\sim 1$  h). As a result, the turbulence remains effectively frozen during the

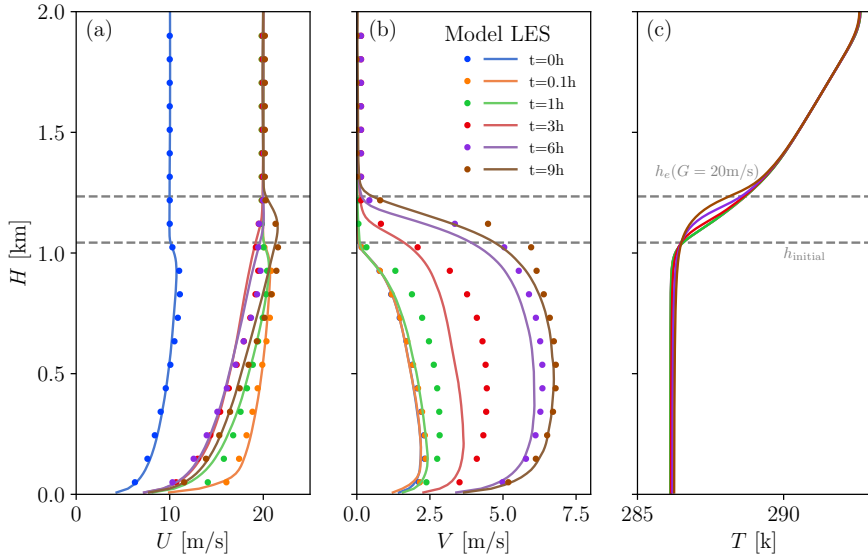


Figure 2.4: Temporal evolution of (a) streamwise velocity ( $U$ ), (b) spanwise velocity ( $V$ ), and (c) temperature profiles. The geostrophic wind is accelerated from  $10$  to  $20 \text{ ms}^{-1}$  over  $5$  minutes, starting at  $t = 0 \text{ h}$ . LES results are shown as solid lines, and dots represent model predictions at discrete elevations. The legend applies to all panels.

acceleration and then relaxes gradually toward the new stationary state once the geostrophic forcing ceases. Figure 2.4 presents LES results up to  $t = 9 \text{ h}$ . Immediately after the acceleration stops ( $t = 0.1 \text{ h}$ ), the streamwise velocity  $U$  is influenced across all heights by the geostrophic forcing, with an over-acceleration evident in the lower part of the ABL that gradually converges to the new equilibrium profile. By  $t = 9 \text{ h}$ , the equilibrium wind profile is fully recovered and matches the shape shown in Figure 2.3. In contrast, the cross-geostrophic component  $V$  exhibits a delayed response, beginning to develop only after about  $t = 1 \text{ h}$ .

To further investigate this behavior, we analyze the time evolution of turbulence and thermal conditions during the dynamic process using LES results, displayed in Figure 2.5a, b. The ABL height  $h$  is defined as the elevation at which  $V(z)$  decreases to 5% of its maximum value within the boundary layer. Turbulence intensity is quantified by fitting the wind-speed variance from the surface to the top of the ABL. For simplicity, we adopt the universal

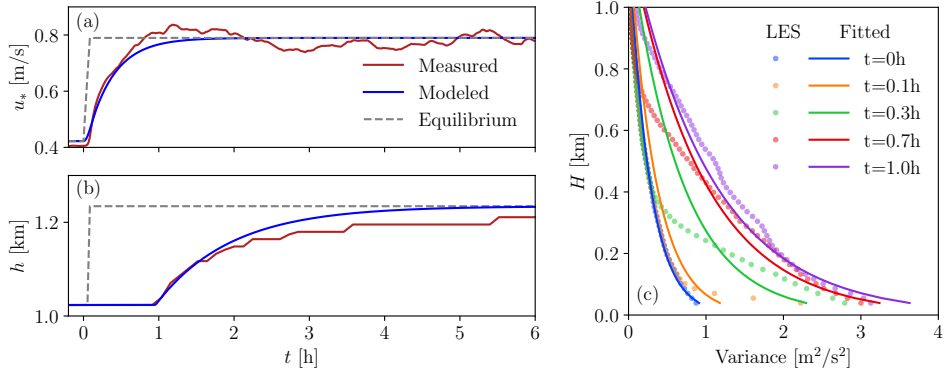


Figure 2.5: Time series of (a) friction velocity, (b) boundary layer height, and (c) vertical profile of variance in LES compared to analytical model results using the stationary geostrophic drag law profiles. Blue lines in panel (a) and (b) indicate the modeled development of turbulence and boundary height in Eq. 2.9, and dashed lines are the equilibrium state for the imposed geostrophic wind speed at that moment.

law-of-the-wall for velocity variance [63–65], expressed as

$$\text{Var} \left( \sqrt{u^2(z) + v^2(z)} \right) / u_*^2 = B_1 - A_1 \log(z/h) \quad (2.8)$$

where  $A_1 = 1.61$  and  $B_1 = 0.3$  are determined from LES. The time series of  $u_*$  and  $h$  during the first six hours are shown in Figure 2.5. Compared to the equilibrium state (dashed lines), both quantities exhibit a delayed adjustment. The turbulence, represented by  $u_*$ , recovers on a timescale of about 1 h, consistent with the estimate  $\tau_t = H/u_* \approx 0.7$  h. The boundary-layer height  $h$  converges more slowly, with a delay of about  $t \approx 1$  h, corresponding to the typical turbulence recovery time.

Figure 2.5c shows turbulence forming near the surface and propagating upward. Vertical profiles of wind-speed variance are compared with the analytical fit from Eq. 2.8. Unlike the model assumption of uniform development, the LES reveals a height-dependent response: near the surface, fluctuations adjust almost instantly, whereas at  $t = 1$  h the variance at the top of the ABL begins to change, marking the onset of boundary-layer growth. Because the boundary-layer height reflects the balance between stratification and turbulent mixing, the turbulence timescale  $\tau_t$  characterizes this delay. After  $t = 1$  h,  $u_*$  gradually approaches equilibrium, but full thermal adjustment requires more than six hours, considerably longer than the turbulence recovery.

To model the transitional behavior of  $u_*$  and  $h$ , we introduce modified control parameters  $G_m$  and  $h_m$  in the turbulence model  $\vec{D}_G(G_m, h_m)$ , where a recursive filter is applied to account for the time delay:

$$\begin{aligned} G_m(t + \Delta t) &= (1 - \epsilon_t)G_m(t) + \epsilon_t G(t + \Delta t) \\ h_m(t + \Delta t) &= (1 - \epsilon_h)h_m(t) + \epsilon_h h(t + \Delta t - t_{\text{onset}}), \end{aligned} \quad (2.9)$$

where  $\epsilon_t$  and  $\epsilon_h$  denote the turbulence and thermal delay factors, respectively, and  $t_{\text{onset}}$  marks the time at which  $h$  begins to evolve. We adopt the empirical values  $\epsilon_t = 4 \times 10^{-3}$ ,  $\epsilon_h = 1.4 \times 10^{-3}$ , and  $t_{\text{onset}} = 3200$  s, with a time-stepping interval of  $\Delta t = 5$  s. The modeled curves in Figure 2.5 reproduce the evolution of  $u_*$  and  $h$  observed in the LES. Because the equilibrium values before ( $t = 0$ ) and after acceleration ( $t = 5$  min) are determined from the geostrophic drag law for conventionally neutral boundary layers, the fit constrains only the timescale over which the profiles relax toward equilibrium. For  $u_*$ , this timescale is  $\tau_t = H/u_* \approx 0.7$  h, which also corresponds to the delay before the boundary-layer height begins to increase.

The corresponding model predictions for velocity profiles, including dynamic effects, are shown in Figure 2.4. Overall, the model reproduces the acceleration trends well and captures the interaction between the geostrophic flow and the ABL, demonstrating that the turbulence closure represents the essential boundary-layer dynamics. After  $t = 6$  h, the model slightly overpredicts the spanwise velocity  $V$  near the top of the ABL, due to an overestimate of  $h$ , as shown by the LES results in Figure 2.5b.

### 2.4.3 Towards natural wind speed variations

The linear wind-speed cases discussed above illustrate the processes by which ABL flow transitions between equilibrium states, which the reduced-order model captures well. However, under realistic conditions the geostrophic wind varies continuously, and the ABL rarely recovers to equilibrium. To access the realistic scenarios, we consider a dynamic wind speed signal adapted from field measurements.

The demonstrative wind speed variations are measured at the National Wind Technology Center (NWTC) [50] in Colorado, USA. On January 28, 2018, six hours of wind speed data (4:30 -10:30 a.m.) were collected at a height of  $h = 87$  m using the M5 meteorological mast. The low-frequency wind speed variations in mesoscale range are obtained by applying a low-pass filter with

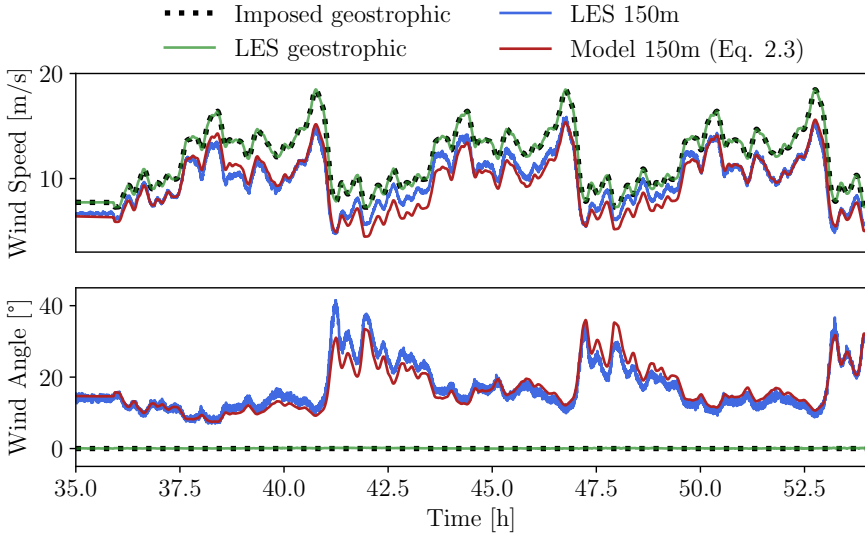


Figure 2.6: Time series of wind speed and direction in the geostrophic layer ( $z = 1500$  m) and in the lower ABL ( $z = 150$  m).

cut-off frequency  $f = 6 \times 10^{-4}$  Hz, which are imposed as the geostrophic wind speed signal (repeated 3 times) in LES through Eq. 2.2. It is worth noting that the wind speed measured near the surface is not fully representative for variations in geostrophic wind speed. However, for demonstrative purposes, it assesses the ability of the model to capture dynamically varying wind speed signals.

Figure 2.6 shows that the proposed forcing method in Eq. 2.2 accurately reproduces the imposed geostrophic wind speed while keeping the geostrophic wind direction constant. At  $h = 150$  m, the wind speed generally follows the geostrophic trend. However, closer inspection reveals that the ratio between the geostrophic wind speed and the wind speed at 150 m is not constant but varies in response to the imposed forcing. At the same time, significant variations in wind direction emerge, highlighting the complex dynamics of the ABL.

To evaluate the model under these conditions, we compare its predictions with LES results (Figure 2.6), using the same time-varying geostrophic forcing  $G(t)$  and the turbulence parameterization defined in Eq. 2.7. The comparison at  $z = 150$  m, representative of wind-turbine hub height, shows that although the model exhibits small deviations from LES during periods of rapid wind

speed changes (near  $t = 41.5$  h), it captures the essential features of the flow with good accuracy. So, despite its simple turbulence closure, the reduced-order model offers an efficient and reliable alternative to LES for capturing unsteady ABL behavior.

## 2.5 Conclusions

We investigated the dynamics of wind speed changes in the ABL under time-varying geostrophic forcing. Variations in geostrophic wind, derived from mesoscale simulations or field measurements, were accurately reproduced in LES by applying a dynamic pressure-gradient force. Building on the damped-oscillator framework of Momen and Bou-Zeid [56–58], we extended the model to incorporate geostrophic forcing, Coriolis effects, and turbulence. The resulting reduced-order model captures the interaction between the ABL and the geostrophic layer, and validation against LES of conventionally neutral boundary layers confirms its ability to reproduce the essential dynamics. This framework enhances the understanding of dynamic wind conditions and provides a practical tool for wind energy applications. Although validated here for conventionally neutral boundary layers, the approach can be extended to other ABL regimes or the diurnal cycle, offering a computational modeling approach toward more realistic atmospheric dynamics in wind farm simulations.

## Appendix

### 2.A LES framework

We perform LES of conventionally neutral ABLs driven by geostrophic wind. The ABL is assumed neutral, while buoyancy effects above the ABL are represented using the Boussinesq approximation. The governing equations are:

$$\partial_i \tilde{u}_i = 0, \quad (2.10a)$$

$$\partial_t \tilde{u}_i + \partial_j (\tilde{u}_i \tilde{u}_j) = -\partial_i \tilde{p}^* - \partial_j \tau_{ij} - \epsilon_{ijk} f_C \tilde{u}_k + \partial_i p + g\beta(\tilde{\theta}) \delta_{i3}, \quad (2.10b)$$

$$\partial_t \tilde{\theta} + \tilde{u}_j \partial_j \tilde{\theta} = -\partial_j q_j. \quad (2.10c)$$

The tilde denotes spatial filtering at the LES grid scale  $\Delta$ , and  $\tilde{u}_i$  and  $\tilde{\theta}$  represent the filtered velocity and potential temperature components. The traceless part of the subgrid-scale (SGS) stress tensor,  $\tau_{ij} = \tilde{u}_i \tilde{u}_j - \tilde{u}_i \tilde{u}_j$ , together with the SGS potential-temperature flux  $q_j$ , is modeled using the anisotropic minimum dissipation model. Here  $\tilde{p}^*$  is the kinematic pressure,  $g$  the gravitational acceleration,  $f_C$  the Coriolis frequency, and  $\epsilon_{ijk}$  the alternating unit tensor. The buoyancy parameter is  $\beta = 1/\theta_0$ , where  $\theta_0 = 286\text{K}$  is the reference potential temperature. Due to the high Reynolds numbers in the atmosphere, viscous stresses are typically neglected. The pressure-gradient forcing  $\partial_i p$  drives the flow following the formulation in Eq. 2.2. Note that the symbol  $\theta(t)$  in the main text refers to the geostrophic wind angle, distinct from  $\theta$  and  $\theta_0$  used here for potential temperature.

The computational domain is bounded at the top by zero vertical velocity, zero shear stress, and a constant potential-temperature gradient. At the same time, periodic boundary conditions are imposed in the streamwise and spanwise directions. At the surface, wall shear stress is modeled using the Monin–Obukhov similarity theory, and a zero potential temperature flux is applied. The pseudo-spectral method is used in the streamwise and spanwise directions, while second-order finite differences are employed in the vertical. Time integration is performed with a third-order Adams-Bashforth scheme. Further details can be found in [17, 46].

# 3

## Turbulence coherence in wind farms: The role of turbines <sup>o</sup>

Models for wind farm power fluctuations primarily focus on the impact of atmospheric turbulence. We employ large eddy simulations (LES) to demonstrate that dynamic changes in thrust ( $C_T$ ) and power ( $C_P$ ) coefficient affect the coherence of power fluctuations in turbine pairs. We consider various inflow wind speeds to examine the velocity and power coherence between consecutive turbine rows under three scenarios: (I) a fully developed region where all turbines operate below rated power, (II) the front row operates above rated power while the downstream row operates below rated power, and (III) both rows operate above rated power. In scenario I, the random sweeping hypothesis turbulence model by Tobin and Chamorro, JFM 855, 1116-1129 (2018) can effectively predict the coherence between the turbines. However, in scenarios II and III, the model fails to capture the simulation results. This discrepancy arises due to the operation of above-rated turbines, with dynamically varying  $C_T$  and  $C_P$ , which have a distinctly different effect on the flow than turbines operating with fixed  $C_T$  and  $C_P$ .

---

<sup>o</sup>Published as: Y. Liu, and R.J.A.M. Stevens, *Turbulence coherence in wind farms: The role of turbines*. In *Journal of Physics: Conference Series* **2767** 092108



### 3.1 Introduction

Wind power has inherent variability across a wide range of scales due to atmospheric turbulence. To reduce the impact of wind farm load perturbations on the power grid, it is necessary to understand the power fluctuations of extended wind farms. For individual wind turbines, it is well understood that the power output spectrum follows a  $f^{-5/3}$  power law [1, 2], which originates from the  $k^{-5/3}$  scaling of Kolmogorov turbulence [66]. The power fluctuations of different wind farms are typically less correlated with each other due to the geographic smoothing effects. Consequently, the aggregate power spectrum of geographically widely distributed wind farms adheres to a  $f^{-7/3}$  distribution [3].

Wind turbines in wind farms are typically spaced less than ten rotor diameters apart, causing downstream turbines to operate within the wakes of upstream turbines. As a result, the influence of these wakes on power fluctuations cannot be overlooked. When the inter-turbine spacing is relatively small the correlation between the output of various turbines is strongly impacted by atmospheric boundary layer (ABL) turbulence, while the effect of geographical smoothing is limited. Simulations show that the aggregate power spectrum of wind farms exhibits a  $f^{-5/3}$  scaling [40]. Furthermore, the spectrum may exhibit peaks attributable to constructive interference, a phenomenon observed in wind tunnel experiments [67]. Bossuyt *et al.* [68] assumed that turbines can be considered as local samplers of the velocity field. They used the random sweeping hypothesis proposed by Kraichnan [69] and Tennekes [70] to model power fluctuations within wind farms. They argued that the aggregate wind farm power spectrum is influenced by both the incoming turbulence and the spatial arrangement of the wind turbines. Liu *et al.* [71] and Tobin and Chamorro [72, 73] studied the correlation between turbine rows and investigated the coherence spectrum of two consecutive turbine rows within wind farms. This work will compare the coherence model they introduced against various large eddy simulations (LES) scenarios.

Studies on wind farm power fluctuations often assume a fixed operational point with constant thrust ( $C_T$ ) and power ( $C_P$ ) coefficients. However, modern wind turbines typically operate in two distinct regions, determined by whether they are below or above the rated wind speed. Below the rated wind speed, the primary objective is to maximize the power efficiency of the turbines. Above the rated wind speed, the main goal is to maintain the rated power output.

Achieving these objectives necessitates continuous adjustments of  $C_T$  and  $C_P$  to the wind speed.

This work investigates power fluctuations within extended wind farms using LES. We analyze the velocity and power coherence of turbine pairs with the model proposed by Tobin and Chamorro [72]. Specifically, we examine the effects of dynamic variations in the thrust and power coefficient instead of assuming fixed operating conditions. Section 3.2 introduces the theoretical framework for predicting coherence between turbine productions using the random sweeping hypothesis model. Section 3.3 describes our LES methodology for simulating wind farm flows. The analysis of power fluctuations and coherence among turbine pairs is presented in Section 3.4, and the paper concludes with a summary of our findings in Section 3.5.

# 3

## 3.2 Theoretical framework

### 3.2.1 Definition of coherence spectrum

The coherence spectrum of two equal-length signals,  $X$  and  $Y$ , is defined as

$$C_{XY}(\omega) = \frac{\Phi_{XY}(\omega)}{\sqrt{\Phi_X(\omega)\Phi_Y(\omega)}} \quad (3.1)$$

where  $\Phi_{XY}(\omega)$  is the cross spectrum of  $X$  and  $Y$ , and  $\Phi_X(\omega)$  and  $\Phi_Y(\omega)$  are the power spectra of each signal.

### 3.2.2 Random sweeping hypothesis

To apply the random sweeping hypothesis in modeling wind turbine power fluctuations, it is assumed that the turbines act as passive probes of the ABL turbulence. We follow the steps provided by Tobin and Chamorro [72] to introduce the basic ideas. Considering the observation that the time scale of atmospheric turbulence evolution significantly exceeds the time it takes for the flow to pass through wind turbines, the random sweeping hypothesis assumes that the turbulent velocity  $u$  remains temporally frozen but is spatially

adverted by a sweeping velocity  $v$ . The spatial-temporal relation is modeled as follows:

$$\frac{\partial u}{\partial t} + v \frac{\partial u}{\partial x} = 0 \quad (3.2)$$

For simplicity, we only consider the streamwise component of  $u$ , denoted by  $u_1$ . By Fourier transform with respect to time  $t$ , where  $u_1(x, t) = \sum_{n=1}^{\infty} \hat{u}_1(x) \exp(i\omega t)$ , the spatial-temporal relation can be expressed in frequency space as:

$$\frac{\partial \hat{u}_1}{\partial x} = -\frac{i\omega}{v} \hat{u}_1 \quad (3.3)$$

Further, we split the sweeping velocity into  $v = V + v'$ , where  $V$  is the mean value of sweeping velocity while  $v'$  represents the relative fluctuations. We consider two spatially fixed points, aligned in the streamwise direction and separated by a distance  $\Delta x$ , representing the locations of two wind turbines. The cross spectrum of this turbine pair can be expressed as

$$\Phi_{XY}(\omega) = \langle \hat{u}(\Delta x, \omega) \hat{u}(0, -\omega) \rangle = \langle \hat{u}(0, \omega) \hat{u}(0, -\omega) \rangle \left\langle \exp\left(\frac{-i\omega\Delta x}{V + v'}\right) \right\rangle \quad (3.4)$$

by assuming that the spectra at the same height remain statistically identical everywhere.

By additionally assuming that  $v'$  follows a Gaussian distribution with zero mean and a standard deviation of  $\sigma_v$ , the two-point coherence spectrum can be expressed through integration over all possible values of  $v'$ :

$$C(\omega) = \int_{-\infty}^{\infty} \exp\left(\frac{-i\omega\Delta x}{V + v'}\right) f(v') dv' \quad (3.5)$$

where the probability density function of  $v'$  is

$$f(v') = \frac{1}{\sigma_v \sqrt{2\pi}} \exp\left(-\frac{1}{2}(v'/\sigma_v)^2\right) \quad (3.6)$$

The exponential part in Eq. 3.4 can be approximated using the Taylor series:

$$-\frac{i\omega\Delta x}{V + v'} = -\frac{i\omega\Delta x}{V} \sum_{n=0}^{\infty} (-v'/V)^n \quad (3.7)$$

By substituting Eq. 3.7 in Eq. 3.5, we get the expression for the coherence spectrum

$$C(\omega) = \frac{1}{\sigma_v \sqrt{2\pi}} \int_{-\infty}^{\infty} \prod_{n=0}^{\infty} \exp\left(-\frac{i\omega\Delta x}{V} \cdot (v'/V)^n\right) \exp\left(-\frac{1}{2}(v'/\sigma_v)^2\right) dv' \quad (3.8)$$

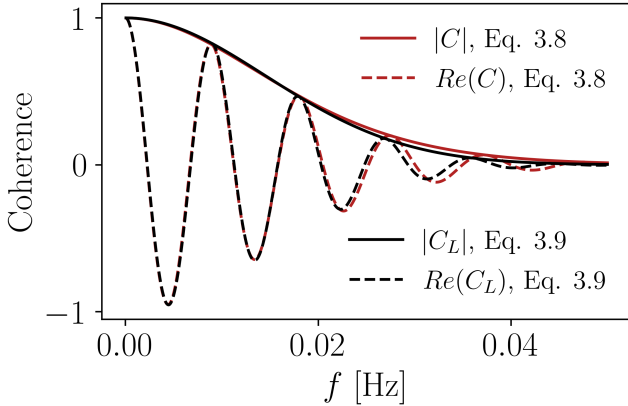


Figure 3.2.1: The nonlinear (Eq. 3.8) and linear (Eq. 3.9) model proposed by Tobin and Chamorro [72]). The absolute values and real parts of the coherence are presented for  $\sigma_v = 1.2$  with sweeping velocity  $V = 12.14$  m/s and spacing  $\Delta x = 1346$  m.

Tobin and Chamorro [72] examined the stationary inflow case, where the velocity fluctuations  $v'$  are relatively small compared to  $V$ . They focused on the linear terms in Eq. 3.8 (up to  $n = 1$ ) and derived the following analytical expression

$$C_L(\omega) = \underbrace{\exp\left(-\frac{i\omega\Delta x}{V}\right)}_{\text{I}} \underbrace{\exp\left(-\frac{\omega^2\Delta x^2\sigma_v^2}{2V^4}\right)}_{\text{II}} \quad (3.9)$$

Here, the first term represents the advection of turbulence, while the second term accounts for turbulence decoherence. As depicted in Eq. 3.8, the precision of Eq. 3.9 is primarily influenced by the ratio  $v'/V$ , which depends on the standard deviation  $\sigma_v$ . In Figure 3.2.1, we compare the linear (Eq. 3.9) and nonlinear (Eq. 3.8) coherence models with respect to  $f = \omega/2\pi$ , where a stationary ABL with hub-height turbulence intensity of about 10% is considered. We observe that the linear scheme is sufficiently accurate, and differences are primarily observed in the decoherence region.

### 3.3 Large eddy simulations

The simulations are performed using an updated version of the LES code developed by Albertson and Parlange [74], which is validated by Gadde *et al.* [46]. We consider a simplified case with neutral pressure-driven ABL. The LES equations read:

$$\partial_i \tilde{u}_i = 0 \quad (3.10a)$$

$$\partial_t \tilde{u}_i + \partial_j (\tilde{u}_i \tilde{u}_j) = -\partial_i \tilde{p}^* - \partial_j \tau_{ij} - \frac{\partial_i p_\infty}{\rho} + f_i \quad (3.10b)$$

where the tilde represents the spatial filtering at LES grid scale  $\Delta$ . The driving pressure gradient is  $\partial_i p_\infty / \rho = -u_*^2 / H$ , where  $u_*$  is the friction velocity.  $\tau_{ij} = \tilde{u}_i \tilde{u}_j - \tilde{u}_i \tilde{u}_j$  is the traceless part of sub-grid scale (SGS) tensor modeled by anisotropic minimum dissipation (AMD) model. The viscous stress is neglected due to the high Reynolds number in wind farm simulations. The filtered modified pressure is  $\tilde{p}^* = \tilde{p} - p_\infty / \rho - \tau_{kk} / 3$ , and  $f_i$  represents the turbine forces.

The flow is bounded with zero vertical velocity and zero shear stress on top of the domain, and periodic condition is applied in streamwise and spanwise boundaries. The Monin-Obukhov similarity theory models the wall shear stress with a roughness height  $z_0 = 0.1m$ . Variables in streamwise and spanwise directions are calculated using the pseudo-spectral method, while a second-order finite difference scheme is used in the vertical direction. Time-integration is performed with a third-order Adams-Bashforth scheme. We employ the concurrent precursor simulation [40] to generate realistic inflow for wind farms. In this approach, an additional precursor simulation of ABL runs simultaneously alongside the wind farm domain, and the flow field is copied into the fringe region of the wind farm domain.

### 3.4 Turbine coherence within an extended wind farm

#### 3.4.1 Case overview

We performed wind farm simulations in a pressure-driven neutral ABL. The domain size for both the precursor and the wind farm domain is  $4\pi \times 2\pi \times$

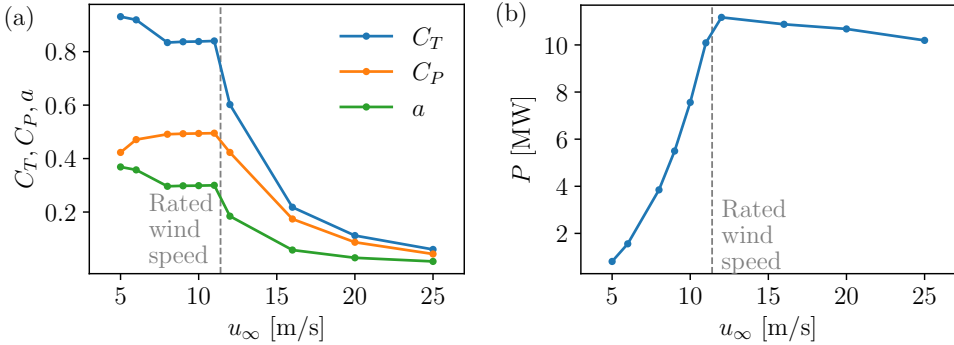


Figure 3.3.1: (a)  $C_T$ ,  $C_P$  and  $a$  values and (b) mechanical power of DTU 10MW turbine as function of wind speed, adapted from Bak *et al.* [51].

1km, spanning the streamwise, spanwise, and vertical directions, respectively. The grid employs spacings of  $\Delta x = \Delta y = 25.54\text{m}$  and  $\Delta z = 7.81\text{m}$ . The wind farm consists of 7 rows and 4 columns of DTU 10MW wind turbines. These turbines are modeled using the actuator disk approach, with  $C_T$  and  $C_P$  coefficients provided in Figure 3.3.1a. The turbines are positioned in a grid layout, featuring a streamwise spacing of  $S_x = 7D$  and a spanwise spacing of  $S_y = 5D$ .

It is worth noting that  $C_T$  and  $C_P$  are defined by undisturbed inflow wind speed  $u_\infty$ , while identifying  $u_\infty$  for downstream turbines remains challenging as they operate in the wakes of the upstream turbines. In the simulations, we employ thrust and power coefficients as functions of disk velocity  $u_d$ , denoted by  $C'_T$  and  $C'_P$ . Therefore, turbine thrust is determined by  $F = 1/2\rho A C'_T u_d^2$ , where  $\rho$  is the density of air and  $A$  the sweeping area of rotor. The resulted turbine power is calculated as  $P = 1/2\rho A C'_P u_d^3$ .

For stronger winds, the average wind speed at the leading row can be high enough to ensure the first row is operating above-rated power, while downstream turbines operate below their rated power due to the wakes from upstream turbines. To simulate various operational conditions for the wind farm, we consider different incoming hub-height velocities, i.e.  $U_{\text{hub}} = [12.14, 13.5, 15] \text{ m/s}$ . In Figure 3.4.1, where the average velocities through the rotor disk are displayed, we identify three typical combinations of operational statuses between consecutive turbine rows: namely, both turbines operate below rated power (scenario 1), one turbine is operating above rated power and the downstream one below rated power (scenario 2), and both turbines operate above-rated

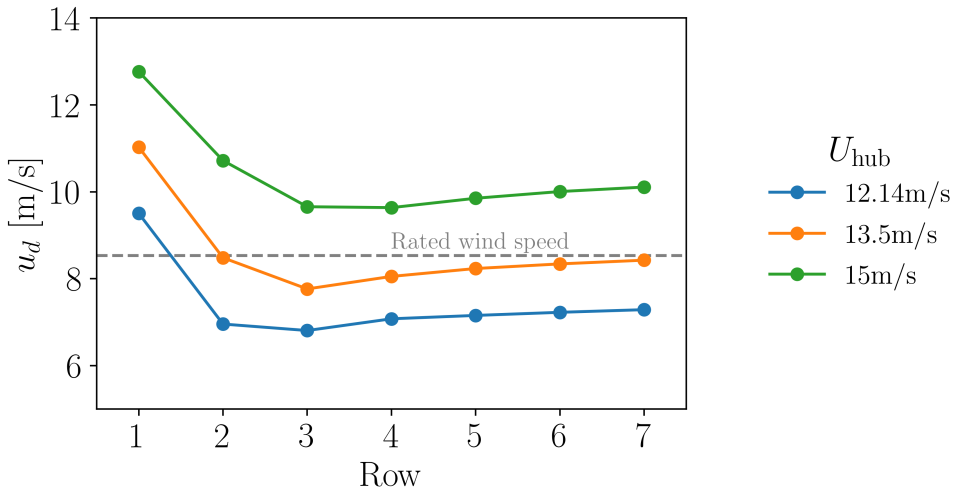


Figure 3.4.1: Average wind velocity through the rotor disk as a function of downstream turbine row for the three simulations with different inflow velocities  $U_{\text{hub}}$ .

3

power (scenario 3). Notably, only turbines operating in fully developed wakes are considered in scenario 1, from which turbines behind above-rated wakes (usually the first below-rated row) are excluded.

Each case is simulated for 100 hours, where we use the first 15 hours as the initialization period. The last 85 hours of power and velocity signals collected from the turbines are divided into 104 equal-length sections for spectral analysis, followed by the computation of their average. This results in a lowest observable frequency  $\sim 3 \times 10^{-4} \text{ Hz}$  in the analysis. Finally, the coherence between consecutive rows is established by averaging the results across the four turbine columns. It is crucial to acknowledge that opting for longer segments improves precision in the low-frequency range, while it increases noise at higher frequencies. Increasing the segment count helps to mitigate noise in the high-frequency domain. However, this limits the accuracy at low frequencies and the lowest observable frequency. Our selection of 104 segments is a compromise that aims to effectively smooth out high-frequency noise while preserving sufficient resolution in the low-frequency range.

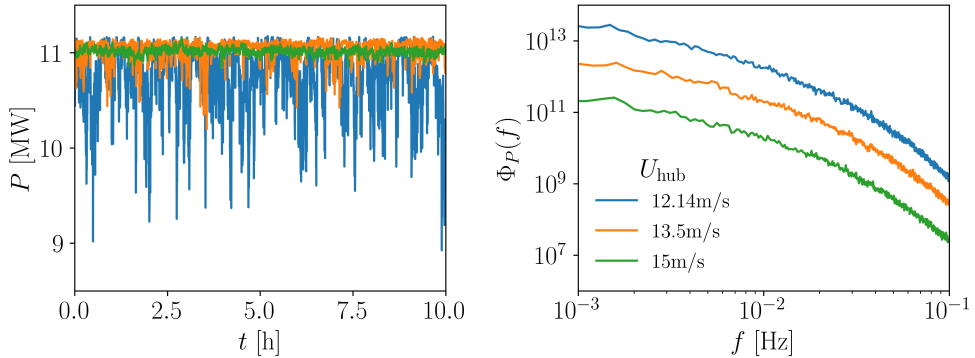


Figure 3.4.2: Power fluctuations of a turbine in the first row under different inflow wind speeds. Left: time series; right: power spectrum.

### 3.4.2 Power fluctuations of above-rated wind turbines

The power production of turbines operating below their rated capacity is governed by the wind speed passing through the rotor-swept area and approximately follows the cubic relationship  $P \propto (u_d)^3$ . This relationship arises from deploying turbine control strategies that try to sustain stable  $C_T$  and  $C_P$  values over a wide range of wind speeds. For instance, the DTU 10MW turbine is designed to maintain consistent values of approximately  $C_T \approx 0.8$  and  $C_P \approx 0.5$  until it reaches its rated wind speed  $u_{\text{rated}} = 11.4 \text{ m/s}$ .

Above the rated speed, the control strategy of the wind turbine is designed to maintain the rated power, leading to a reduction in power fluctuations. Figure 3.4.2 shows that the power fluctuations of first-row wind turbines decrease with increasing wind speed. It's important to highlight that the maximum power output,  $P_{max} \approx 11 \text{ MW}$  (refer to the left side of Figure 3.4.2), is a consequence of the  $C_P$  values provided by Bak *et al.* [51]. Specifically, we employ the EllipSys DTU 10MW power curve, illustrated in Figure 3.3.1b, which shows a slight decrease in power production as wind speeds exceed the rated wind speed.

### 3.4.3 Coherence of turbine pairs in the fully developed region (scenario 1)

In Figure 3.4.3 (left), the coherence spectra between rows 4 and 5 are presented for  $U_{\text{hub}} = 12.14 \text{ m/s}$ . Both these turbine rows operate in the wake of upstream turbines and, therefore, correspond to scenario 1. The velocity and power coherence observed in the LES agree excellently with the model predictions by Tobin and Chamorro [72]. The absolute coherence demonstrates a consistent decay from low to high frequencies, attributable to the random fluctuations of the sweeping velocity. Moreover, the phase angle exhibits periodic variations, reflecting a frequency-dependent phase difference between the signals recorded by the two turbines. These findings show that in the fully developed region of the wind farm, the power coherence between consecutive turbine rows is well described by a random sweeping model for atmospheric turbulence. However, it's important to recognize that wake turbulence contributes to the variability of the sweeping velocity, an aspect incorporated into the  $\sigma_v$  parameter of the random sweeping model.

In the random sweeping model the absolute coherence to approach unity at  $f = 0$ . However, this condition is not perfectly reflected in the simulations, where the coherence is observed to be lower. Consequently, a constant factor  $0 < C_0 < 1$  is introduced, scaling the coherence to align with the simulation data. This factor  $c$  is believed to be linked to the induction factor  $a$  of the wind turbines. For turbines operating below their rated capacity, and with a constant induction factor  $a$ , the velocity deficit relates linearly to the inflow wind speed, denoted as  $u_\infty - u_d = a \cdot u_\infty$ . The linearity of the Fourier transform  $\mathcal{F}(a \cdot u_\infty) = a \cdot \mathcal{F}(u_\infty)$  implies that after passing the wind turbine, the amplitude of velocity deficit across all scales can be described by multiplying with the induction factor  $a$ . However, the fitted constant  $C_0$  cannot be simply equated to  $1 - a$  (which equals 0.7 for DTU 10MW turbines). The reason is that the wake turbulence still undergoes modification through turbulence entrainment before reaching the downstream row, which further depends on the atmospheric conditions and turbine spacing.

### 3.4.4 Coherence of above-below-rated turbine pairs (scenario 2)

In scenario 2, exemplified by the coherence between rows 1 and 2 (see Figure 3.4.3 right), the behavior is pronounced differently than in scenario 1. Firstly,

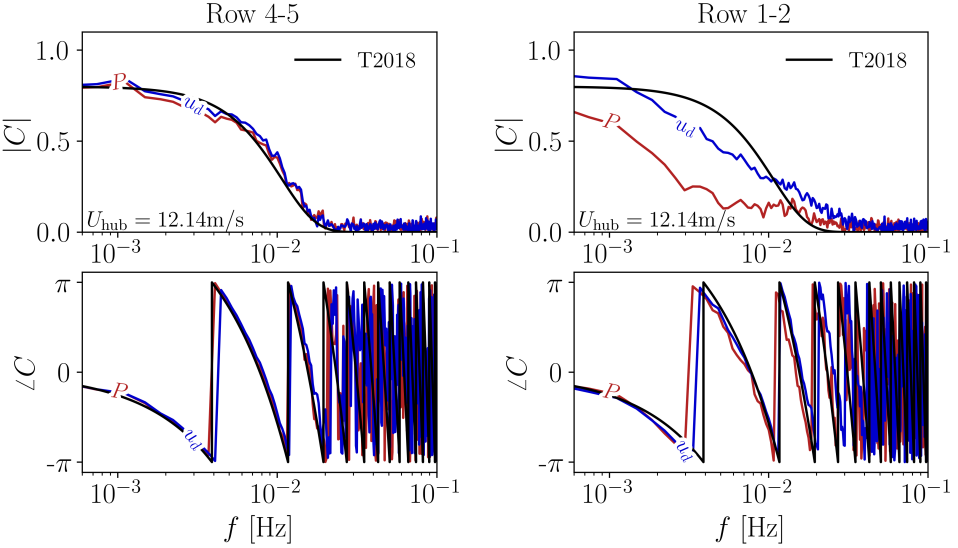


Figure 3.4.3: Comparison of two-row coherence from LES ( $U_{\text{hub}} = 12.14\text{m/s}$ ) with predictions of Tobin and Chamorro [72] (T2018). Left: below-below-rated pairs (scenario 1), right: above-below-rated pairs (scenario 2). Top: absolute coherence, bottom: phase angle.

the velocity coherence deviates from the predictions of the random sweeping model, exhibiting higher values than predicted at both large and small frequencies yet lower at intermediate frequencies. The reason is that the  $C_T$  (equivalently, the induction factor  $a$ ) for the above-rated turbines dynamically responds to variations in incoming wind speed. At higher wind speeds, the induction factor  $a$  decreases significantly; see Figure 3.3.1. This variation in  $a$  leads to a relative velocity deficit that depends on the incoming wind velocity, which impacts the performance of the downstream turbine in the pair. As a result, the velocity coherence in this scenario cannot be accurately represented by simply applying a uniform multiplicative constant to the coherence predicted by the random sweeping model across all frequencies.

Secondly, the power output exhibits less coherence than velocity. This phenomenon is primarily attributed to the fact that the upstream turbine in the pair operates above-rated. As elaborated in Section 3.4.2, power output from turbines operating above their rated capacity exhibits reduced sensitivity to incoming flow compared to turbines operating below-rated power. This reduces the correlation between velocity and power output. Despite the deviations in

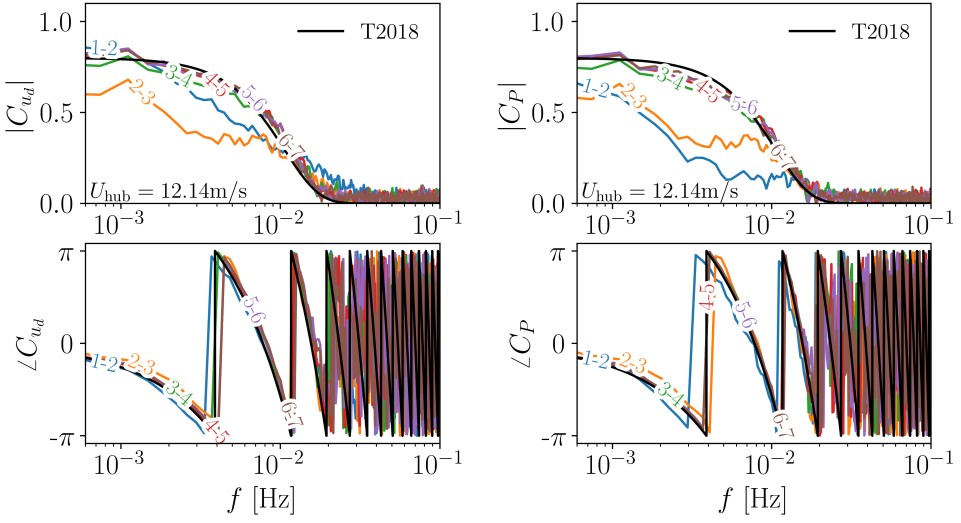


Figure 3.4.4: Comparison of two-row coherence in wind farm from LES ( $U_{\text{hub}} = 12.14\text{m/s}$ ) with predictions of Tobin and Chamorro [72]. Left: velocity coherence, right: power coherence.

absolute coherence, the phase angle remains well-predicted by the theoretical framework. In the random sweeping model (Eq. 3.9), the phase diagram solely depends on the sweeping velocity  $V$  and turbine spacing  $\Delta x$ . As the sweeping velocity only differs slightly from scenario 1, the main trends are still well predicted despite slight differences that can be observed.

### 3.4.5 Coherence within the wind farm

In Figure 3.4.4, the coherence spectra of all consecutive rows within the wind farm for  $U_{\text{hub}} = 12.14\text{m/s}$  are presented. Starting at row 3–4, both the power and velocity coherence converge to the random sweeping model predictions. This implies that the wind farm transitions into the fully developed region where scenario 1 applies around the third row. Apart from the deviation of row 1–2 which is elaborated in Section 3.4.4, a significant lower coherence is observed for rows 2–3. In Figure 3.4.5, we exemplify the time series of  $a$  in first three rows. As the operation of downstream rows (row 2 and 3) are insensitive to the incoming turbulence with stable induction factor, the above-rated first

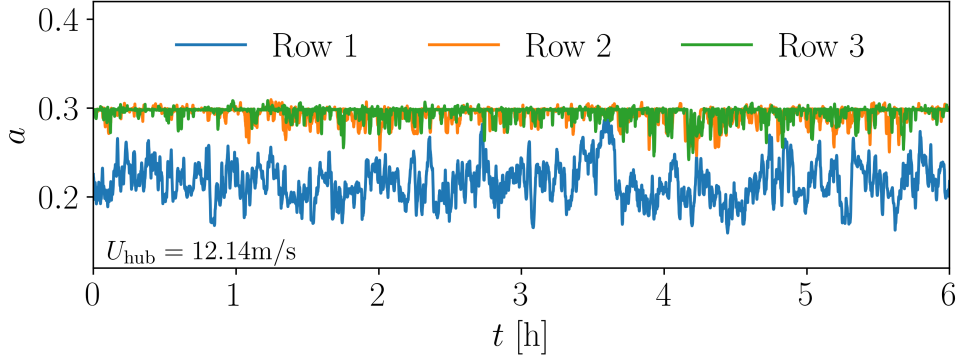


Figure 3.4.5: Temporal variation of the induction factor  $a$  in first three rows for  $U_{\text{hub}} = 12.14 \text{ m/s}$ .

row exhibits lower but more fluctuating induction factor responding to the incoming turbulence. The wake turbulence impacting the second row originates from turbines operating above the rated capacity with a varying induction factor  $a$ , which has a remarkably different wake structure than below-rated wakes impacting the third row. Therefore, turbine pairs impacted by the above-rated operation, including those containing above-rated turbines (row 1) or turbines in above-rated wakes (row 2), do not follow the random sweeping predictions.

To verify the hypothesis that the observed behavior is due to turbines operating above and below their rated capacity, we present simulations with all turbines operating at  $C_T = 0.8$  and  $C_P = 0.5$  in Figure 3.4.6. As row 1 becomes the first below-rated row, the fully developed region where scenario 1 applies starts from row 2. This is evidenced by an improved agreement of rows 2 – 3 coherence with model predictions, and the coherence of rows 1 – 2 resembles rows 2 – 3 in dynamic  $C_T$  case. This highlights that the turbine operation has a pronounced influence on velocity and power coherence within a wind farm, even though previous works focused on the role atmospheric turbulence alone [68, 72].

As the inflow wind speed increases, a growing number of turbines within a wind farm operate above-rated, as illustrated in Figure 3.4.1. In Figure 3.4.7, we provide the velocity coherence spectra for higher wind speeds. For  $U_{\text{hub}} = 13.5 \text{ m/s}$ , the coherence of rows 2 – 3 is notably lower than for other rows. The reduced coherence originates from the difference in turbine operating conditions in rows 2 and 3. For the case with  $U_{\text{hub}} = 15 \text{ m/s}$ , this effect is

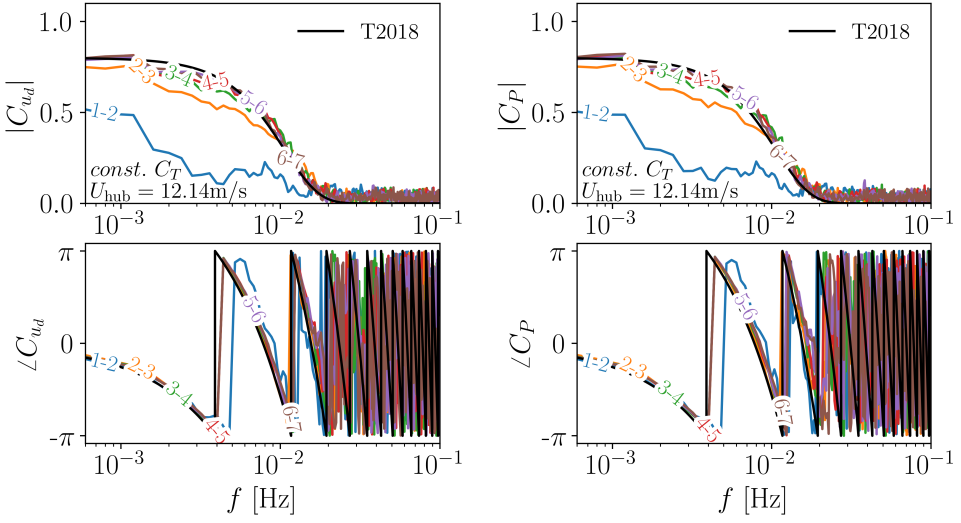


Figure 3.4.6: Coherence spectra for the simulation ( $U = 12.14\text{m/s}$ ) with constant  $C_T = 0.8$  and  $C_P = 0.5$ .

3

somewhat visible for rows 2 – 3 and 3 – 4. For this case, the third row has a distinctive response as its average wind speed is closest to the rated wind speed, indicating that it operates more frequently in below-rated regime than other rows. As a typical example for scenario 3, row 1 – 2 in the  $U_{\text{hub}} = 15\text{m/s}$  case exhibits a significantly higher coherence. As both rows operate far above-rated wind speed and their influence on the incoming flow is relatively weak, the coherence pattern is much closer to the original random sweeping model predictions with  $C_0 = 1$ .

Figure 3.4.8 shows the power coherence at higher inflow wind speeds. As the wind speed increases, there's a notable decorrelation in power production across all turbine pairs, a trend that increases with increasing wind speed. This trend further substantiates the notion that power fluctuations in turbines operating above their rated capacity are less influenced by incoming turbulence and more by the control strategy of the turbines, characterized by dynamic adjustments in  $C_T$  and  $C_P$ . Given these dynamics, the spectral characteristics of power coherence in such scenarios are not accurately captured by the random sweeping model for atmospheric turbulence.

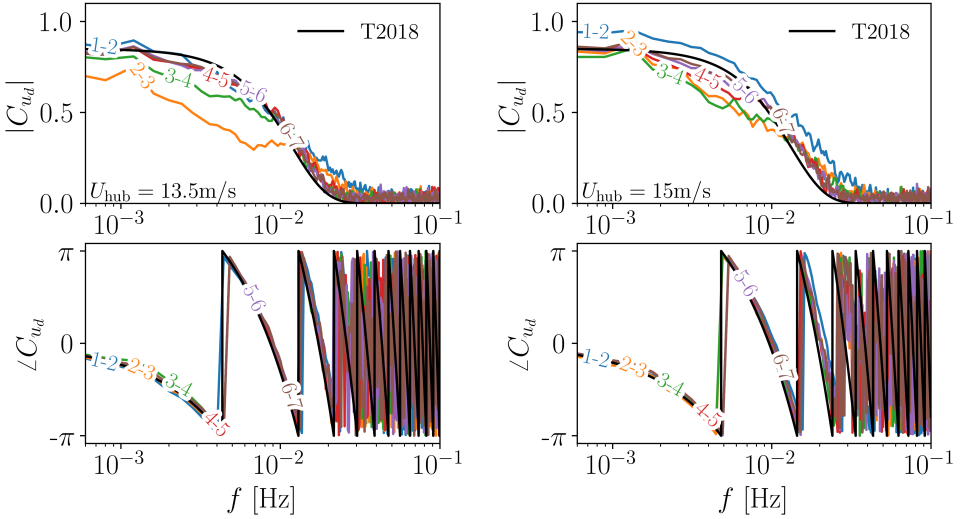


Figure 3.4.7: Velocity coherence between consecutive turbine rows in wind farm for inflow wind speed  $U_{\text{hub}} = 13.5$  and  $15\text{m/s}$ .

### 3.5 Conclusions

We investigate the coherence between consecutive downstream turbine rows in extended wind farms using LES. Our findings demonstrate that the random sweeping hypothesis, as outlined in the theoretical framework [72], accurately captures the power and velocity coherence for turbine pairs operating below-rated power in the fully developed region. The coherence between consecutive turbine rows deviates from the random sweeping predictions when the leading turbine operates above its rated power or in the wakes of above-rated turbines, while the downstream row operates below rated power. Additionally, the correlation between power and velocity fluctuations diminishes when the average wind speed surpasses the rated power of the turbines.

These findings show that dynamic variations in thrust and power coefficient have a significant impact on the velocity and power coherence among consecutive downstream turbine rows. With the growing size of wind turbines, their interaction with the ABL turbulence becomes more pronounced, which alters the turbulence structure both in front of (induction zone) and behind (wake region) the turbines [4, 75], and this is an aspect not accounted for in the

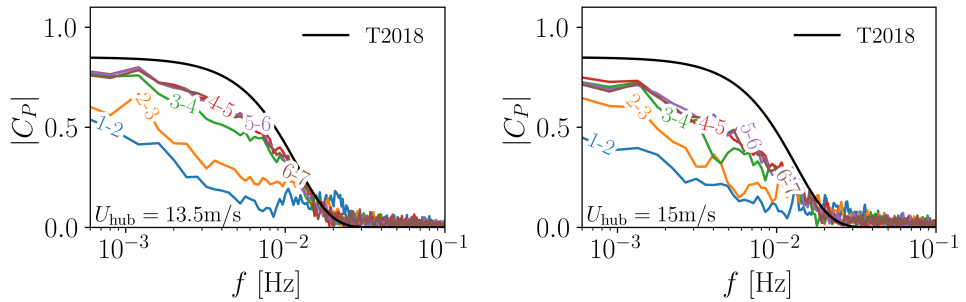


Figure 3.4.8: Absolute coherence of power production for consecutive turbine rows in a wind farm for  $U_{\text{hub}} = 13.5 \text{ m/s}$  and  $15 \text{ m/s}$ .

random sweeping model [72]. Beyond the neutral ABL case illustrated in this work, there are multiple factors impacting the turbulence coherence in wind farms, such as the turbulence level of incoming flow [72] and the thermal stability [73]. Consequently, a comprehensive understanding of the corresponding dynamics requires further investigation.



# 4

## Wake-corrected random sweeping model for wind farm power coherence<sup>◦</sup>

Random sweeping models predict coherence in atmospheric flows well and can provide valuable insights into power output correlations between wind turbines. However, these models typically overpredict coherence because they neglect wind turbine wake effects. We use large-eddy simulations (LES) to quantify these effects within a wind farm and identify two distinct regimes: the entrance region and the downstream wind farm region. In the entrance region, coherence between turbines in the leading rows drops significantly due to the transition from atmospheric boundary layer flow to internal wind farm flow, driven by the formation of an internal boundary layer. In the downstream region, traditional random sweeping models capture the trend but overpredict coherence. Our new theoretical framework incorporates coherence reduction due to wind turbine wakes and achieves excellent agreement with LES results across a range of induction factors and turbine spacings. These results extend the applicability of random sweeping theory to operational wind farms and provide a physics-based tool for predicting power correlations for different turbine layouts and operating conditions.

---

<sup>◦</sup>To be submitted as: Y. Liu and R.J.A.M. Stevens, *Wake-corrected random sweeping model for wind farm power coherence*.



## 4.1 Introduction

Understanding fluctuations in wind power output is crucial for the reliable operation of the power grid. For a single turbine, power generation is governed by the local wind speed at the rotor. Studies show that the wind turbine power fluctuations show same turbulent character as that observed in winds [1, 2]. On wind farm scale, variability in total power output depends not only on output of individual turbines, but also the correlation of power fluctuations in the farm. The advection of turbulent eddies through the farm introduces a time-delayed response in power output of downstream turbines compared to their upstream counterparts [76, 77]. This phenomenon depends on the wind speed conditions, wind farm layout and turbine spacings, which is captured by power coherence function of turbine pairs [7–9]. The coherence function is essential for translating the spectral characteristics of individual turbines into those of the entire wind farm, as it quantifies the frequency-dependent correlation between their power outputs.

Random sweeping models describe the advection of atmospheric turbulence by a quasi-stationary, uniform sweeping velocity in space. Following Taylor's hypothesis, the turbulence is assumed to be frozen during this advection, which applies when the turbulence's evolution timescale is much longer than that of advection. Tobin and Chamorro [8] proposed a linear form of the random sweeping coherence model as

$$C_{RS}(\omega) = \underbrace{\exp\left(-\frac{i\omega\Delta_x}{V}\right)}_{\text{I}} \underbrace{\exp\left(-\frac{\omega^2\Delta_x^2\sigma_v^2}{2V^4}\right)}_{\text{II}} \underbrace{\exp\left(\frac{\Delta_y^2}{L_y^2}\right)}_{\text{III}} \quad (4.1)$$

where  $V$  denotes the average value of sweeping velocity  $v$ ,  $\sigma_v$  is the standard deviation, and  $\Delta_x$ ,  $\Delta_y$  represent the streamwise and spanwise spacing between two turbines. Term I in the model describes the phase lag in coherence, while Term II captures the exponential decay in coherence magnitude towards higher frequencies. Term III accounts for the coherence reduction due to the lateral separation with a decay length parameter  $L_y$ . Notably, the boundary layer turbulence mainly correlates power of turbine pairs aligned in streamwise direction, whereas the laterally separated turbines show much lower power coherence due to the streak structures that is much shorted in spanwise direction [12]. The Tobin model is a linear approximation of random

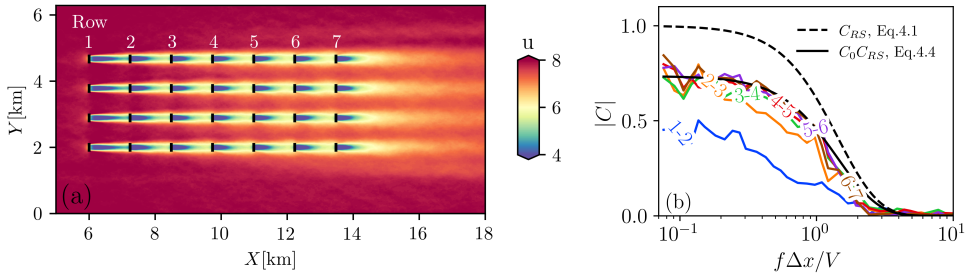


Figure 4.1.1: (a) Time-averaged flow field at hub height and (b) inter-row power coherence from wind farm LES. Dashed and solid lines indicate original random sweeping models (Eq. 4.1) and the coherence model proposed in this work (Eq. 4.4), respectively.

sweeping hypothesis, which only applies when  $\sigma_v$  is significantly smaller than the value of  $V$ . The ability of random sweeping models to represent turbulence coherence in wind farms has been validated by both experimental [7, 8] and numerical [9, 73, 78] studies.

However, these models only consider atmospheric conditions and ignore the influence of wind turbine wakes. Nevertheless, Liu and Stevens [9] showed that wind turbine wakes have a pronounced impact on the coherence of wind turbine power outputs. In particular, turbines capture energy from wind, which alter the inflow structure and introduce wake turbulence behind them. Consequently, the downstream wind turbines constantly operate in the wakes from upstream with slower and more fluctuating flow. Observations confirm that the wake turbulence reduces power coherence between turbines compared to random sweeping model predictions. The operational status of wind turbines as well as the wind farm layout have a pronounced impact on power coherence [8, 9].

Figure 4.1.1 shows the turbulence coherence between turbine rows measured from a wind farm LES. Whereas the coherence between first two rows is relatively low, the downstream turbines converge to the same coherence level. Comparison with dashed line in the same figure reveals that random sweeping model prediction by Eq. 4.1 overestimates the coherence in actual wind farms. Specifically, Eq. 4.1 indicates the coherence converging to unity at low frequencies, whereas the LES results show a coherence reduction that cannot be modeled by simply adjusting random sweeping parameters. It was pointed out that the coherence reduction factor can be considered as a premultiplied constant  $C_0$ , i.e. the power coherence function takes the form  $C_{WF} = C_0 C_{RS}$  [8,

9, 73], where the turbine impact on  $C_0$  is introduced through turbine induction factor  $a$ . Liu and Stevens [9] considered the coherence reduction due to the velocity deficit in wake region and proposed the relation of  $C_0 \sim 1 - a$ . However, this simple consideration ignores the wake deflection effect due to the turbine blockage, and underestimates the value of  $C_0$  observed in wind farm LES. In Figure 4.1.1, we also present the  $C_{WF}$  curves corrected by flow deflection model considered in this work. The excellent agreement between the model and LES results addresses the importance of capturing  $C_0$  in predicting power coherence of downstream turbines.

In this work, we investigate how wind turbine wakes influence the coherence between the power outputs of turbines within a wind farm. LES of wind farms with different turbine induction factor and inter-turbine spacing are carried out to examine the coherence patterns throughout the wind farms. We present a theoretical framework to model the prefactor  $C_0$  accounting for the wake effects. The model considers the wake deflection due to the turbine blockage effect, which provides accurate predictions in typical operation scenarios of wind farms. Additionally, we demonstrate that the decreased power coherence in the leading rows is resulted from the transition between atmospheric boundary layer dynamics and internal wind farm flow.

The rest of this work is organized as follows: Section 4.2 introduces the LES approach as well as the performed wind farm simulations. The coherence reduction mechanism associated to the wake effects are analyzed in Section 4.3. In Section 4.4, we illustrate the theoretical approach to model the coherence reduction prefactor, which is validated against LES results. In Section 4.5, we demonstrate how the development of wind farm internal boundary layer influence the power coherence of turbines at wind farm entrance region. The results and discussions are concluded in Section 5.5.

## 4.2 Large eddy simulations of wind farms

We perform wind farm simulations embedded in conventionally neutral atmospheric boundary layers (CNBLs), which is driven by geostrophic wind. The CNBLs are characterized by a neutral atmospheric boundary layer capped by a stable thermal stratification layer above. The buoyancy effect due to thermal stratification is modeled by Boussinesq approximation. The governing equations read:

$$\partial_i \tilde{u}_i = 0 \quad (4.2a)$$

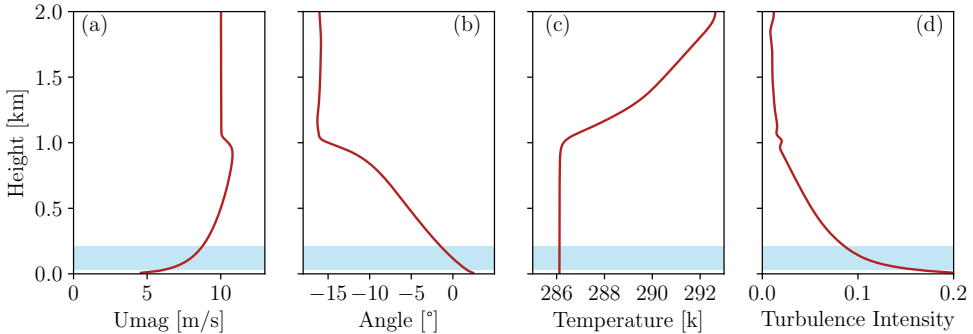


Figure 4.2.1: Inflow statistics of a conventional neutral boundary layer: (a) wind speed, (b) wind veer, (c) temperature, and (d) turbulence intensity. The blue-shaded region marks the turbine locations.

$$\partial_t \tilde{u}_i + \partial_j (\tilde{u}_i \tilde{u}_j) = -\partial_i \tilde{p}^* - \partial_j \tau_{ij} - \epsilon_{ijk} f_C (\tilde{u}_k - G_k) + g\beta(\tilde{\theta} - \langle \tilde{\theta} \rangle) \delta_{i3} + f_i \quad (4.2b)$$

$$\partial_t \tilde{\theta} + \tilde{u}_j \partial_j \tilde{\theta} = -\partial_j q_j \quad (4.2c)$$

The tilde represents the spatial filtering at the LES grid scale  $\Delta$ , and  $\tilde{u}_i$ ,  $\tilde{\theta}_i$  denotes the filtered velocity and potential temperature components, respectively. The driving pressure gradient is given by  $\epsilon_{ijk} f_C (\tilde{u}_k - G_k)$ , which is related to the geostrophic wind speed  $G$ , and  $\epsilon_{ijk}$  denotes the alternating unit tensor. The traceless part of the sub-grid scale (SGS) tensor,  $\tau_{ij} = \tilde{u}_i \tilde{u}_j - \tilde{u}_i \tilde{u}_j$ , as well as the SGS potential temperature flux, are modeled using the anisotropic minimum dissipation model. The filtered modified pressure is defined as  $\tilde{p}^* = \tilde{p} - p_\infty / \rho - \tau_{kk} / 3$ .  $g$  is the acceleration force due to gravity, and  $\beta = 1/\theta_0$  is the buoyancy parameter with respect to the reference potential temperature  $\theta_0 = 286$  k. The term  $f_i$  represents the turbine forces in the wind farm domain. Due to the high Reynolds number in the atmosphere, viscous stresses are neglected.

The flow domain is bounded with zero vertical velocity, zero shear stress and constant potential temperature gradient at the top, and periodic boundary conditions are applied in the streamwise and spanwise directions. The wall shear stress is modeled using the Monin-Obukhov similarity theory with a roughness height  $z_0 = 0.1$  m, representing flat-grassland terrain conditions. Zero surface heat flux at the lower boundary is considered for the neutral condition. Variables in the streamwise and spanwise directions are computed using the pseudo-spectral method, and second-order finite differences in the vertical direction are employed. Time integration is performed using a third-

order Adams-Bashforth scheme. For further details, we refer the reader to Gadde et al. [46].

To avoid a long fetch region in wind farm LES, we use the concurrent precursor method [40] with two domains running simultaneously. The precursor domain runs atmospheric boundary layer flow ( $f_i = 0$ ), generating realistic boundary layer turbulence. The flow is copied into the wind farm domain in the fringe region, which serves as the inflow for wind farm domain. Both precursor and wind farm simulations share the same domain and atmospheric inputs for a unified communication interface.

The geostrophic wind speed is set to  $G = 10$  m/s. A capping inversion layer with a temperature difference of  $\Delta\theta = 3$  K is imposed between  $H = 1.0$  and 1.2 km, and the free-atmosphere lapse rate is  $\Gamma = 5$  K/km. The Coriolis frequency is  $f_C = 10^{-4}$  s<sup>-1</sup>. A PID controller is used to maintain the hub-height wind direction aligned with the streamwise (longitudinal) axis [33]. Both the wind farm and precursor simulations are conducted in a domain of 25.12 km × 6.28 km × 2 km, with a grid resolution of 1024 × 256 × 256 in the streamwise, spanwise, and vertical directions, respectively. Figure 4.2.1 summarizes the key inflow characteristics. At hub height, the mean wind speed and turbulence intensity are observed to be  $U_{\text{hub}} = 8$  m/s and  $\text{TI} = 12\%$ .

We performed 13 wind farm simulations with varying inter-turbine spacings and induction factors, as summarized in Table 4.2.1. We use DTU 10 MW wind turbines [51], each with a rotor diameter of  $D = 178$ m and a hub height of  $z_{\text{hub}} = 119$ m. The wind farm is modeled using the actuator disk approach with a resolution of 7 points per rotor diameter, which is sufficient according to Stevens et al. [45]. We used the first 36 hours to stabilize transient effects of atmospheric boundary layer flow, and power data of turbines were recorded over 28 hours at a sampling frequency of 2Hz. To reduce spectral variability, the coherence spectra are averaged over time segments that evenly divide the original time series. Ten segments are used for the lowest frequencies, and 1280 segments for the highest frequencies.

## 4.3 Wake-induced coherence loss between turbines

To evaluate the mechanism of turbulence decoherence in atmospheric boundary layer, we compare the evolution of wind speed fluctuations with or without turbines present. Wind speed signals are measured at multiple positions upstream and downstream of the turbine locations for  $S_x = 7$ . Sampling points

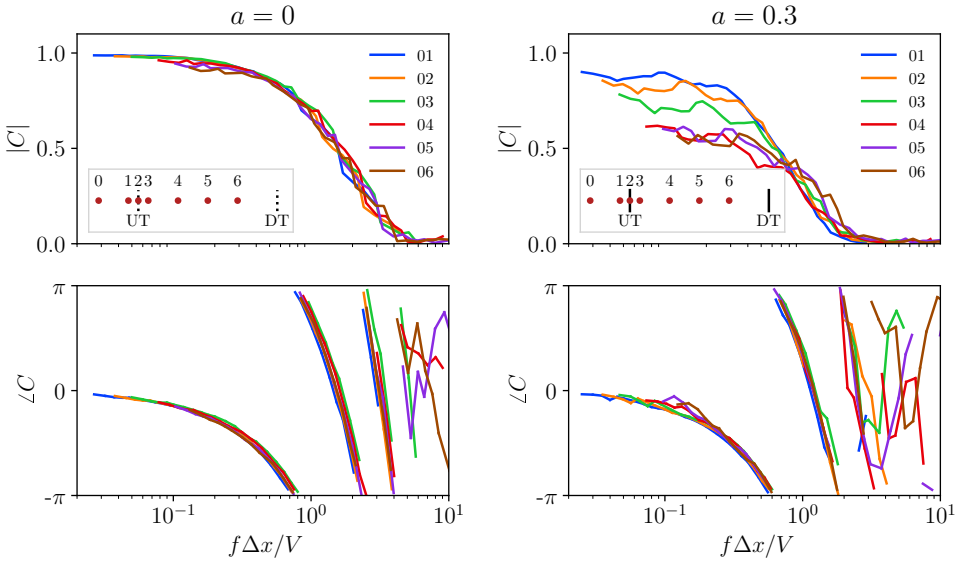


Figure 4.2.2: Coherence of wind speed fluctuations between sampled points ( $S_x = 7$ ) for  $a = 0$  (left) and  $a = 0.3$  (right). Top: magnitude of coherence; bottom: phase angle. The numbering and relative positions of the sampled points with respect to the upstream turbine are shown in the subplots, corresponding to  $X/D = \{-2, -0.5, 0, 0.5, 2, 3.5, 5\}$ . UT: upstream turbine; DT: downstream turbine.

are aligned along the hub-height centerline, with their positions relative to the turbine given by  $X/D = \{-2, -0.5, 0, 0.5, 2, 3.5, 5\}$ . Coherence is evaluated from the LES data as a function of the nondimensional frequency  $f \Delta x / V$ , where  $\Delta x$  is the streamwise separation and  $V$  the hub-height wind speed.

In undisturbed atmospheric flow ( $a = 0$ , shown in Figure 4.2.2 left), the local advection velocity  $V$  and the velocity fluctuations  $\sigma_v$  are approximately uniform. Under these conditions, the random sweeping model predicts that the phase (first factor in Eq. 4.1) and coherence magnitude (second factor in Eq. 4.1) as functions of non-dimensional frequency remain consistent across spacings. The LES results support these predictions, indicating that the model assumptions effectively capture atmospheric layer turbulence. Coherence spectra for various point separations show close agreement, with only a slight decrease at the largest separation (pair 0–6). These findings confirm that the random sweeping hypothesis reliably describes coherence in the atmospheric boundary layers over kilometer-scale separations and that natural decoherence

$S_x$	$S_y$	#Row	#Column	$a$
5	5	10	4	0, 0.15, 0.25, 0.35
7	5	7	4	0, 0.1, 0.2, 0.3, 0.35
14	5	6	4	0, 0.1, 0.2, 0.3

Table 4.2.1: Overview of wind farm setups for all simulations. Three streamwise turbine spacings  $S_x = 5, 7, 14$  are simulated, with each case considering a range of turbine induction factors.

in the atmosphere has only a small effect on the decay factor  $C_0$ .

The results for  $a = 0.3$  are shown in the right panels of Figure 4.2.2. For illustration, we select the fourth (upstream) and fifth (downstream) rows which are located inside the wind farm. Turbine wakes reduce the mean wind speed within the array relative to undisturbed atmospheric flow. To account for spatial variation in wind speed, we use the mean velocity between each turbine pair measured from LES as the sweeping velocity  $V$ , which allows an overlap of phase angle diagrams for different spacings displayed in the lower panel. At high frequencies, wake-induced turbulence lowers coherence and the phases become more scattered. In the upper panel, a significant decline in absolute coherence appears in the near-turbine region ( $-2D$  to  $2D$ ), indicating strong local disturbances caused by the turbine, whereas coherence remains consistent in the far-wake region ( $2D$  to  $5D$ ). These patterns show that  $C_0$  is primarily controlled by near-wake dynamics, while the far wake retains features of ambient turbulence transport.

## 4.4 Accounting for turbine wakes in random sweeping theory

Liu and Stevens [9] showed that wind turbines introduce turbulence decoherence by reducing wind speed through the rotor. Assuming coherence does not recover when wind speed fluctuations do, the coherence reduction factor is associated to the induction factor of upstream turbines, i.e.  $C_0 \propto 1 - a$ . This simple model assumes that the convection velocity  $V$  is unchanged between turbines. However, its accuracy degrades at higher induction factors  $a$ . For turbines operating at high induction factors, a pronounced induction zone forms upstream, the wind speed is reduced and a significant fraction of the flow is deflected around the rotor. The resulting deflected flow, whose

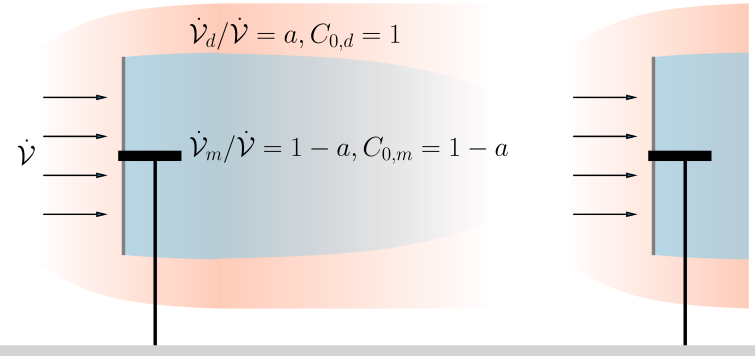


Figure 4.3.1: Illustrative sketch of the coherence model including the flow deflection effect as represented in Eq. 4.3.

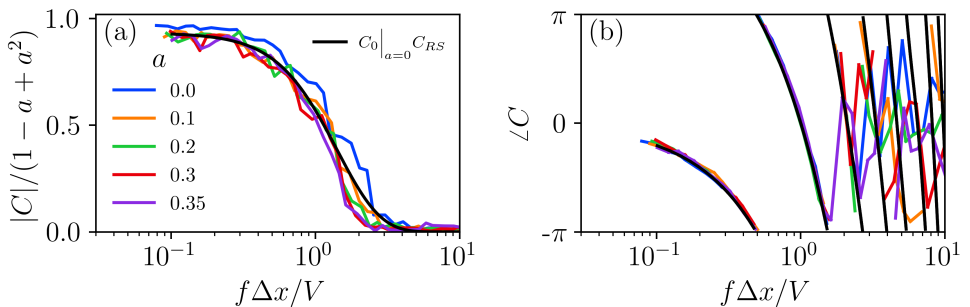


Figure 4.3.2: Velocity coherence at downstream turbines for different induction factors ( $S_x = 7D$ ).

turbulence is less influenced by the rotor, then mixes with the wake before reaching the downstream turbine.

To model this process, we adopt a stream-tube approach, illustrated in Figure 4.3.1. According to the rotor disk theory, the deflected flow occupies a volume fraction which is proportional to the turbine induction factor, i.e.  $\dot{V}_d/\dot{V} = a$ , while the main stream flow passing through the rotor occupies  $\dot{V}_m/\dot{V} = 1 - a$ . We assume that the deflected flow preserves coherence ( $C_{0,d} = 1$ ) and that the main stream coherence loss is  $C_{0,m} = 1 - a$  [9]. After mixing, the resulting coherence reduction factor becomes

$$C_0 \sim a \cdot C_{0,d} + (1 - a) \cdot C_{0,m} \sim 1 - a + a^2 \quad (4.3)$$

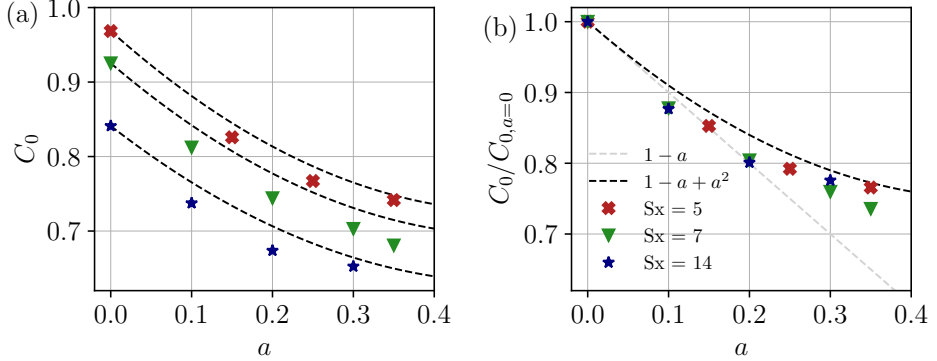


Figure 4.4.1: Fitted  $C_0$  values from LES results. (a) Coherence curves based on original LES data; (b) Results with the influence of natural atmospheric decoherence removed. Dashed lines indicate model predictions.

With the turbine induction factor  $a \in [0, 1]$  (practically between 0.1 and 0.4 for utility-scale turbines), the quadratic term  $a^2$  is positive, implying higher coherence than the first-order estimate  $C_0 \propto 1 - a$ . As  $a$  increases, more flow is deflected around the rotor, weakening the rotor's influence on downstream turbulence coherence. The deflection contribution is always smaller than the first-order wake term because  $a^2 \leq a$  on  $[0, 1]$ , so it can only partially offset the first-order reduction. Combining these effects, the general form of  $C_0$  can be written as

$$C_0 = (1 - a + a^2)F(\Delta x, z_0, z/L, \dots) \quad (4.4)$$

The function  $F(\Delta x, z_0, z/L, \dots)$  accounts for the decoherence due to the turbulence evolution in undisturbed atmospheric boundary layers, which is not considered in idealized random-sweeping prediction that assumes Taylor's hypothesis holds exactly. This coherence drop is not introduced by turbines, and it mainly depends on the streamwise spacing between turbine pairs ( $\Delta x = S_x D$ ) and on atmospheric conditions such as surface roughness  $z_0$  and atmospheric stability  $z/L$ , where  $L$  is the Obukhov length. LES results from Tobin et al. Tobin et al. [73] show that  $C_0$  decreases significantly under stably stratified low-turbulence conditions. We represent these atmospheric effects through  $F(\Delta x, z_0, z/L, \dots)$ , whose value, despite its complexity, can be obtained from undisturbed atmospheric boundary layer simulations by setting  $a = 0$  and fitting  $C_{WF} = C_0 C_{RS}$ , i.e.  $F(\cdot) = C_0|_{a=0}$ .

Figure 4.3.2 compares coherence spectra from LES and model prediction

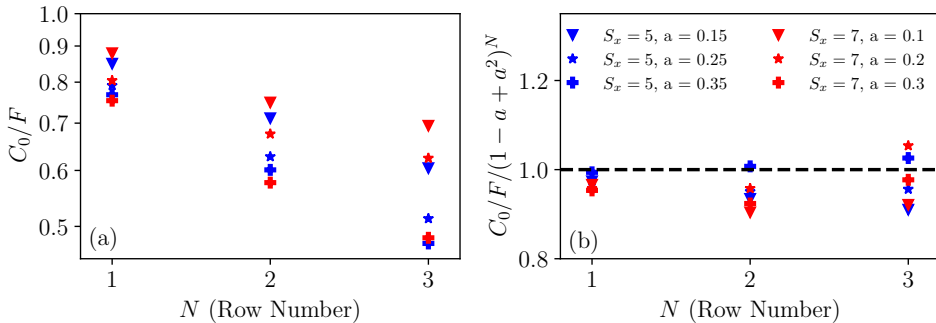


Figure 4.4.2: (a) Variation of  $C_0$  values across multiple turbine rows from LES; (b)  $C_0$  normalized by Eq. 4.5, as indicated by dashed line.

by Eq. 4.4 for a range of turbine induction factors  $a$ . In the model, the sweeping velocity  $V$  is determined as wind farm internal velocity obtained from LES. Figure 4.3.2b confirms that the determined sweeping velocity retains the convection properties of turbulence. In the absence of LES data, the internal wind speed can also be estimated by analytical wake models. The standard deviation  $\sigma_v = 0.96$  is taken as 12% of hub-height inflow wind speed. The black lines in the figure describe the random sweeping model predictions (Eq. 4.4) for  $a = 0.35$ . After normalization by  $(1 - a + a^2)$ , the spectra collapse across  $a$ , consistent with the model prediction. The  $a = 0$  case exhibits slightly higher coherence than the others. Notably, the magnitude of coherence can only overlap by having the same  $V$ , see Eq. 4.1. This zero-thrust case differs due to its higher internal wind speed, which leads to an elevated coherence level in the normalized coordinate system. Nevertheless, the overlap of cases with  $a > 0$  demonstrates the predictive ability of the deflected-flow model.

In Figure 4.4.1, we plot  $C_0$  values from LES as a function of induction factor for three different turbine spacings. These values are obtained by fitting the LES coherence curves to the random sweeping model,  $C_{WF} = C_0 C_{RS}$ . As in Figure 4.3.2, the parameters  $\Delta x$  and  $V$  in the random sweeping model are adjusted for each combination of  $S_x$  and  $a$ . Figure 4.4.1a shows that the natural atmospheric decoherence, represented by the  $a = 0$  cases, increases with  $S_x$ . For  $S_x = 7$ , the value of  $C_0$  remains above 0.9, indicating that Taylor's hypothesis of frozen turbulence is still reasonable. For large spacing,  $S_x = 14$ , the atmospheric coherence decreases further, and the violation of Taylor's hypothesis due to the flow structure evolution over the corresponding

distance ( $\Delta x \approx 2.5$  km) can no longer be neglected.

For  $a > 0$ , all cases follow the trend predicted by Eq. 4.4. To exclude the effect of natural atmospheric decoherence, we normalize  $C_0$  by  $C_0|_{a=0}$  in Figure 4.4.1b. For small  $a$ , the naive estimate ( $C_0 \propto 1 - a$ ) and the deflected-flow model ( $C_0 \propto 1 - a + a^2$ ) give similar predictions. As  $a$  increases, the proposed model captures the quadratic trend in the LES results by accounting for the relative coherence gain from flow deflection. The measured  $C_0$  from LES are all below the model predictions, indicating that Eq. 4.4 slightly overestimates  $C_0$  for  $a > 0$ . This occurs because the model assumes steady downstream convection of wake turbulence, whereas in reality the wake meanders dynamically, which perturbs the transfer of upstream turbulence to downstream turbines.

Theoretical considerations and LES results connect the drop of power coherence to the impact of turbine operation, which is described by the pre-multiplied factor  $C_0$  to correct original random sweeping models. When turbulent eddies pass through more rows, they are also altered by turbines multiple times, accumulating decoherence effects. Figure 4.4.2a shows the value of  $C_0$  for power coherence of wind turbines separated by multiple rows, showing  $C_0$  drops with increasing row number. We therefore generalize the above formulation of  $C_0$  to multiple rows by explicitly relating it to the row separation  $N$  as

$$C_0^N = (1 - a + a^2)^N F(N\Delta x, z_0, z/L\dots) \quad (4.5)$$

where  $N$  denotes the number of rows between turbines ( $N = 1$  for successive rows). The equation indicates a linear reduction in  $C_0/F$  when it is presented in logarithmic scale, which is evidenced by Figure 4.4.2a. Comparison with the model is presented in Figure 4.4.2b, where the LES-fitted  $C_0$  for  $N = 1, 2, 3$  are normalized by Eq. 4.5. Larger row numbers are not considered, since coherence is already very low. The model exhibits a close match with LES results, demonstrating its broad capability for predicting turbine power coherence in large wind farms. Although scatter grows with  $N$  as the coherence is already low, model deviations stay within 10%.

## 4.5 Effect of entrance-region flow dynamics on coherence

Building on these results, we examine why turbines in the entrance region deviate from the expected coherence pattern. While downstream coherence trends are well predicted by the random sweeping model, entrance-row tur-

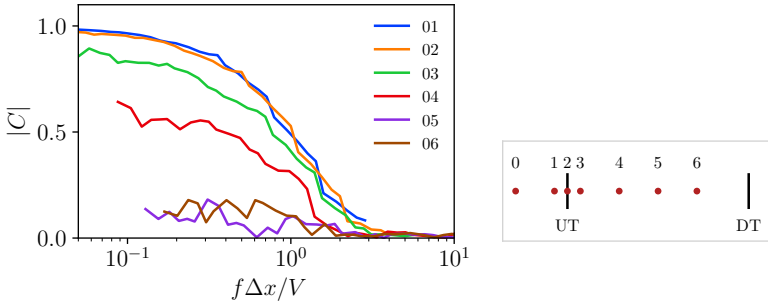


Figure 4.5.1: Velocity coherence between sampled points in the first turbine row ( $S_x = 7$ ,  $a = 0.35$ ). Point locations correspond to the same case as in Figure 4.2.2.

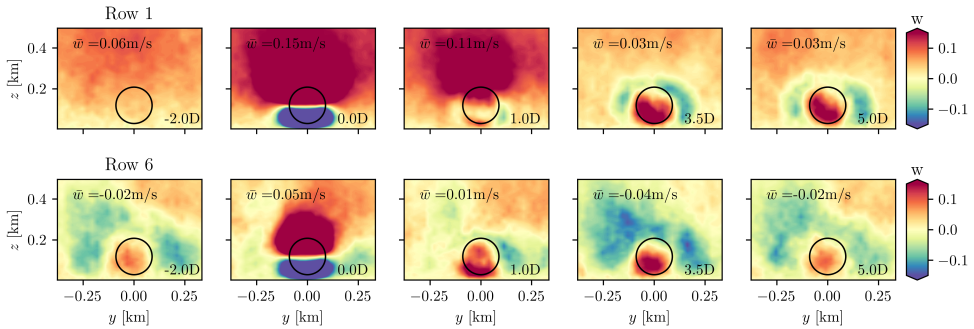


Figure 4.5.2: Visualization of time-averaged vertical velocity near turbines for  $S_x = 7$  and  $a = 0.35$ . Top: first row; bottom: sixth row. Black circles indicate the turbine location.

bines remain noticeably less coherent. Figure 4.5.1 shows the evolution of velocity coherence along the streamwise direction for the first row. Near the turbine (points 01-04), coherence decreases due to turbine operation, mirroring the trend in Figure 4.2.2. In the far-wake region (points 05-06), coherence drops sharply. We attribute this additional loss to the entrance-region transition from ambient atmospheric boundary layer flow to internal wind farm flow.

To explain the specific feature at far-wake region, Figure 4.5.2 compares vertical velocity fields near turbines at several streamwise positions for the first row and the sixth row; the latter represents the downstream wind farm region. In this region (lower panels of the figure), vertical velocity exhibits a periodic pattern: at the turbine location ( $0D$ ), the inflow is deflected around

the rotor and with the ground limiting downward motion, the net vertical motion is upward ( $\bar{w} > 0$ ). Farther downstream, the wake recovers and the flow descends due to mass conservation, with  $\bar{w} < 0$  at  $3.5D$  and  $5D$ . The patterns at  $5D$  and  $-2D$  are similar, corresponding to equivalent positions for adjacent rows separated by  $S_x = 7$ , consistent with our model assumptions.

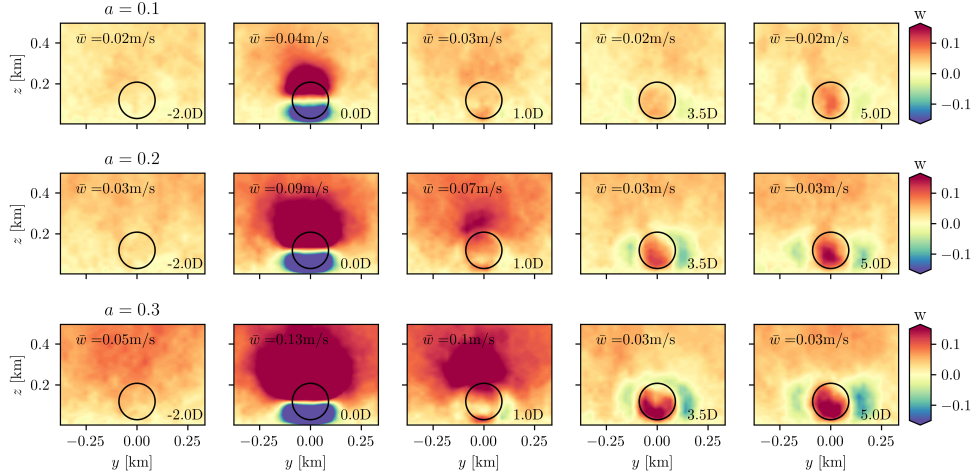


Figure 4.5.3: Visualization of time-averaged vertical velocity near first-row turbines for different induction factors:  $a = 0.1$  (top),  $a = 0.2$  (middle), and  $a = 0.3$  (bottom).

Flow around the first row differs from the fully developed region because an internal boundary layer forms at the wind farm entrance. This layer is characterized by higher turbulence intensity and lower mean wind speed than the ambient atmospheric boundary layer. The entrance transition drives a stronger upward motion that persists into the far wake ( $5D$ ), lifting turbulence structures above hub height. This vertical displacement reduces the similarity between upstream and downstream turbulence and lowers  $C_0$ , explaining the reduced first-row coherence relative to the fully developed region.

The transition effect is more pronounced for wind farms operate at higher thrust, as the difference in wind speed and turbulence levels between ambient flow and wind farm internal flow becomes greater. Figure 4.5.3 confirms that the flow deflection effects strengthen as the induction factor increases (cases  $a = 0.1$  to  $0.3$ ). Figure 4.5.4 shows that the coherence reduction between the first two turbine rows increases monotonically with  $a$ . For  $a = 0.1$ , the entrance effect is minimal and matches the downstream model closely, whereas

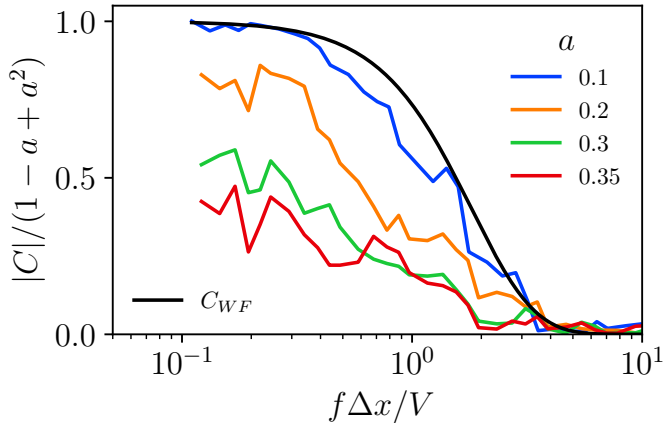


Figure 4.5.4: Induction-factor controlled decoherence effect at the entrance region of wind farms ( $S_x = 7$ ), demonstrated by power coherence of first two rows.

at higher thrust the coherence drops by more than half relative to the fully developed expectation when the spectra are normalized by  $1 - a + a^2$ . We note that turbine-level coherence exceeds pointwise measurements (cf. Figure 4.5.1,  $a = 0.35$ ) because disk-averaged velocity fluctuations integrate turbulence over the rotor diameter, making turbines less sensitive to small-scale flow redirection than individual probes.

## 4.6 Conclusions

We investigated the coherence spectra between wind turbines in a finite-size wind farm using large-eddy simulations (LES). Two regimes were identified: the entrance region and the downstream wind farm region. For turbines in the downstream region, traditional random sweeping models capture the spectral shape of coherence, but they overpredict its magnitude because wake effects are not included. We developed a theoretical framework that incorporates wake-induced coherence reduction via the factor  $C_0$ , reproducing coherence trends across a wide range of induction factors, turbine spacings, and downstream row separations in close agreement with LES. In the entrance region, coherence between the leading rows is still lower due to the formation of an internal boundary layer at the farm entrance, which deflects the flow over the array

and reduces turbulence coherence at hub height.

These results extend the applicability of random sweeping theory to operational wind farms and provide a physics-based framework for predicting wind farm power spectra and power correlations across different layouts, spacings, and operating conditions. The model is feasible for downstream wind farm region, which includes most of the turbines in the wind farm. The present formulation accounts for wake effects but does not yet parameterize entrance-region dynamics; incorporating this is expected to further improve performance assessments.



# 5

## Modeling multi-scale atmospheric interactions in wind farm power spectra<sup>◦</sup>

Wind farm power spectra display distinct regimes that reflect how turbines in the farm interact with the atmosphere. At low frequencies ( $\sim 10^{-4}$  Hz and below), turbine power outputs remain correlated, while at high frequencies ( $\sim 10^{-2}$  Hz and above), they become uncorrelated, smoothing out wind farm power fluctuations. Existing models typically address only one end of this spectrum and lack a unified framework for the transitional range ( $\sim 10^{-3}$  Hz). Here, we introduce a dynamic sweeping model that predicts wind farm power spectra across all scales. Low-frequency variations are represented as a time-dependent sweeping velocity that advects boundary-layer turbulence through the farm, while small-scale turbulence is captured using the random sweeping model. The model demonstrates that these different regimes originate from interactions between mesoscale weather systems, with typical timescales of 15 minutes to hours, and microscale atmospheric turbulence, which evolves over seconds to minutes. Large-eddy simulations and field data confirm that the model accurately reproduces the mesoscale, transitional, and turbulence-dominated regimes, providing a physically consistent basis for predicting wind farm power spectra and supporting the reliable integration of wind energy into the power grid.

---

<sup>◦</sup>To be submitted as: Y. Liu and R.J.A.M. Stevens, *Modeling multi-scale atmospheric interactions in wind farm power spectra*.



## 5.1 Introduction

Fluctuations in wind-farm power output, driven by atmospheric turbulence across multiple spatial and temporal scales, pose a fundamental challenge for integrating wind energy into power grids. Early measurements at Horns Rev documented significant fluctuations at farm scale [79], and this challenge increases as wind power penetration grows. Spectral analysis of wind-farm output is therefore crucial for determining storage and backup generation needs and for ensuring reliable grid integration [1, 80, 81].

To frame the problem, we distinguish between microscale and mesoscale atmospheric dynamics. Microscale turbulence, with scales below several kilometers and lifetimes of seconds to minutes [30, 82], governs interactions among neighboring turbines, whose outputs are only weakly correlated. Mesoscale variability, spanning 5–500 km and lasting minutes to hours [12, 19, 30, 83], controls correlations across farms. Bandi [3] showed that correlations decay to 0.5 at separations of about 300 km, implying that fluctuations can be suppressed by aggregating power from farms spread across different weather systems [84–86].

In practice, the industry typically relies on 10-minute averages for assessing wind resources and farm performance. While useful, these averages overlook sub-10-minute variability, which misses key atmospheric fluctuations that influence wind-power variability. High-resolution measurements (Figure 5.1.1) reveal three distinct regimes in wind-farm power spectra [23]: low frequencies ( $< 2 \times 10^{-4}$  Hz, timescales longer than 1.5 hours) where turbine outputs are correlated; high frequencies ( $> 3 \times 10^{-3}$  Hz, timescales shorter than five minutes) where outputs are largely uncorrelated; and an intermediate transitional regime ( $2 \times 10^{-4}$  to  $3 \times 10^{-3}$  Hz) where both effects overlap. Existing models capture the low- and high-frequency extremes: mesoscale models such as WRF describe slow variability [87], while random sweeping methods based on Taylor’s hypothesis account for fast fluctuations [7, 8]. However, their interactions are overlooked. Here, we propose a dynamic sweeping model that connects wind-power fluctuations across scales by treating slower variations as a time-dependent sweeping velocity that transports smaller-scale turbulence. This extension of the random sweeping concept provides the first consistent explanation of the transitional regime. Validated with large-eddy simulations (LES) and wind-farm measurements (Figure 5.1.1), the model reproduces the three observed spectral regimes. Our framework, therefore, offers a physical

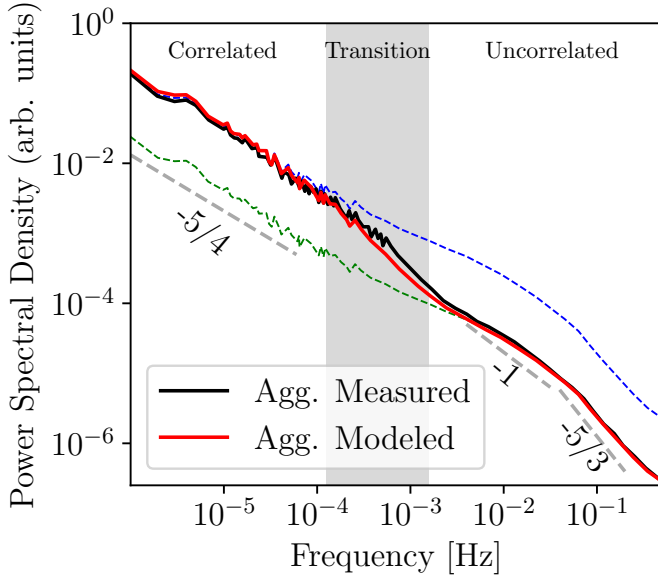


Figure 5.1.1: Aggregate power spectrum measured at Mt Mercer wind farm (black line) [23]. Red line indicates model predictions by Eq. 5.12, with inter-turbine coherence function modeled in Appendix 5.C. The blue and green lines indicate the upper and lower bounds of wind farm correlation based on the measured spectrum of single turbines.

model for predicting wind-power fluctuations.

In the remainder of the paper, we first introduce the theory in Section 5.2. In Section 5.3, we examine the coherence in power output between different turbine pairs in the wind farm, which reveals the physics of the three regimes. Section 5.4 discusses how these findings are reflected in the wind farm power spectra. Conclusions are presented in Section 5.5. Details on the simulations are provided in Appendix 5.A, and the modeling of the atmospheric spectra is described in Appendix 5.B and 5.C.

## 5.2 Theory

In Sections 5.2.1 and 5.2.2, we describe how microscale atmospheric turbulence is captured with the random sweeping model and how low-frequency variability is represented using the dynamic sweeping approach.

### 5.2.1 Random sweeping model

The random sweeping model [7–9, 73] assumes that the turbulent velocity field  $u$  is advected by a uniform sweeping velocity  $v$  across the domain. The advection of  $u$  is described by

$$\frac{\partial u}{\partial t} + v \frac{\partial u}{\partial x} = 0. \quad (5.1)$$

Using Taylor’s frozen turbulence hypothesis, the model is based on three main assumptions: (i) the turbulent motion is considered “frozen” during advection; (ii) wind turbines act as passive probes; and (iii) the sweeping velocity can be decomposed as  $v = V + v'$ . Here,  $V$  denotes the mean sweeping velocity, while  $v'$  represents the fluctuations. These fluctuations are assumed to follow a Gaussian distribution with zero mean and a standard deviation  $\sigma_v$ .

The streamwise coherence between turbines separated by  $\Delta x$  is given by integrating over all possible values of  $v'$  [8, 9]:

$$C_{RSM}(\omega) = \frac{\Phi_{0,\Delta_x}}{\Phi_{Mi}} = \frac{1}{\sigma_v \sqrt{2\pi}} \int_{-\infty}^{\infty} \prod_{n=0}^{\infty} \exp \left[ -\frac{i\omega\Delta_x}{V} \left( \frac{v'}{V} \right)^n - \frac{1}{2} \left( \frac{v'}{\sigma_v} \right)^2 \right] dv' \quad (5.2)$$

where the coherence function is defined by the ratio of the two-point cross-spectrum  $\Phi_{0,\Delta_x}$  and the power spectrum of single points  $\Phi_{Mi}$ , the assumption that wind turbines do not affect the flow is unrealistic for operational wind farms. Previous studies have shown that turbine wakes convert atmospheric turbulence into wake turbulence, reducing the power coherence between successive downstream turbines [8, 9, 88]. The loss of coherence is directly related to the upstream turbines’ induction factor  $a$ , as it controls the initial strength of the wake.

To model these effects, we consider the coherence between turbine pairs in the wind farm as follows:

$$C_{WF}(\omega) = C_0(a) C_{RSM}(\omega) \exp \left( \frac{\Delta_y^2}{L_y^2} \right). \quad (5.3)$$

The reduction in coherence resulting from wake-added turbulence is modeled by the prefactor  $C_0$ :

$$C_0(a) = (1 - a + a^2)^N F(\Delta_x), \quad (5.4)$$

where  $N$  indicates the number of rows separating two turbines, with  $N = 1$  representing consecutive turbine rows. The function  $F(\Delta_x)$  models decoherence over a distance  $\Delta_x$ , which depends on atmospheric conditions. When turbine effects are absent ( $a = 0$ ),  $F$  reduces to the constant  $C_0$  obtained from atmospheric flow LES. The exponential decay function  $\exp(-\Delta_y^2/L_y^2)$  describes the reduction in coherence due to spanwise separation, where  $\Delta y$  is the spanwise distance between turbine pairs and  $L_y$  is the spanwise coherence length [8]. Because the spanwise coherence length is much shorter than the streamwise coherence length [89], the effective spanwise coherence is limited. LES study [88] confirms that Eq. 5.4 captures the turbine-induced coherence reduction in a wide range of induction factors, turbine spacings, and number of rows.

### 5.2.2 The dynamic sweeping model

The random sweeping model assumes steady conditions to predict coherence due to microscale atmospheric turbulence. In reality, microscale wind conditions are controlled by mesoscale weather systems, which impose low-frequency changes in wind speed and wind direction. Observations indicate that these mesoscale variations are mostly uncorrelated with microscale turbulence because large-scale weather systems extend over tens of kilometers, which effectively decouples them from small-scale turbulence [12].

Therefore, for wind turbines within a wind farm, low-frequency wind speed variations can be viewed as a dynamic sweeping velocity that transports atmospheric turbulence past the turbines. We model the total wind speed variations  $U(t)$  as the sum of a dynamic sweeping velocity  $v(t)$  and the microscale atmospheric turbulence  $u(t)$ , i.e.,

$$U(t) = v(t) + u(t) \quad (5.5)$$

The linear Fourier transform in time provides the coefficients in frequency space:

$$\hat{U}(\omega) = \hat{v}(\omega) + \hat{u}(\omega) \quad (5.6)$$

To quantify the weight of mesoscale and microscale components, we introduce a function  $r(\omega)$  defined by the ratio of their power spectral intensity:

$$r(\omega) = \frac{\Phi_{Me}(\omega)}{\Phi_{Mi}(\omega)} = \frac{\langle \hat{v}\hat{v}^* \rangle}{\langle \hat{u}\hat{u}^* \rangle}. \quad (5.7)$$

The wind turbine power spectrum can then be expressed as:

$$\Phi_{MM} = \langle \hat{U} \hat{U}^* \rangle = \langle (\hat{v} + \hat{u}) (\hat{v}^* + \hat{u}^*) \rangle \quad (5.8a)$$

$$= \langle \hat{v} \hat{v}^* \rangle + \langle \hat{v} \hat{u}^* \rangle + \langle \hat{v}^* \hat{u} \rangle + \langle \hat{u} \hat{u}^* \rangle \quad (5.8b)$$

$$= (r + 1) \Phi_{Mi} \quad (5.8c)$$

We assume that mesoscale and microscale variations are uncorrelated, which means  $\hat{v}$  and  $\hat{u}$  are statistically independent. For a turbine pair separated by  $\Delta = [\Delta_x \ \Delta_y]^T$ , where  $\Delta_x$  and  $\Delta_y$  are the streamwise and spanwise distances, the cross-spectrum becomes

$$\begin{aligned} \Phi_{0,\Delta} &= \langle \hat{U}_\Delta \hat{U}_0^* \rangle \\ &= \langle (\hat{u}_\Delta + \hat{v}_\Delta) (\hat{u}_0^* + \hat{v}^*) \rangle \\ &= \langle \hat{u}_\Delta \hat{u}_0^* \rangle + \langle \hat{v}_\Delta \hat{v}^* \rangle \end{aligned} \quad (5.9)$$

where the cross terms cancel due to the independence of  $\hat{u}$  and  $\hat{v}$ . The first term on the right-hand side represents the microscale contributions, which are modeled using the random sweeping model  $\langle \hat{u}_\Delta \hat{u}_0^* \rangle = C_{WF} \Phi_{Mi}$ . The second term represents the mesoscale contribution, which we express as

$$\langle \hat{v}_\Delta \hat{v}^* \rangle = \zeta \Phi_{Me} = \zeta r \Phi_{Mi} \quad (5.10)$$

For the mesoscale atmospheric dynamics, we apply an exponential decay consistent with observations [2, 12, 31, 84, 90].

$$\zeta(\omega, \Delta) = \exp\left(-a_\Delta \frac{\omega \Delta}{V}\right) \quad (5.11)$$

Here  $a_\Delta$  denotes the decay coefficient. In contrast to small-scale atmospheric turbulence, which has little spanwise coherence, large-scale motions decay similarly in both horizontal directions, so  $a_{\Delta_x} \approx a_{\Delta_y}$ .

Combining Eqs. 5.8, 5.9, and 5.10, the final expression of the dynamic sweeping model is obtained

$$C_{MM} = \frac{\Phi_{0,\Delta}}{\Phi_{MM}} = \frac{\zeta r + C_{WF}}{r + 1}. \quad (5.12)$$

This expression connects meso- and micro-scale atmospheric effects through the ratio function  $r$ . For  $r \gg 1$ , low-frequency mesoscale effects dominate,

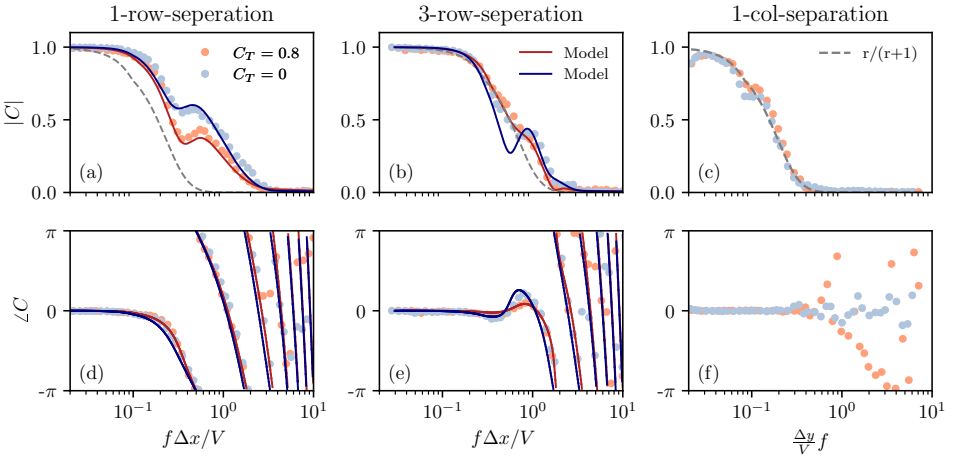


Figure 5.2.1: Coherence spectra from LES and the dynamic sweeping model (Eq. 5.12) for cases with zero turbine thrust ( $C_T = 0$ ) and maximum thrust ( $C_T = 0.8$ ). The top panels display the absolute coherence, while the bottom panels show the phase angle. Labels in panels (a), (b), and (c) apply to all subfigures.

and the coherence approaches the mesoscale coherence pattern, denoted by  $\zeta$ . For  $r \ll 1$ , microscale turbulence effects dominate, which are represented by the random sweeping model  $C_{WF}$ . In the intermediate range ( $r \approx 1$ ), the flow transitions between the two regimes, with influences from both determining the coherence.

Measurements indicate that wind turbine power correlations decrease exponentially with distance as  $\exp(-\Delta x/l_0)$  with a typical atmospheric integral length scale of  $l_0 = 300$  km [3]. Since typical wind farms are much smaller than  $l_0$ , we set  $a_\Delta = 0$  and take  $\zeta = 1$  in our model. This assumption is justified, as for a typical farm size of  $\Delta x_{WF} = 10$  km, the correlation between the farthest turbines remains about 0.97. For wind farms covering significantly larger areas, a more general coherence function  $\zeta(f)$  would be necessary to capture geographic smoothing effects. However, this extension is beyond the scope of the present study.

## 5.3 Coherence between turbine pairs

To model the coherence between turbine pairs, we perform LES of a wind farm composed of DTU 10MW turbines [51], with details of the simulation presented in Appendix 5.A. The layout consists of seven rows and four columns, with streamwise and spanwise spacings of  $S_x = 7$  and  $S_y = 5$ , respectively. We compare two scenarios: (1) zero thrust ( $C_T = 0$ ), where turbines passively record wind speed variations without generating wake turbulence, and (2)  $C_T = 0.8$ , where turbines operate below rated wind speed to maximize power. Because  $C_T = 0$  and  $C_T = 0.8$  represent extreme cases, they provide insight into the upper and lower bounds of the coherence and wind farm power spectra affected by turbine operation.

The coherence data are calculated from wind speed signals measured by each turbine, which equally reflect the power coherence under the context of constant  $C_T$ . The dynamic wind speed signal, described in Appendix 5.B, is applied after the flow is fully developed. Velocity data with a time length of 120 hours are collected, ensuring that the spectral calculations are statistically converged.

Figure 5.2.1 compares coherence spectra from LES and the model for turbines separated by one and three rows, as a function of normalized frequency  $f\Delta x/V$ . Spectra are averaged from the second row onward to reduce entrance effects [8, 9, 88]. The model closely matches the LES results for atmospheric flow without wind turbine wakes. At low frequencies, mesoscale processes dominate, while at higher frequencies, microscale turbulence becomes the main driver. The model also reproduces the non-monotonic behavior observed in the transitional regime, where peaks and troughs arise from the interference of frequencies. This occurs because the phase angle of the random sweeping model coherence shifts continuously with frequency, while the dynamic sweeping component remains real and positive.

The interaction between the wind farm and the atmosphere decreases wind speed and increases turbulence intensity. The lower wind speed is modeled in Eq. 5.2 by  $V = 0.85\bar{v}$ , derived from LES. As the wake-induced turbulence does not contribute to power coherence [8, 9], we still consider the standard deviation of inflow velocity in the model. Figure 5.2.1 compares two scenarios and shows that turbine wakes at  $C_T = 0.8$  reduce coherence relative to the atmospheric flow case ( $C_T = 0$ ), except at intermediate frequencies in panel (b), where frequency interference occurs.

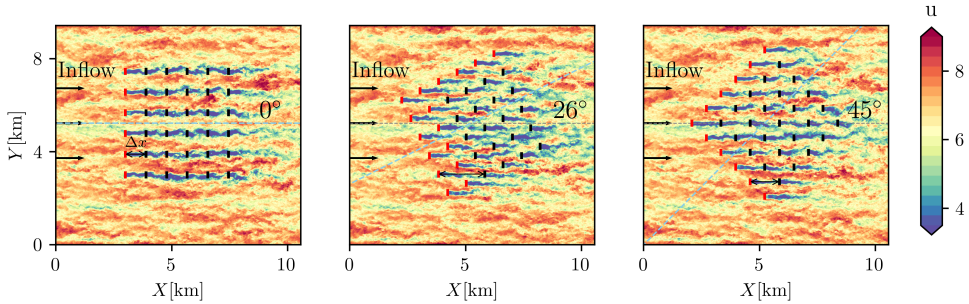


Figure 5.3.1: Top view of the wind farm configuration for different wind directions, with turbines receiving clean inflow highlighted in red.

The figure also shows the mesoscale contribution  $r/(r + 1)$  (dashed line); see the Appendix 5.B for details. The gap between this dashed line and the overall coherence (red line) highlights the contribution from microscale atmospheric turbulence. For turbine pairs separated by three rows, the microscale contribution becomes negligible as the LES results converge to the imposed mesoscale signal (Figure 5.2.1b). In the spanwise direction, no microscale coherence is observed, with the LES results fully overlapping the imposed signal (Figure 5.2.1c). Consequently, at low frequencies, the turbine power output is primarily correlated with these large-scale variations, consistent with the component  $r/(r + 1)$ . The strong power correlation is consistent with field observations [3, 22, 23], which cannot be achieved through microscale turbulence [8, 9]. At higher frequencies, microscale turbulence leads to sustained decoherence between turbines in the wind farm. Finally, we emphasize that the rapid phase angle changes at high frequencies have no physical impact, as the coherence is effectively zero in this range.

## 5.4 Wind farm spectra

To assess the model's predictive ability for the overall wind farm power spectrum, we analyze a  $5 \times 5$  wind farm with turbines evenly spaced at  $S_x = S_y = 5$ . Three wind directions are considered ( $0^\circ$ ,  $26^\circ$ , and  $45^\circ$ ; see Figure 5.3.1). In the  $0^\circ$  case, the streamwise spacing between consecutive turbines is smallest and wake effects in the wind farm are strongest. At  $26^\circ$ , 16 of the 36 tur-

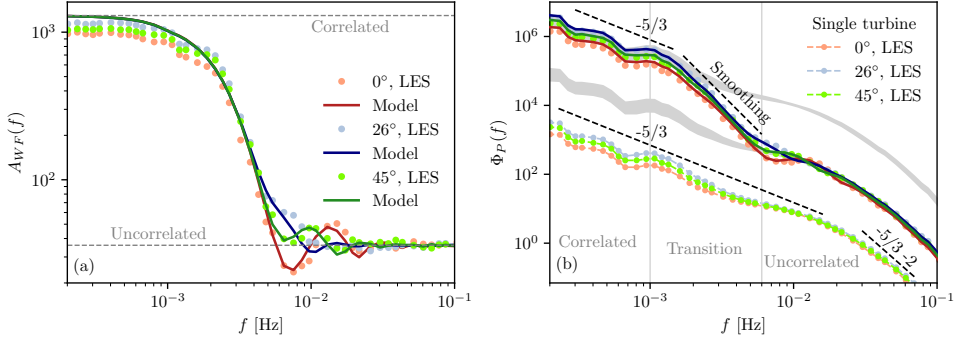


Figure 5.3.2: Aggregate wind farm power output from LES (dotted lines) and model from Eq. 5.13 (solid lines). (a) Admittance function. (b) Power spectra of single turbines (lower curves) and the entire wind farm (upper curves). The grey lines in panel (b) illustrate an extrapolation of the fully correlated and uncorrelated scenarios as a guide for the eye. Legends apply to both panels.

bines experience free inflow, increasing the overall wind farm power output. Wake effect are represented by  $V = 0.85\bar{v}$  ( $0^\circ$ ),  $0.95\bar{v}$  ( $26^\circ$ ), and  $0.9\bar{v}$  ( $45^\circ$ ), as determined from LES. Collectively, these scenarios illustrate how wind farm performance varies with wind farm layout.

Assuming the power output spectra of all turbines are statistically identical, the total wind farm spectrum is given by

$$\Phi_{WF}(\omega) = A_{WF}(\omega)\Phi_1(\omega) \quad (5.13)$$

where the admittance function sums the real part of the coherence between all turbine pairs,

$$A_{WF}(\omega) = n + 2 \sum_{i=1}^{n-1} \sum_{j=i+1}^n \text{Re}(C_{ij}(\omega)) \quad (5.14)$$

The admittance function measures instantaneous power correlations between turbines, with  $A_{WF} = n^2$  representing the fully correlated limit and  $A_{WF} = n$  representing the uncorrelated limit.

Figure 5.3.2a compares LES results with model predictions for the admittance function, showing that the model accurately reproduces the observed trends. Low-frequency variations up to  $10^{-3}\text{Hz}$  (about a 16-minute timescale) remain highly coherent and mostly independent of wind farm layout, resulting

in  $A_{WF} = n^2 = 36^2$ . Above  $2 \times 10^{-2}$ Hz ( $\approx$  1-minute timescale), fluctuations become uncorrelated and  $A_{WF}$  approaches its lower limit of  $n = 36$ . Layout effects appear in the intermediate region ( $5 \times 10^{-3}$  to  $2 \times 10^{-2}$ Hz), where turbine spacing and alignment influence coherence between turbine power outputs [7, 78]. The streamwise distance  $\Delta x$  between turbine rows determines the interference frequencies, while the number of downstream turbines controls their magnitude. The  $0^\circ$  layout, with perfect alignment, exhibits the strongest interference [78], whereas the  $26^\circ$  case shows the weakest, and  $45^\circ$  lies between. We note that LES amplifies this signature compared to field data, since in reality the wind rarely remains perfectly aligned with the wind farm layout for extended periods.

Figure 5.3.2b compares spectra from single turbines with the aggregate wind farm spectrum. From the wind farm spectral density compared to individual turbines, we identify the correlated ( $\lesssim 10^{-3}$  Hz), uncorrelated ( $\gtrsim 6 \times 10^{-3}$  Hz) regimes and the transitional regime ( $10^{-3}$  Hz to  $6 \times 10^{-3}$  Hz). Notably, the bounds of different regimes are directly connected to the mesoscale contributions, see Figure 5..1b in Appendix 5.B. In the low-frequency region, the power spectral density of individual turbines depends on wind direction: the  $26^\circ$  case yields the highest power output and fluctuations, whereas the aligned  $0^\circ$  case produces the lowest. At these frequencies, the farm spectrum follows the same scaling as individual turbines because the admittance function remains close to its maximum value, indicating that the wind power is highly correlated inside the wind farm. This aligns with earlier findings that wind farm power spectra follow a  $-5/3$  scaling for timescales longer than 10 minutes [1, 3, 23].

Single-turbine spectra gradually converge in the transitional regime, suggesting that the influence of microscale turbulence is largely independent of wind direction. Within the transitional regime, the wind farm spectrum steepens, reflecting a loss of coherence between the power outputs of individual turbines. This spectral drop indicates that the wind farm power smoothing effect is mainly due to the weak correlation of turbine output resulting from microscale processes at higher frequencies. In an uncorrelated region, power fluctuations on the wind farm level are sufficiently smoothed, and the spectral scaling returns to the same as that of individual turbines. Additionally, we observe a sharper  $f^{-5/3-2}$  scaling in turbine spectra at the high-frequency end, which is likely due to the filtering effects of the rotor. Studies [91, 92] suggest that this scaling arises at frequencies lower than 0.07 Hz (the rotor scale), which is in agreement with our observations. Observing the transitional

and high-frequency regimes requires measurements with finer resolution than the standard 10-minute averages typically used in wind energy practice. Nevertheless, wind farm power production data, as shown in Figure 5.1.1, have clearly evidenced these regimes.

## 5.5 Conclusions

This study introduces the dynamic sweeping model as a unified framework for predicting wind farm power fluctuations across three distinct frequency regimes. The model integrates mesoscale atmospheric variability, microscale turbulence, and turbine-induced wakes into a single formulation. It shows that the three regimes arise from interactions between large-scale weather systems and small-scale atmospheric turbulence. In the low-frequency regime, turbine power fluctuations are associated with mesoscale variations and remain correlated with them. At high frequencies, microscale atmospheric turbulence dominates and turbine outputs become uncorrelated. In the transitional range, spectral smoothing effects of wind farm power outputs appear. LES and field observations confirm that the model accurately captures the wind farm's response to the transition of multi-scale turbulence sources and reproduces all three regimes. This provides a physically consistent basis for characterizing the power spectra of wind farms.

By enabling reliable modeling of wind farm power spectra, this framework supports improved integration of wind energy into the power grid and lays a foundation for future work. Knowledge of spectral behavior can inform estimates of the required capacity and response time of ancillary batteries and reserve power plants needed to balance the power production of wind farms. The known spectral form, when incorporated into stochastic load scheduling protocols, could help alleviate dynamic load balancing challenges. Similar spectral limits for other renewable sources, such as solar, could ultimately guide policy decisions and support the design of an optimal energy mix for regional grids with defined resource constraints [3, 93].

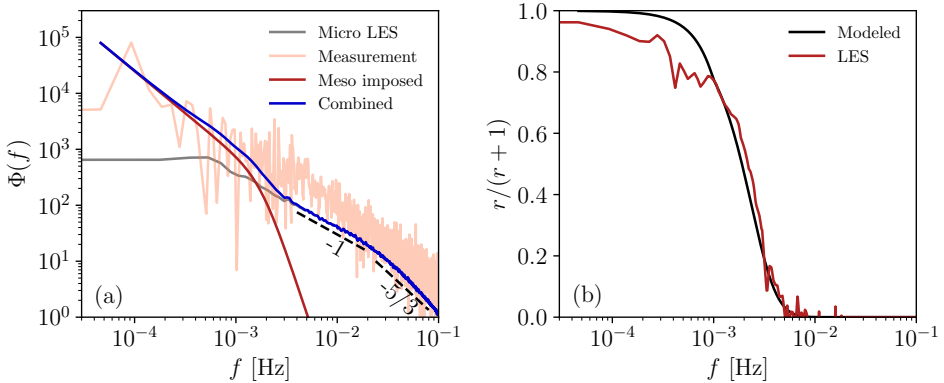


Figure 5..1: (a) The atmospheric spectra reproduced in LES, shown at height 87 m. The “Micro LES” represents the wind spectrum measured from a standalone LES, “Meso imposed” is the imposed low-frequency wind speed signal accounting for mesoscale contributions, and “Combined” is the composite spectrum of “Micro LES” and “Meso imposed”. (b) The mesoscale contributions as a function of frequency measured from LES, along with the model results from Eq. 5.16.

## Appendix

### 5.A Large-eddy simulations of wind farms

To validate the dynamic sweeping model, we performed wind farm LES. The simulations were carried out for a neutral pressure-driven boundary layer. The numerical scheme uses pseudo-spectral methods in the horizontal directions, second-order finite differences in the vertical direction, and second-order Adams–Bashforth time integration. The flow domain is bounded at the top by zero vertical velocity and zero shear stress. The wall shear stress at the surface is modeled using Monin–Obukhov similarity theory with a roughness height of  $z_0 = 0.1$  m. All simulation parameters are non-dimensionalized using the domain height  $H$  and reference friction velocity  $u_*|_{t_0}$ , yielding a non-dimensional time scale  $t_{\text{ndim}} = H/u_*$ . For further details, readers may refer to other works

[46, 74].

To provide realistic turbulent inflow, we use concurrent precursor simulations following [40] and [33]. We adopt the approach proposed by [54] to model low-frequency wind speed fluctuations in wind farm simulations. The corresponding LES equations are as follows.

$$\partial_t \tilde{u}_i = 0 \quad (5.15a)$$

$$\partial_t \tilde{u}_i + \partial_j (\tilde{u}_i \tilde{u}_j) = -\partial_i \tilde{p}^* - \partial_j \tau_{ij} - \frac{\partial_i p_\infty}{\rho} + f_i + v \delta_{i,1}, \quad (5.15b)$$

where the tilde  $\sim$  denotes spatial filtering at the grid scale  $\Delta$ , and  $-\partial_i p_\infty / \rho$  represents the imposed driving pressure gradient, which synchronizes with the prescribed wind speed. The subgrid-scale stress tensor is defined as  $\tau_{ij} = \tilde{u}_i \tilde{u}_j - \tilde{u}_i \tilde{u}_j$  and modeled using the anisotropic minimum dissipation model. The filtered modified pressure is expressed as  $\tilde{p}^* = \tilde{p} - p_\infty / \rho - \tau_{kk} / 3$ . Turbine forces within the wind farm domain are denoted by  $f_i$  and are modeled with an actuator disk model [45]. Viscous stresses are ignored because the Reynolds number in the atmosphere is very high. The time derivative of the imposed wind speed signal,  $v \delta_{i,1}$ , accounts for the forcing to drive low-frequency velocity changes, where  $\delta_{i,1}$  is the Kronecker delta, indicating that  $v$  acts only in the streamwise direction.

In Section 5.3, the simulations were performed with a domain size of 12.56 km  $\times$  6.28 km  $\times$  1 km on a  $512 \times 256 \times 128$  grid for both the precursor and the wind farm domain. The horizontal resolution of 24.5 m ensures that the DTU 10MW turbine disk can be resolved with 7 grid points per diameter, which is sufficient for actuator disk representation in wind farm LES [45, 94]. For the wind farm in Section 5.4, we adopted the simulation domain size of 12.56 km  $\times$  9.42 km  $\times$  1 km with the same spatial resolution.

## 5.B Modeling atmospheric spectra

In Figure 5..1a, we show the spectrum of the imposed inflow wind speed in the wind farm LES. The velocity spectra demonstrate how our modeling approach allows the imposed low-frequency wind speed signal to smoothly blend with the high-frequency wind speed fluctuations that LES naturally captures. As a result, the simulation captures both low-frequency (mesoscale) and high-frequency (microscale) velocity fluctuations. This combination (blue line) produces a spectrum representative of atmospheric turbulence.

The low-frequency wind speed fluctuations are obtained from field measurements at the National Wind Technology Center (NWTC) [50, 54]. On January 28, 2018, six hours of wind speed data (4:30–10:30 a.m.) were collected at height  $z = 87$  m using the M5 meteorological mast, which is shown in Figure 5..1a as “Measurement”. This signal was smoothed and filtered with a second-order Butterworth filter (cut-off frequency  $f_c = 1.8 \times 10^{-3}$ Hz, corresponding to a timescale of about 9 minutes) to remove high-frequency components before being introduced into the LES. The imposed sweeping velocity signal has a mean wind speed of  $\bar{v} = 12.14$ m/s and a standard deviation of  $\sigma_v = 2.89$  m/s at hub height. For standalone LES, the turbulence intensity at hub height is about 12%, corresponding to a standard deviation of  $\sigma_u = 1.53$  m/s. Assuming the sweeping velocity and turbulence fluctuations are uncorrelated, the combined standard deviation is  $\sigma_{v+u} = \sqrt{\sigma_v^2 + \sigma_u^2} = 3.25$  m/s.

Both the LES and the dynamic sweeping model use the same input spectrum. This allows for a direct comparison and highlights which spectral features are most important. Because atmospheric spectra vary by site, the framework can assess how these differences influence wind farm power spectra by adjusting the mesoscale input of the model. As shown in Figure 5..1a, there is almost no spectral gap between the low-frequency mesoscale and high-frequency microscale ranges for the spectrum used in this study. The identification of the different regimes (see Figures 5.1.1 and 5.3.2) is not sensitive to the details of the imposed spectrum.

In microscale wind speed spectra, there exist  $f^{-1}$  and  $f^{-5/3}$  regions, which reflect the identity of wavenumber spectra in turbulent boundary layers [7, 11, 13]. Meanwhile, field observations find that the wind power spectra follow a continuous  $f^{-5/3}$  law across multiple scales [1]. Considering the mesoscale contributions to be the difference between full-scale and microscale spectra, we model the ratio function  $r_s(f)$  as

$$r_s(f) = \begin{cases} 0, & f > f_z \\ (f/f_z)^{k_s+1} - 1, & f \in (f_H, f_z] \\ (f/f_z)^{k_s+1} \cdot (f/f_H)^{-1} - 1, & f \in (f_0, f_H] \\ (f_0/f_z)^{k_s+1} \cdot (f_0/f_H)^{-1} - 1, & f \leq f_0 \end{cases} \quad (5.16)$$

where  $k_s = -5/3$  is the scaling of full-scale spectrum,  $f_z$  and  $f_H$  are the low-frequency end of  $f^{-5/3}$  and  $f^{-1}$  regions in microscale spectra, and  $f_0$  corresponds to the integral time scale of mesoscale processes.

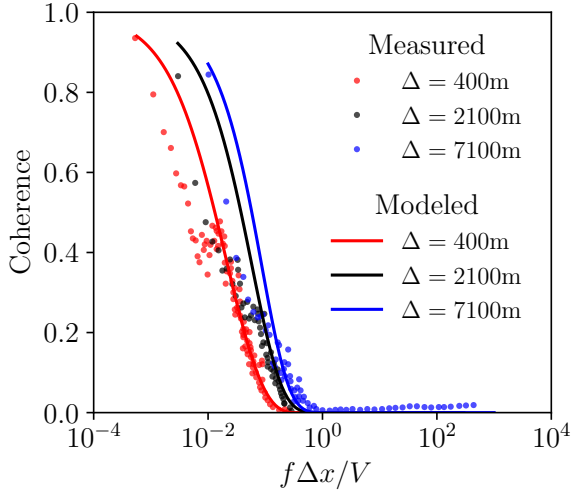


Figure 5.B.1: Measured coherence for different turbine pairs corresponding to Figure 5.1.1, adapted from Naemi and Brear [23]. Solid line indicates the modeled coherence by Eq. 5.17.

We note that wind conditions vary across sites, and a spectral gap between mesoscale and microscale regions can sometimes be observed [12, 90]. This deviation from an idealized  $f^{-5/3}$  spectrum can be represented using a gap function,  $\zeta_G(f) = A \exp(-Bf/f_z)$ , where  $A$  controls the offset in the mesoscale region and  $B$  represents the width of the spectral gap at the mesoscale–microscale interface. Both constants can be adapted from the wind spectrum, and the corresponding mesoscale ratio function is expressed as  $r(f) = r_s(f) \zeta_G(f)$ . Figure 5..1b compares the modeled mesoscale coherence,  $r/(r + 1)$ , with LES results. Using  $f_z = 3 \times 10^{-2}$  Hz,  $f_H = 10^{-3}$  Hz,  $A = 0.9$ ,  $B = 24.6$ , and  $f_0$  as the lowest imposed frequency, the parametrization reproduces the ratio of mesoscale and microscale components in the LES.

## 5.C Modeling wind farm data in Figure 5.1.1

In Figure 5.B.1, we present coherence functions measured from the same wind farm as in Figure 5.1.1, used to obtain the model spectrum shown here. Data with different colors are collected for a range of turbine spacings, from 400 meters to 7100 meters, with an average wind speed of  $V = 7.1$  m/s. The

400 m spacing is significantly smaller than the scale of mesoscale processes, which shows the highest wind power correlation. Interestingly, Coherence in the high-frequency range ( $f > 10^{-3}$  Hz) is not evident, even for the closest turbine pairs. This absence of microscale coherence is attributed to the effects of terrain and continuous wind condition changes during the measurement, which are more complex than those in well-controlled laboratory or numerical environments. Nevertheless, the transition from highly coherent mesoscale structures to low coherence in the high-frequency range is consistent with our explanations. Since no mesoscale components are observed in  $f \in (f_h, f_z]$ , we use a simplified ratio functions as:

$$r_s(f) = \begin{cases} 0, & f > f_H \\ (f/f_H)^{k_s} - 1, & f \in (f_0, f_H] \\ (f_0/f_H)^{k_s} - 1, & f \leq f_0 \end{cases} \quad (5.17)$$

From Figure 5.1.1, we identified  $f_z \approx 3 \times 10^{-2}$  Hz and  $f_H \approx 2 \times 10^{-3}$  Hz. In mesoscale range, the wind spectrum shows  $f^{-5/4}$  scaling, therefore we take  $k_s = -5/4$ ,  $A = 0.12$  and  $B = 1.1$ . To account for the mesoscale decay trend, we take  $a_\Delta = 1.3$  for  $\zeta$  in Eq. 5.11. Figure 5.B.1 confirms that the model captures the measured coherence inside the wind farm, which is then used to model the wind farm spectra, Figure 5.1.1.

# Conclusions and Outlook

In this thesis, we provide insights into wind farm performance under dynamic inflow conditions. Both large-eddy simulation (LES) techniques and analytical modeling reveal that dynamic scenarios exhibit distinct effects compared to steady-state conditions, particularly in terms of inflow characteristics, wake evolution, and power correlations. These findings establish a fundamental framework for studying wind farm flow dynamics in greater depth.

In Chapter 1, we develop techniques to accurately represent time-varying wind conditions in wind farm LES. The simulations show that dynamic inflow drives transient wake effects, which significantly influence the power output of downstream turbines - effects not captured in previous steady-state simulations. In parallel with the numerical investigation, we also consider a physics-based dynamic wake model (not included in the thesis), which confirms the physical consistency of the dynamic flow behavior observed in LES. This model can account for wind direction changes and varying boundary layer types, enabling more realistic assessments of wind farm performance. While Chapter 1 focuses on neutral turbulent boundary layers, atmospheric boundary layer dynamics become more complex when the Earth's rotation is included. In Chapter 2, we incorporate the Coriolis force, which causes wind veer with height, by introducing a time-varying pressure gradient to represent changing geostrophic wind speeds in LES. The coupled evolution of wind speed and direction is examined using LES, and a reduced-order model is proposed to predict trends in the atmospheric boundary layer. These contributions improve our understanding of dynamic boundary layer behavior and support better wind farm design and optimization.

In Chapter 3, we shift focus to power correlations between turbines in a wind farm. Time series of power output from LES are used to validate predictions from the random sweeping model. We find that turbine operation reduces wind power correlations—an effect not considered in the original model, which assumes below-rated operation with stable induction. Specifically, the coherence of turbine pairs operating above rated wind speed is not captured by existing random sweeping theory. Chapter 4 explores this in detail, showing that coherence patterns can be categorized into two regimes depending on the formation of the internal boundary layer within the wind farm. A wake-corrected random sweeping model is developed that incorporates turbine wake effects through the induction factor. LES validation confirms that this new

model captures power coherence across a range of turbine induction factors, spacings, and row separations.

Building on this understanding of microscale coherence, Chapter 5 extends coherence modeling to mesoscale variations. We introduce the dynamic sweeping model, which combines both mesoscale and microscale turbulence effects and successfully predicts full-scale wind farm power spectra. LES confirms that the model captures three distinct regimes of wind farm power fluctuations: a highly correlated low-frequency regime, an uncorrelated high-frequency regime, and a transitional mesoscale-to-microscale smoothing regime. These are physically explained and accurately reproduced by the dynamic sweeping framework.

This thesis aims to establish a deeper understanding of wind farm flow physics under dynamic atmospheric conditions, using a combination of physical modeling and numerical simulations. While microscale processes under steady inflow have been extensively studied, modeling the mesoscale–microscale interface remains a major challenge. A direct comparison between simulations and field data is difficult unless atmospheric variability is consistently represented in both. Although the methods introduced in this thesis focus on neutral boundary layer conditions, changes in thermal stratification—driven by diurnal and seasonal cycles—often coincide with wind speed fluctuations. Our modeling approach can be extended to other boundary layer types, offering a path toward realistic wind farm performance assessment under fully dynamic atmospheric conditions. Moreover, the results presented here can support more accurate wind farm parameterizations in mesoscale weather models, improving our understanding of the two-way interactions between large-scale weather systems and wind farm flow physics.

The wind farm physics under dynamic wind conditions is essential for design and optimization of wind farms, which is not yet considered in wind farm modeling. To approach more realistic situations, a fully dynamic modeling that captures inflow characteristics, wake effects and power coherence consistent with LES results needs to be established. This is particularly meaningful for initial-stage decision making by policy makers and wind farm operators, as wind farm LES is still too expensive in many situations.

# References

- [1] J. Apt. “The power spectrum of power from wind turbines”. In: *J. Power Sources* 169 (2007), pp. 369–374.
- [2] P. Milan, M. Wächter, and J. Peinke. “Turbulent Character of Wind Energy”. In: *Phys. Rev. Lett.* 110 (2013), p. 138701.
- [3] M. M. Bandi. “Spectrum of Wind Power Fluctuations”. In: *Phys. Rev. Lett.* 118 (2017), p. 028301.
- [4] R. J. A. M. Stevens and C. Meneveau. “Flow Structure and Turbulence in Wind Farms”. In: *Annu. Rev. Fluid Mech.* 49 (2017), pp. 311–339.
- [5] P. Veers et al. “Grand challenges in the science of wind energy”. In: *Science* 366.6464 (2019), eaau2027.
- [6] S. T. Frandsen. *Turbulence and turbulence-generated structural loading in wind turbine clusters*. Risø report R-1188 (Roskilde, Denmark), 2007.
- [7] J. Bossuyt, C. Meneveau, and J. Meyers. “Wind farm power fluctuations and spatial sampling of turbulent boundary layers”. In: *J. Fluid Mech.* 823 (2017), pp. 329–344. doi: 10.1017/jfm.2017.328.
- [8] N. Tobin and L. P. Chamorro. “Turbulence coherence and its impact on wind-farm power fluctuations”. In: *J. Fluid Mech.* 855 (2018), pp. 1116–1129.
- [9] Y. Liu and R. J. A. M. Stevens. “Turbulence coherence in wind farms: The role of turbines”. In: *J. Phys. Conf. Ser.* 2767 (2024), p. 092108.
- [10] Bowen Li et al. “Mesoscale modeling of a “Dunkelflaute” event”. In: *Wind Energy* 24.1 (2021), pp. 5–23.
- [11] M. Wilczek, R. J. A. M. Stevens, and C. Meneveau. “Spatio-temporal spectra in the logarithmic layer of wall turbulence: large-eddy simulations and simple models”. In: *J. Fluid Mech.* 769 (2015), R1.
- [12] X. G. Larsén, S. E. Larsen, and E. L. Petersen. “Full-scale spectrum of boundary-layer winds”. In: *Bound.-Layer Meteorol.* 159 (2016), pp. 349–371.
- [13] So-Kumnenh Sim, Joachim Peinke, and Philipp Maass. “Signatures of geostrophic turbulence in power spectra and third-order structure function of offshore wind speed fluctuations”. In: *Scientific Reports* 13.1 (2023), p. 13411.

- [14] A. J. Smits, B. J. McKeon, and I. Marusic. “High Reynolds number wall turbulence”. In: *Annu. Rev. Fluid Mech.* 43 (2011), pp. 353–375.
- [15] F. Porté-Agel, M. Bastankhah, and S. Shamsoddin. “Wind-Turbine and Wind-Farm Flows: A Review”. In: *Boundary-Layer Meteorol.* 74 (1 2020), pp. 1–59.
- [16] Anja Stieren and Richard JAM Stevens. “Impact of wind farm wakes on flow structures in and around downstream wind farms”. In: *Flow* 2 (2022), E21.
- [17] L. Liu, S. N. Gadde, and R. J. A. M. Stevens. “Universal wind profile for conventionally neutral atmospheric boundary layers”. In: *Phys. Rev. Lett.* 126 (2021), p. 104502.
- [18] L. Liu and R. J. A. M. Stevens. “Vertical structure of conventionally neutral atmospheric boundary layers”. In: *Proc. Natl. Acad. Sci. U.S.A.* 119.22 (2022), e2119369119.
- [19] S. E. Haupt et al. “Lessons learned in coupling atmospheric models across scales for onshore and offshore wind energy”. In: *Wind Energy Science* 8 (2023), pp. 1251–1275.
- [20] T. Burton et al. *Wind Energy Handbook*. New York: John Wiley & Sons, 2001.
- [21] Geoffrey Ingram Taylor. “The spectrum of turbulence”. In: *Proceedings of the Royal Society of London. Series A-Mathematical and Physical Sciences* 164.919 (1938), pp. 476–490.
- [22] T. Nanahara et al. “Smoothing effects of distributed wind turbines. Part 1. Coherence and smoothing effects at a wind farm”. In: *Wind Energy* 7.2 (2004), pp. 61–74.
- [23] M. Naemi and M. J. Brear. “A hierarchical, physical and data-driven approach to wind farm modelling”. In: *Renew. Energy* 162 (2020), pp. 1195–1207.
- [24] J. D. Albertson. “Large Eddy Simulation of Land-Atmosphere Interaction”. PhD thesis. University of California, 1996.
- [25] A. M. Obukhov. “Turbulence in an atmosphere with inhomogeneous temperature”. In: *Trans. Inst. Teoret. Geoz. Akad. Nauk SSSR* 1 (1946), pp. 95–115.

- [26] A. S. Monin and A. M. Obukhov. “Basic laws of turbulent mixing in the surface layer of the atmosphere”. In: *Tr. Akad. Nauk SSSR Geophiz. Inst.* 24.151 (1954). url:gibbs.science/efd/handouts/monin\_\_obukhov\_1954.pdf, pp. 163–187.
- [27] F. Porté-Agel, M. Bastankhah, and S. Shamsoddin. “Wind-turbine and wind-farm flows: A review”. In: *Boundary-layer Meteorol.* 174.1 (2020), pp. 1–59.
- [28] P. Veers et al. “Grand Challenges: Wind energy research needs for a global energy transition”. In: *Wind Energ. Sci.* 7 (2022), pp. 2491–2496.
- [29] S. E. Haupt et al. “On bridging a modeling scale gap: Mesoscale to microscale coupling for wind energy”. In: *Bull. Am. Meteorol. Soc.* 100.12 (2019), pp. 2533–2550.
- [30] B. Kosović et al. “Impact of atmospheric turbulence on performance and loads of wind turbines: Knowledge gaps and research challenges”. In: *Wind Energy Science Discussions* 2025 (2025), pp. 1–67.
- [31] A. H. Syed and J. Mann. “Simulating low-frequency wind fluctuations”. In: *Wind Energy Science* 9 (6 2024), pp. 1381–1391.
- [32] W. Munters, C. Meneveau, and J. Meyers. “Turbulent inflow precursor method with time-varying direction for large-eddy simulations and applications to wind farms”. In: *Boundary-Layer Meteorol.* 159.2 (2016), pp. 305–328.
- [33] A. Stieren, S. N. Gadde, and R. J. A. M. Stevens. “Modeling dynamic wind direction changes in large eddy simulations of wind farms”. In: *Renewable Energy* 170 (2021), pp. 1342–1352.
- [34] B. Foloppe et al. “Development of a dynamic wake model accounting for wake advection delays and mesoscale wind transients”. In: *J Phys. Conf. Ser.* 2265.2 (2022), p. 022055.
- [35] J. Meyers et al. “Wind farm flow control: prospects and challenges”. In: *Wind Energ. Sci.* 7.6 (2022), pp. 2271–2306.
- [36] W. C. Skamarock et al. “A Description of the Advanced Research WRF Version 3”. In: *NCAR Technical Note* NCAR/TN-475+STR (2008), pp. 1–126.
- [37] D Allaerts et al. “Development of a Time–Height Profile Assimilation Technique for Large-Eddy Simulation”. In: *Boundary-Layer Meteorol.* 176.3 (2020), pp. 329–348.

- [38] R. S. Arthur et al. “Multi-scale simulation of wind farm performance during a frontal passage”. In: *Atmosphere* 11.3 (2020), p. 245.
- [39] T. Chatterjee et al. “Large eddy simulation with realistic geophysical inflow of Alpha Ventus wind farm: a comparison with LIDAR field experiments”. In: *J. Phys. Conf. Ser.* 1037.7 (2018). doi:10.1088/1742-6596/1037/7/072056, p. 072056.
- [40] R. J. A. M. Stevens, J. Graham, and C. Meneveau. “A concurrent precursor inflow method for large eddy simulations and applications to finite length wind farms”. In: *Renewable Energy* 68 (2014), pp. 46–50.
- [41] D. Muñoz-Esparza and B. Kosović. “Generation of inflow turbulence in large-eddy simulations of nonneutral atmospheric boundary layers with the cell perturbation method”. In: *Mon. Weather Rev.* 146.6 (2018). doi:10.1175/MWR-D-18-0077.1, pp. 1889–1909.
- [42] F. K. Chow et al. “Crossing multiple gray zones in the transition from mesoscale to microscale simulation over complex terrain”. In: *Atmosphere* 10.5 (2019), p. 274.
- [43] S. E. Haupt et al. “Mesoscale to Microscale Coupling for Wind Energy Applications: Addressing the Challenges”. In: *J. Phys. Conf. Ser.* 1452 (2020), p. 012076.
- [44] S.J. Andersen, N.N. Sørensen, and M. Kelly. “LES Modelling of Highly Transient Wind Speed Ramps in Wind Farms”. In: *J. Phys. Conf. Ser.* 1934.1 (2021), p. 012015.
- [45] R. J. A. M. Stevens, L. A. Martínez-Tossas, and C. Meneveau. “Comparison of wind farm large eddy simulations using actuator disk and actuator line models with wind tunnel experiments”. In: *Renewable Energy* 116 (A 2018), pp. 470–478.
- [46] S. N. Gadde, A. Stieren, and R. J. A. M. Stevens. “Large-eddy simulations of stratified atmospheric boundary layers: Comparison of different subgrid models”. In: *Boundary-Layer Meteorol.* 178 (2021), pp. 363–382.
- [47] H.H. Fernholz and D. Warnack. “The effects of a favourable pressure gradient and of the Reynolds number on an incompressible axisymmetric turbulent boundary layer. Part 1. The turbulent boundary layer”. In: *J. Fluid Mech.* 359 (1998), pp. 329–356.
- [48] S. He and J.D. Jackson. “A study of turbulence under conditions of transient flow in a pipe”. In: *J. Fluid Mech.* 408 (2000), pp. 1–38.

- [49] D. Greenblatt and E. A. Moss. “Rapid temporal acceleration of a turbulent pipe flow”. In: *J. Fluid Mech.* 514 (2004), pp. 65–75.
- [50] NWTC Information Portal. *NWTC 135-m Meteorological Towers Data Repository*. <https://nwtc.nrel.gov/135mData> (last access: 22 July 2025). 2016.
- [51] C. Bak et al. “The DTU 10-MW reference wind turbine”. In: *Danish wind power research 2013*. 2013.
- [52] S.E. Haupt et al. “Lessons learned in coupling atmospheric models across scales for onshore and offshore wind energy”. In: *Wind Energy Sci.* 8.8 (2023), pp. 1251–1275.
- [53] L. Liu, S. N. Gadde, and R. J. A. M. Stevens. “Geostrophic drag law for conventionally neutral atmospheric boundary layers revisited”. In: *Q. J. R. Meteorol. Soc.* 147 (2021), pp. 847–857.
- [54] Y. Liu, A. Stieren, and R. J. A. M. Stevens. “Modeling low-frequency wind speed variations in large-eddy simulations of wind farms”. In: *Chapter 1* (2025).
- [55] J. Fischereit et al. “Review of Mesoscale Wind-Farm Parametrizations and Their Applications”. In: *Boundary-Layer Meteorol.* 182.2 (2022), pp. 175–224.
- [56] M. Momen and E. Bou-Zeid. “Large-eddy simulations and damped-oscillator models of the unsteady Ekman boundary layer”. In: *Journal of the Atmospheric Sciences* 73.1 (2016), pp. 25–40.
- [57] M. Momen and E. Bou-Zeid. “Analytical reduced models for the non-stationary diabatic atmospheric boundary layer”. In: *Boundary-Layer Meteorology* 164 (2017), pp. 383–399.
- [58] M. Momen and E. Bou-Zeid. “Mean and turbulence dynamics in unsteady Ekman boundary layers”. In: *Journal of Fluid Mechanics* 816 (2017), pp. 209–242.
- [59] M. Momen and E. Bou-Zeid. “Mean and turbulence dynamics in unsteady Ekman boundary layers”. In: *J. Fluid Mech.* 816 (2017), pp. 209–242. DOI: [10.1017/jfm.2017.76](https://doi.org/10.1017/jfm.2017.76).
- [60] Carl-Gustaf Rossby and Raymond B Montgomery. “The layer of frictional influence in wind and ocean currents”. In: (1935).

- [61] Alfred K Blackadar and H Tennekes. “Asymptotic similarity in neutral barotropic planetary boundary layers”. In: *Journal of Atmospheric Sciences* 25.6 (1968), pp. 1015–1020.
- [62] M. Momen and E. Bou-Zeid. “Large-Eddy Simulations and Damped-Oscillator Models of the Unsteady Ekman Boundary Layer”. In: *J. Atmos. Sci.* 73 (2016), pp. 25–40. DOI: 10.1175/jas-d-15-0038.1.
- [63] I. Marusic and G. J. Kunkel. “Streamwise turbulence intensity formulation for flat-plate boundary layers”. In: *Phys. Fluids* 15 (2003), pp. 2461–2464.
- [64] C. Meneveau and I. Marusic. “Generalized logarithmic law for high-order moments in turbulent boundary layers”. In: *J. Fluid Mech.* 719 (2013), R1.
- [65] R. J. A. M. Stevens, M. Wilczek, and C. Meneveau. “Large eddy simulation study of the logarithmic law for high-order moments in turbulent boundary layers”. In: *J. Fluid Mech.* 757 (2014), pp. 888–907.
- [66] Andrey Nikolaevich Kolmogorov. “The local structure of turbulence in incompressible viscous fluid for very large Reynolds”. In: *Numbers. In Dokl. Akad. Nauk SSSR* 30 (1941), p. 301.
- [67] J. Bossuyt et al. “Measuring power output intermittency and unsteady loading in a micro wind farm model”. In: *34<sup>th</sup> Wind Energy Symposium, AIAA SciTech AIAA 2016-1992* (2016), pp. 1–7.
- [68] J. Bossuyt et al. “Measurement of unsteady loading and power output variability in a micro wind farm model in a wind tunnel”. In: *Exp. Fluids* 58 (2016), pp. 1–17.
- [69] Robert H Kraichnan. “Kolmogorov’s hypotheses and Eulerian turbulence theory”. In: (1964).
- [70] Henk Tennekes. “Eulerian and Lagrangian time microscales in isotropic turbulence”. In: *Journal of Fluid Mechanics* 67.3 (1975), pp. 561–567.
- [71] Huiwen Liu et al. “Towards uncovering the structure of power fluctuations of wind farms”. In: *Physical Review E* 96.6 (2017), p. 063117.
- [72] N. Tobin and L. Chamorro. “Wakes behind surface-mounted obstacles: Impact of aspect ratio, incident angle, and surface roughness”. In: *Phys. Rev. Fluids* 3 (2018), p. 033801.

- [73] N. Tobin et al. “Spatiotemporal correlations in the power output of wind farms: On the impact of atmospheric stability”. In: *Energies* 12.8 (2019), p. 1486.
- [74] J. D. Albertson and M. B. Parlange. “Surface length-scales and shear stress: implications for land-atmosphere interaction over complex terrain”. In: *Water Resour. Res.* 35 (1999), pp. 2121–2132.
- [75] Jakob Mann et al. “How does turbulence change approaching a rotor?” In: *Wind Energy Science* 3.1 (2018), pp. 293–300.
- [76] Janna Kristina Seifert et al. “Correlations of power output fluctuations in an offshore wind farm using high-resolution SCADA data”. In: *Wind Energy Science* 6.4 (2021), pp. 997–1014.
- [77] Edgar Jungblut, Henrik M Bette, and Thomas Guhr. “Spatial structures of wind farms: Correlation analysis of the generated electrical power”. In: *Physica A: Statistical Mechanics and its Applications* 666 (2025), p. 130508.
- [78] R. J. A. M. Stevens and C. Meneveau. “Temporal structure of aggregate power fluctuations in large-eddy simulations of extended wind-farms”. In: *J. Renew. Sustain. Energy* 6 (2014), p. 043102.
- [79] H. Holttinen. “Hourly wind power variations in the Nordic countries”. In: *Wind Energy* 8.2 (2005), pp. 173–195.
- [80] J. K. Lundquist and L. Bariteau. “Dissipation of Turbulence in the Wake of a Wind Turbine”. In: *Boundary-Layer Meteorol.* 154.2 (2015). doi:10.1007/s10546-014-9978-3, pp. 229–241. DOI: 10.1007/s10546-014-9978-3.
- [81] F. Guo and D. Schlipf. “A spectral model of grid frequency for assessing the impact of inertia response on wind turbine dynamics”. In: *Energies* 14.9 (2021), p. 2492.
- [82] R. Stoll et al. “Large-eddy simulation of the atmospheric boundary layer”. In: *Boundary-Layer Meteorol.* 177.2 (2020). doi:10.1007/s10546-020-00556-3, pp. 541–581.
- [83] A. Alexakis et al. “Large-scale self-organization in dry turbulent atmospheres”. In: *Science* 383.6686 (2024), pp. 1005–1009.
- [84] A. Vigueras-Rodríguez et al. “Spectral coherence model for power fluctuations in a wind farm”. In: *J. Wind Eng. Ind. Aerodyn.* 102 (2012), pp. 14–21.

- [85] A. R. Mehren et al. “Correlation and coherence of mesoscale wind speeds over the sea”. In: *Q. J. R. Meteorol. Soc.* 142.701 (2016), pp. 3186–3194.
- [86] T. Nanahara et al. “Smoothing effects of distributed wind turbines. Part 2. Coherence among power output of distant wind turbines”. In: *Wind Energy* 7.2 (2004), pp. 75–85.
- [87] Jordan G Powers et al. “The weather research and forecasting model: Overview, system efforts, and future directions”. In: *Bulletin of the American Meteorological Society* 98.8 (2017), pp. 1717–1737.
- [88] Y. Liu and R. J. A. M. Stevens. “Wake-corrected random sweeping model for wind farm power coherence”. In: *Chapter 4* (2025).
- [89] H. A. Panofsky and J. A. Dutton. “Atmospheric turbulence. Models and methods for engineering applications”. In: *New York: Wiley* (1984).
- [90] X. G. Larsén, C. Vincent, and S. Larsen. “Spectral structure of mesoscale winds over the water”. In: *Q. J. R. Meteorol. Soc.* 139 (2013), pp. 685–700.
- [91] Leonardo P Chamorro et al. “Turbulence effects on a full-scale 2.5 MW horizontal-axis wind turbine under neutrally stratified conditions”. In: *Wind Energy* 18.2 (2015), pp. 339–349.
- [92] N Tobin, Hao Zhu, and LP Chamorro. “Spectral behaviour of the turbulence-driven power fluctuations of wind turbines”. In: *Journal of Turbulence* 16.9 (2015), pp. 832–846.
- [93] P. D. Lund et al. “Review of energy system flexibility measures to enable high levels of variable renewable electricity”. In: *Renew. Sustain. Energy Rev.* 45 (2015), pp. 785–807.
- [94] Y. T. Wu and F. Porté-Agel. “Simulation of Turbulent Flow Inside and Above Wind Farms: Model Validation and Layout Effects”. In: *Boundary-Layer Meteorol.* 146 (2013), pp. 181–205.

# Summary

The wind power capacity is expected to expand rapidly in the near future. The growing demand of industrial applications, especially in designing and optimizing modern wind farms, urgently requires the accurate prediction of wind farm performance under realistic weather conditions. The state-of-the-art wind farm modeling and simulations primarily assume steady wind conditions. However, the validity of this assumption degrades as modern wind farms spans tens of kilometers in space, whose performance is increasingly affected by the variation of wind conditions.

In this thesis, we shift our focus from steady-state scenarios to dynamic wind conditions. The dynamic change of local weather conditions is mainly driven by the mesoscale motions of atmosphere, which can span up from tens to hundreds of kilometers in space and last for more than 15 minutes to several hours in time. These atmospheric motions continuously modify atmospheric boundary layer flow, leading to sustained wind speed changes for wind farms. Distinguished from wind speed fluctuations driven by boundary layer turbulence which lasts for seconds to minutes, the mesoscale variations are much slower and often overlooked in wind farm simulations. Understanding the impact of low-frequency wind speed variations necessities proper representation in both simulations and modeling of wind farm flow.

In Chapter 1, we developed a method to accurately represent dynamic wind speed changes in large-eddy simulations of wind farms, which allows a detailed investigation of their effects on wind farm performance under well-controlled conditions. The wake flows of wind turbines in dynamic inflow conditions significantly differs from steady case, which impacts the power output of downstream turbines inside the wind farm. Whereas Chapter 1 considers an idealized turbulent boundary layer, we extended the method to realistic atmospheric boundary layers in Chapter 2. In realistic scenarios, the atmospheric boundary layer is affected by both Coriolis effect and a capping layer above it, where the stable stratification limits the growth of boundary layer. Above the capping layer, the Coriolis force in free atmosphere is balanced by large-scale pressure gradient, resulting the geostrophic wind. The response of boundary layer flow under dynamic geostrophic wind speed exhibits complex physics due to the interaction of large-scale pressure gradient, Coriolis force and boundary layer turbulence. We demonstrated that the atmospheric boundary layer dynamics under time-varying geostrophic wind speed can be

captured by a reduced-order approach, where the turbulence is modeled from a steady-state solution. It helps advance the understanding of dynamic inflow conditions for wind farm operations.

The focus of the thesis is shifted to the power correlation in wind farms for following chapters. In Chapter 3, we investigated the coherence of turbine power output inside a wind farm using large-eddy simulations. We examined the applicability of random sweeping models for predicting the coherence between consecutive wind turbines, and investigated the impact of turbine operation which is not considered in the original model. Specifically, the above-rated turbines introduce dynamic wake flows, whose alters the coherence pattern that is not captured the random sweeping models. The effect of turbine wakes on the power coherence was investigated in detail in Chapter 4, where a wake-corrected random sweeping model was developed to incorporate the impact of turbine operations through induction factor. Large-eddy simulation results confirmed the model's validity for a wide range of wind farm scenarios.

Whereas Chapter 3 and 4 take steady inflow conditions, the effect of dynamic wind conditions is incorporated in the coherence models introduced in Chapter 5. The new dynamic sweeping model combines the mesoscale variation, boundary layer turbulence and wake-induced coherence losses in one formulation. Compared with simulation results and field observations, this model is shown to be able to reproduce spectral identity of wind farm power fluctuations, which provides significant physical insights in the spectral behavior of aggregate power output of wind farms.

The Conclusions and Outlook summarizes the main results of all the chapters, and points out future perspectives and potentials that are beyond the scope of this thesis. With a deeper understanding of wind farm flow physics under dynamic wind and wake effects, this thesis provides insights in the simulations and modeling of wind farms towards more realistic scenarios. This will benefit the design, optimization and operation of modern wind farms.

# Samenvatting

De windenergiecapaciteit zal naar verwachting in de nabije toekomst snel toenemen. De groeiende vraag vanuit industriële toepassingen naar het ontwerpen en optimaliseren van moderne windparken vereist dringend een nauwkeurige voorspelling van de prestaties van windparken onder realistische weersomstandigheden. De huidige geavanceerde modellen en simulaties van windparken gaan doorgaans uit van stationaire windcondities. De geldigheid van deze aanname neemt echter af naarmate moderne windparken zich over tientallen kilometers uitstrekken, waardoor hun prestaties in toenemende mate worden beïnvloed door variaties in de windcondities.

In dit proefschrift verleggen wij de focus van stationaire windcondities naar dynamische scenario's. De dynamische verandering van lokale weersomstandigheden wordt voornamelijk aangedreven door mesoschaalbewegingen in de atmosfeer, die zich over tientallen tot honderden kilometers kunnen uitstrekken en variëren over tijdschalen van meer dan vijftien minuten tot meerdere uren. Deze atmosferische bewegingen wijzigen continu de stroming in de atmosferische grenslaag, wat leidt tot aanhoudende veranderingen in windsnelheid voor windparken. In tegenstelling tot de snelheidsfluctuaties die worden veroorzaakt door turbulentie in de grenslaag, welke slechts seconden tot minuten duren, zijn mesoschaalvariaties veel langzamer en worden zij vaak verwaarloosd in windparksimulaties. Het begrijpen van de invloed van laagfrequente variaties in windsnelheid vereist een adequate representatie in zowel simulaties als modellering van stromingen in windparken.

In Hoofdstuk 1 hebben we een methode ontwikkeld om dynamische veranderingen in windsnelheid nauwkeurig te representeren in grootschalige wervelsimulaties (large-eddy simulations) van windparken. Dit maakt een gedetailleerd onderzoek mogelijk naar de effecten van deze veranderingen op de prestaties van windparken onder goed gecontroleerde omstandigheden. De wake-stromingen van windturbines onder dynamische instroomcondities verschillen significant van die onder stationaire condities, wat invloed heeft op het vermogensverloop van stroomafwaarts gelegen turbines binnen het windpark. Terwijl Hoofdstuk 1 een geïdealiseerde turbulente grenslaag beschouwt, hebben we in Hoofdstuk 2 de methode uitgebreid naar realistische atmosferische grenslagen. In realistische omstandigheden wordt de atmosferische grenslaag beïnvloed door zowel het Corioliseffect als een afdekkende laag erboven, waarin stabiele stratificatie de groei van de grenslaag beperkt. Boven

deze afdekkende laag wordt de Corioliskracht in de vrije atmosfeer in evenwicht gehouden door de grootschalige drukgradiënt, wat resulteert in de geostrofische wind. De respons van de grenslaagstroming onder een dynamische geostrofische windsnelheid vertoont complexe fysische processen door de interactie tussen de grootschalige drukgradiënt, de Corioliskracht en de turbulentie in de grenslaag. We hebben aangetoond dat de dynamiek van de atmosferische grenslaag onder tijdsafhankelijke geostrofische windsnelheden kan worden beschreven met een gereduceerde-orde benadering, waarbij de turbulentie wordt gemodelleerd op basis van een stationaire oplossing. Dit draagt bij aan een beter begrip van dynamische instroomcondities voor de werking van windparken.

De focus van het proefschrift verschuift in de volgende hoofdstukken naar het onderzoek van vermogenscorrelaties binnen windparken. In Hoofdstuk 3 hebben we de coherentie van het turbinevermogen binnen een windpark onderzocht met behulp van grootschalige wervelsimulaties. We hebben de toepasbaarheid geëvalueerd van willekeurige sweepingmodellen (random sweeping models) voor het voorspellen van de coherentie tussen opeenvolgende windturbines, en we hebben de invloed onderzocht van de turbinewerking, die in het oorspronkelijke model niet in aanmerking werd genomen. Met name turbines die boven de nominale windsnelheid opereren, genereren dynamische wakestromingen die het coherentiepatroon veranderen op een wijze die niet door de oorspronkelijke willekeurige sweepingmodellen wordt vastgelegd. Het effect van turbinewakes op de vermogenscoherentie is verder onderzocht in Hoofdstuk 4, waarin een wake-gecorrigeerd willekeurig sweepingmodel werd ontwikkeld dat de invloed van turbinewerking via de inductiefactor incorporeert. Resultaten van grootschalige wervelsimulaties bevestigen de geldigheid van het model voor een breed scala aan windparkscenario's.

Terwijl Hoofdstuk 3 en 4 uitgaan van stationaire instroomcondities, wordt in Hoofdstuk 5 het effect van dynamische windcondities geïntegreerd in de coherentiemodellen. Het nieuwe dynamische sweepingmodel combineert mesoschaalvariaties, turbulentie in de grenslaag en door wakes geïnduceerde coherentieverliezen in één formulering. Vergelijking met simulatiereultaten en veldwaarnemingen toont aan dat dit model in staat is om het spectrale gedrag van vermogensfluctuaties in windparken realistisch te reproduceren. Dit biedt belangrijke fysische inzichten in het spectrale gedrag van het geaggregeerde vermogen van windparken.

De Conclusies en Vooruitblik vatten de belangrijkste resultaten van alle hoofdstukken samen en wijzen op toekomstige perspectieven en mogelijkheden die buiten de reikwijdte van dit proefschrift vallen. Met een dieper begrip van

de stromingsfysica van windparken onder dynamische wind- en wake-effecten levert dit proefschrift waardevolle inzichten voor de simulatie en modellering van windparken onder meer realistische omstandigheden. Dit zal bijdragen aan de verdere verbetering van het ontwerp, de optimalisatie en de operationele efficiëntie van moderne windparken.



# Acknowledgements

I would like to dedicate this section to all the people who have shared these four unforgettable years with me during my PhD journey.

First, I want to express my deepest gratitude to my supervisors. **Richard**, it has always been a great pleasure working with you. Four years ago, when I joined PoF, I was simply passionate about fluid dynamics, yet knew almost nothing about wind energy and atmospheric science. Four years later, I have not only gained disciplinary knowledge but also developed a strong scientific character, much of which I owe to you.

**Detlef**, what I appreciate most is not only your insightful discussions and valuable suggestions, but also the excellent environment for doing science that you have created. The stability, flexibility, and freedom at PoF, along with its rich resources, have made these four years truly precious. I especially enjoyed every seminar — the wide range of topics broadened my perspective on fluid dynamics as a whole. Thank you for making PoF a place where science becomes so exciting and enjoyable.

I would like to thank the members of my thesis evaluation committee — **Devaraj, Kees, Fulvio, and Joshua** — for reviewing my work and for the engaging discussion during my defense, which made that day truly memorable. Many thanks also to **Jeroen** for chairing the defense ceremony.

**Joanita**, there's no need to explain the magic you have in keeping everything organized so perfectly — everyone at PoF already knows it. I simply want to thank you for every single moment you've offered your help and support.

## *Wind Farmers*

**Jens** and **Davide**, we spent most of our time together over the past four years - from Glasgow to Lyon, Florence, and Nantes, sharing the best pizzas along the way. **Davide**, thank you for introducing me to real Italian food beyond Domino's and Happy Italy! I look forward to celebrating your defense ceremony soon. **Jens**, you were the first doctoral student among us - and became the most experienced PoFer and wind farmer when we just started. Thank you for all your help and for being my paranymph. **Manideep**, we had great fun together at the sports day, but maybe next time you could join on your bike, like everyone else! **Giacomo**, I hope you've mastered English by

now — after taking more language courses than group meetings! Jokes aside, I'm sure you'll master both English and research. **Dong**, I truly enjoyed our project discussions, and of course, the hotspot. Enjoy your time on campus with your girlfriend! **Thomas**, you're always so kind and easy to talk with. As a local, you've shown that finding housing in Enschede can be challenging even for Dutch people. I hope you enjoy your new place. **Joppe**, welcome to the group - I look forward to getting to know you better in the days ahead.

**Anja**, I continued your project when I began my PhD, and I'm deeply grateful for your insights and advice, even after you finished your work here. **Srinidhi**, you were the first wind farmer I met during my interview - thank you for your kindness at that early stage, which encouraged me to start and complete this journey. **Jessica**, it's always nice to meet you again even after your graduation - I hope for many more visits to KNMI in the future. **Luo-qin**, I've learned so much from your insightful papers and from our discussions and collaborations. Thank you for all the knowledge you've shared. **Lucas**, although our time working together was short, it was full of great memories. All the best in your new position - I look forward to meeting again somewhere in Europe. **Jules**, **Ariane**, **Didier**, I really enjoyed the visits in both Lyon and Enschede. Thanks for your hospitality and the amazing French Cuisines.

### *My Chinese Colleagues*

**Rui**, you were the first PoFer I met upon arriving in Twente, which opened the door to countless moments of work, fun, and laughter together. I hope we both reach our goals and “see each other at the summit!” **Dehao**, even though you might disagree, I still believe I spent more time in the office than you did! I’ll never forget filming for Rui’s video while the rest of the group was away at APS. We still made it work. **Rundong**, thank you for being my paranymph. Sorry for always chatting with you in the office. I hope you’ll miss it when it’s gone. **Haoran**, we spent so much time together playing cards, basketball, and sharing meals. Let’s keep those memories alive whenever we meet again. **Yibo**, thank you for your amazing cooking and dry humor. I really enjoyed our time as roommates. **Yixin**, I still miss our trip to America, with the drives, the food, and the landscapes we explored together. You were the best travel partner; I wish you all the best for your future. **Linfeng**, thank you to you and your family for your warm hospitality. You always made me feel at home. **Boxue**, your pool skills are on another level, but I’m glad we could still have fun playing with Dehao!

*Friends in PoF*

To my wonderful office mates in ME214a: **Prashanth, Minkush, Ellis, and Pim W.** - although we worked on very different topics, our conversations were always interesting and full of ideas. Thank you for being so patient with my naive questions when I was curious about your work. We complained about the Dutch weather together, but also shared many drinks and cakes that made everything better. **Jens and Rundong**, thank you again for being my paranympths and for all your efforts - our small office truly became a cozy little community within PoF thanks to all of you.

I would like to express my gratitude to others in PoF. **Chris, Vanshu, Naoki**, I enjoyed our small talks and the moments of making movies. **Marco**, we entered the group about the same time, and with being the audience of your talks, I also learned a lot on porous media and Darcy's law. Also to **Ehsan, Mohammed, Tolga**, and many others, I enjoyed the time we spent together, and I wish all the best in your academic career.

*Family*

Last but not least, I want to express my heartfelt gratitude to my family. **Shiyu**, I feel incredibly lucky to have met my best companion during the best years of my life. You've stood by me through all the ups and downs, all sleepless nights, turning these four years into a shared memory for both of us. To my **parents and sister**, you are my constant source of strength and inspiration. Pursuing a PhD has been far more challenging than I ever imagined, and I could not have done it without your unwavering support.



# About the author



Yang Liu was born on August 22<sup>nd</sup>, 1995, in Ju Xian, China. Growing up in the countryside, his childhood was filled with the sights and sounds of chickens, goats, and donkeys. Although he enjoyed rural life, he developed a strong fascination with aviation from an early age.

When he began primary school, Yang and his family moved to Qufu - the hometown of Confucius. Before entering university, he spent most of his teenage years living in Shanghai for five years and in Beijing for four years, with experiences that broadened his worldview and deepened his curiosity about natural science.

After successfully passing the national college entrance examination, Yang pursued a bachelor's degree in Engineering Mechanics at the Harbin Institute of Technology, China. As one of the top 5% of students in his major, he was selected to study in the Elite Program. Motivated by a desire to expand his horizons, he continued his studies in Germany at the Technical University of Dresden, where he earned the Diplomingenieur degree in Aerospace Engineering in 2021. During his time in Dresden, he met Shiyu, whom he married in 2025.

Driven by his passion for fluid dynamics, Yang decided to continue his academic journey. Since 2022, he has been a PhD student in the Physics of Fluids group at the University of Twente, working under the supervision of Richard Stevens and Detlef Lohse. His research focuses on wind energy, using numerical simulations and physical modeling to study the impact of dynamic wind conditions on wind farm performance.

Outside of his academic life, Yang enjoys a wide range of hobbies. He is an enthusiastic fan of anthropology and linguistics, with a special interest in ancient Chinese languages. He also loves playing the piano, and actively participates in badminton, basketball, skiing, and swimming.